Nanoscale

REVIEW

View Article Online
View Journal | View Issue

Cite this: *Nanoscale*, 2023, **15**, 907

Tiny spots to light the future: advances in synthesis, properties, and application of perovskite nanocrystals in solar cells

Lucas Scalon, [a] Flavio Santos Freitas,[b] Francisco das Chagas Marques*[c] and Ana Flávia Nogueira *[a]

Perovskites are in the hotspot of material science and technology. Outstanding properties have been discovered, fundamental mechanisms of defect formation and degradation elucidated, and applications in a wide variety of optoelectronic devices demonstrated. Advances through adjusting the bulk-perovskite composition, as well as the integration of layered and nanostructured perovskites in the devices, allowed improvement in performance and stability. Recently, efforts have been devoted to investigating the effects of quantum confinement in perovskite nanocrystals (PNCs) aiming to fabricate optoelectronic devices based solely on these nanoparticles. In general, the applications are focused on light-emitting diodes, especially because of the high color purity and high fluorescence quantum yield obtained in PNCs. Likewise, they present important characteristics featured for photovoltaic applications, highlighting the possibility of stabilizing photoactive phases that are unstable in their bulk analog, the fine control of the bandgap through size change, low defect density, and compatibility with large-scale deposition techniques. Despite the progress made in the last years towards the improvement in the performance and stability of PNCs-based solar cells, their efficiency is still much lower than that obtained with bulk perovskite, and discussions about upscaling of this technology are scarce. In light of this, we address in this review recent routes towards efficiency improvement and the up-scaling of PNC solar cells, emphasizing synthesis management and strategies for solar cell fabrication.

Received 13th September 2022,
Accepted 18th December 2022

DOI: 10.1039/d2nr05043a

rsc.li/nanoscale

[a]*Institute of Chemistry, University of Campinas, Campinas, São Paulo 13083-970, Brazil. E-mail: anafla@unicamp.br*
[b]*Centro Federal de Educação Tecnológica de Minas Gerais, Minas Gerais 30421-169, Brazil*
[c]*Instituto de Física Gleb Wataghin, University of Campinas, São Paulo 13083-970, Brazil*

1. Introduction

Since the first communication on the perovskites applied in solar cells[1] the scientific community has initiated a true revolution in several fields. From the search for new perovskite-based materials[2–7] to attempts to understand the formation,

Lucas Scalon

Lucas Scalon graduated in Chemistry from the Federal Technical University of Parana in 2018. Since 2019, he is a Ph.D. student in Chemistry at the University of Campinas, with an exchange internship at the Integrated Center for Applied Physics and Photonic Materials (IAPP) at the Technische Universität Dresden. His current research is focused on chiral perovskites and interface engineering of perovskite solar cells.

Flavio Santos Freitas

Flavio Santos Freitas received his Bachelor degree in Chemistry from the Federal University of Uberlandia (2007), Master (2009) and PhD (2013) degrees in Chemistry from the University of Campinas. Since 2019, he is a Professor at CEFET-MG, Brazil. His current research is focused on metal chalcogenides for solar energy conversion.

self-assembly, and crystallization,[8–10] the mechanisms of charge generation and charge transfer[10,11] perovskites already have their place in the development of optoelectronics. When we take a look at the advance in solar cells, many scientific works have presented numerous ways and possibilities to bring the benefits of perovskites into products for the industrial community through studies with different architectures,[1,12–14] small to large area devices,[13,15–22] and stability tests.[17,23,24] Predictably, perovskite nanocrystals (PNCs) have not been slow to enter this race. Their high quantum confinement regime, achieved by decreasing the dimensionality of perovskite from 3D (bulk) to 0D (quantum dots), has been shown to be excellent for application in light-emitting diodes (LED) and, more recently, in photovoltaic devices. When comparing PNC-based *vs.* bulk-perovskite-based solar cells, the first displays significant benefits for the photovoltaic technology establishment, as it demonstrates improved stability of the photo-active phase, greater bandgap control, and high photovoltages for solar cells. In addition, modern deposition technologies are compatible with PNCs, since solution-based methods are the most suitable for industrialization using roll-to-roll technology.[15,18,21,25]

Despite the benefits, the integration of PNCs in solar cells is recent. The first report dates from 2016,[26] and the efficiency of these devices still lack far behind the conventional perovskite bulk-based solar cells. As a matter of comparison, the record efficiency for bulk-based devices is 25.7%,[27] whereas for PNC-based ones is ~16%.[28] The progress in this area toward improved efficiency and further upscaling requires advances in terms of synthesis protocols, comprehension of surface chemistry, the understanding of the fundamental mechanisms of nanocrystal growth and degradation, as well as device manufacture. When we consider upscaling strategies, several studies and reviews have addressed bulk perovskite-based devices[13,15–17,19,20,22,29,30] and PNCs in LED applications[31–34] or perspectives regarding their use in solar cells,[18,25] leaving a gap in scientific reports about these materials applied in large-area solar cells. Here, we contribute to this discussion by emphasizing the application of PNCs in solar cells and approaches to integrating them into large-area modules. To reach this goal, we start to discuss the main properties of PNCs, the state-of-art of synthetic routes, and strategies to fabricate efficient and stable photovoltaic devices. This background information provides a basis to draw a path toward the upscaling of PNC-based solar cells.

2. Metal halide perovskite nanocrystals

2.1 Fundamental properties of the nanocrystals

Metal halide perovskites (MHP) have the general chemical formula ABX_3, in which A is a monovalent organic or inorganic cation (*e.g.* methylammonium (MA^+), formamidinium (FA^+), cesium (Cs^+)), B is a divalent metal (Pb^{2+} or Sn^{2+}) and X is a halide anion (Cl^-, Br^-, and/or I^-). Three-dimensionally and ideally, it organizes as a cubic structure comprised of a share-corning lead (or tin) octahedron ($[Pb(Sn)I_6]^{4-}$) with the A-site cation in the cubo-octahedral void formed by eight octahedrons (see Fig. 1a). By varying the A, B, and X species, it is possible to obtain a plethora of different perovskite compositions, allowing fine control of the MHP structural, optoelectronic and photophysical properties.[2,35–40]

Another method to control the MHP's properties is changing its dimensionality rather than composition. Going from bulk 3D to 0D quantum dots (QD) the energy band structure changes from continuous to discrete (*i.e.*, quantized) (Fig. 1b),[41–43] in which the electron can only occupy specific

Francisco das Chagas Marques

Francisco das Chagas Marques is Full professor at the Gleb Wataghin Physics Institute, University of Campinas (UNICAMP), from where he received his Ph.D. degree in physics in 1989. He was a post-doctoral fellow at Harvard University, visiting professor at the University of Utah, and visiting researcher at SCIRO, Melbourne. He has published over one hundred research papers working in the development and study of optoelectronic, structural, and thermomechanical properties of amorphous, microcrystalline, and nanostructured materials and in the manufacture of photovoltaic devices.

Ana Flávia Nogueira

Bachelor's degree in Chemistry from the University of São Paulo (1996), Master (1998), and PhD degrees in Chemistry from the University of Campinas (2001). She worked as a postdoctorate fellow at the Imperial College, UK, in 2001–2002 and as visiting researcher at Stanford University from 2017–2018. At the moment, Ana Flavia is Full Professor at the Institute of Chemistry at UNICAMP and Director of the Center for Innovation on New Energies (CINE). Prof. Nogueira's research focuses on the development of functional (nano)materials and their application in solar energy conversion. She has experience in the field of perovskite solar cells, perovskite quantum materials, and dense energy carriers.

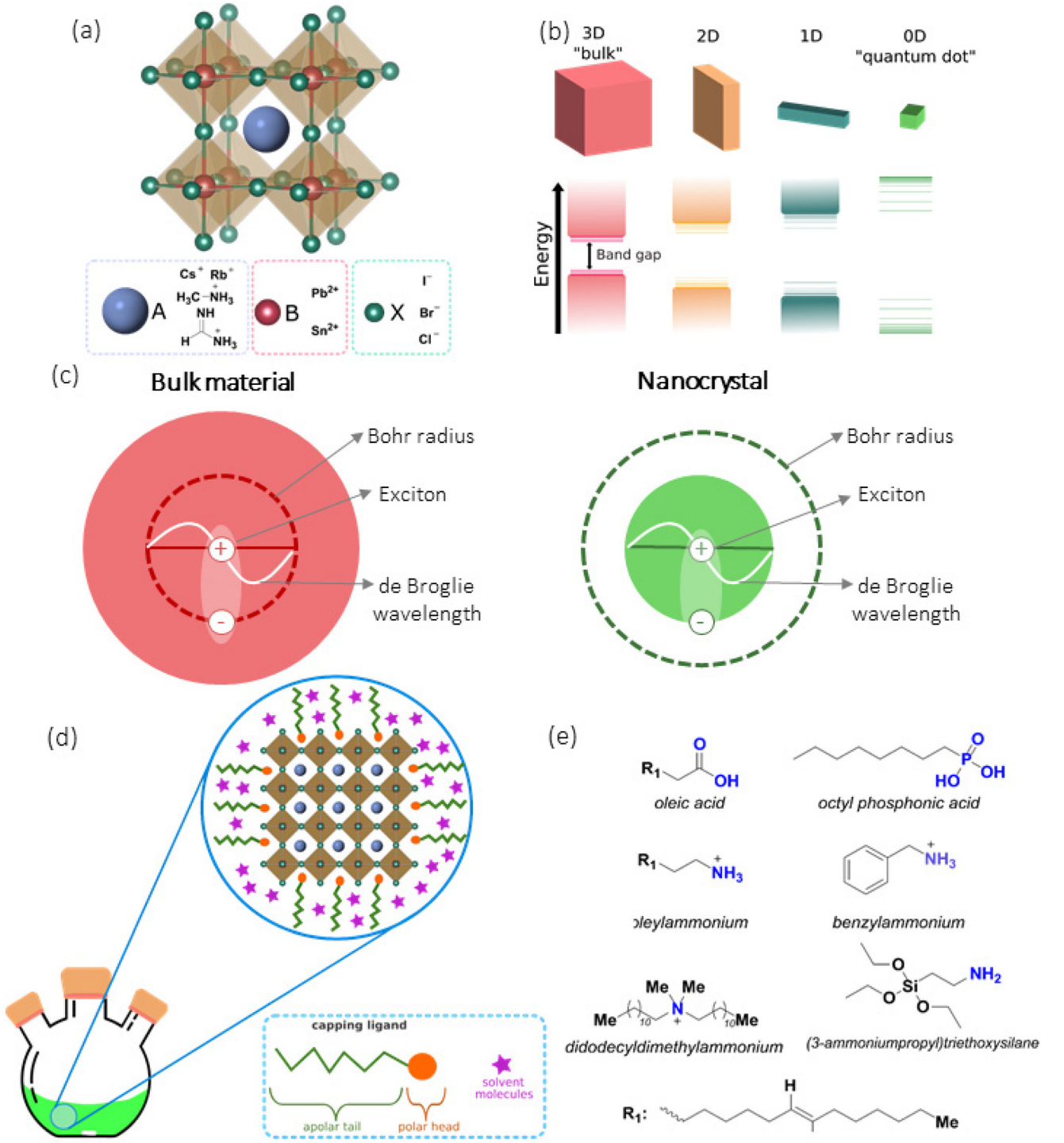

Fig. 1 (a) Crystal structure of an ABX_3 perovskite. (b) Dependence of the bandgap on the size of the material. The quantum confinement increases the bandgap going from bulk 3D to the quantum dot 0D. (c) Schematic illustration of the de Broglie wavelength confinement with the decrease in the material's size. (d) Schematic illustration of the micelles formed by the capping ligands: the polar head of the molecule interacts with the perovskite QD while the apolar tail interacts with the solvent. (e) Chemical structures commonly used capping ligands.

energies in the system. The effect of the quantization can be visualized in the electronic absorption spectra of the QDs as sharp and well-defined peaks,[44,45] a feature that becomes less prominent as the size increases and the material assumes a bulk-like behavior. Another particularity is the dependence of the bandgap (E_g) on the NC size. This happens because as the material's size becomes smaller than the Bohr radius (the average separation length between electron–hole pairs generated by photoexcitation), the de Broglie wavelength of a free electron (or hole) becomes highly confined inside the particle

(Fig. 1c),[46] making the E_g of the QD dependent on the size: decreasing the size, increases the E_g.[47] The explanation for this phenomenon lies in the solution of the Schrödinger equation for a particle confined in a three-dimensional system (case of a 0D QD), which tell us that the energy of the levels is inversely proportional to the square of the wall thickness, *i.e.*, the nanoparticle size. In other words, narrow walls have more wide-spaced levels, resulting in higher E_g.[48,49] In this sense, the variation of the NC size can be used to control the confinement regime, which ultimately affects the material's bandgap. Let us take the $CsPbBr_3$ NC as an example. Its exciton Bohr radius is about 7 nm.[50] As size decreases to <7 nm, the electron energy levels assume a discrete rather than continuous energy landscape (see Fig. 1b), causing the material to fall into the *quantum confinement regime*.[51] Based on the size, we can classify these materials in two different regimes: a high confinement regime when the NC dimensions are $\ll$7 nm, and a low confinement regime when the NC dimensions are $\gg$7 nm,[48,52] which will affect the optoelectronic properties of the material.

Because of its small size, the surface/volume ratio of NC is large. Considering a spheric NC, its surface area can be expressed as $4\pi r^2$, and its volume $4/3\pi r^3$; here r is the radius of the sphere. Therefore, the surface/volume ratio is $3/r$. In this sense, a 7 nm diameter particle will have a surface area equal to 154 nm^2, and the surface/volume ratio is $\sim 8 \times 10^8$ m^2/m^3. For this reason, there are much more atoms on the surface than in the interior of the NC, which is opposite to bulk materials, in which the surface is only a tiny fraction of the whole.[53] As a consequence, the chemical potential (*i.e.*, reactivity) of the surface is very high. To decrease the surface's reactivity, the NC tends to agglomerate with time to form large domains, which causes loss of the quantum confinement regime (note that, in this situation, the material's size will increase). To avoid this natural tendency of agglomeration, capping ligands are required to stabilize the material by forming micelles, as schematized in Fig. 1d. Commonly, alkylamines, carboxylic acids, and phosphonic-based ligands are used (Fig. 1e).[54–58] These molecules are composed of a polar head that binds to the NC surface, and a long hydrocarbon tail that interacts with the solvents.

2.2 Size-dependent properties beyond bandgap

Besides bandgap, several other properties can be affected by size variations. For instance, the Stokes shift (energy difference between the emission maxima and the excitonic peak in the absorption spectra) was observed to be large for low-size NC; this seems to be independent of the composition, at least regarding the halide for $CsPbX_3$ NC-series, as shown in Fig. 2a.[59–62] First-principle calculation revealed the presence of a confined hole state (CHS), with a size-dependent energetic separation in respect to the valence band (VB) edge states,[63] which explains the dependence of Stokes shift with the NC size. It was verified that the absorption from CHS to the conduction band (CB) is dark (not seen in the UV-Vis absorption spectra) due to the low density of state (DOS). As a result, the absorption spectrum is dominated by only VB $\rightarrow$ CB edge state transitions. Nevertheless, non-radiative relaxation can occur from CB edge states to CHS, which causes CHS to be analyzed through emission spectra rather than absorption. The net result is that the photoexcited electrons lose the absorbed energy and populate a state with higher energy (*i.e.* CHS) compared to the state from where they were excited (that is, VB edge states). In this way, the emission spectra will be red-shifted, which in turn increases the Stokes shift. The possibility to obtain materials with a large Stokes shift is particularly interesting for solar cell applications, due to avoiding reabsorption losses,[64] and also has application in luminescent solar concentrators,[65] which is attractive to improve solar cell performance.

Additionally, the size was revealed to impact the lattice strain and crystal phase of the PNC.[66] For instance, as the $CsPbI_3$ size increases from 5.7 to 15.3 nm, it loses the α-phase cubic symmetry, approaching γ-phase symmetry with an orthorhombic structure for larger NC, as can be seen from the XRD patterns in Fig. 2b and c. The results also showed that small NC experiences higher tensile strain and revealed octahedra tilt as the size increases. Small NC also seems to be less prone to cubic-to-tetragonal phase transitions at low temperatures (120 K), whereas the large ones suffer from phase transition because of changes in electrical polarization.[67]

Furthermore, Shang *et al.* revealed a size dependence on the charge separation (CS) and charge recombination (CR) rates from $CsPbI_3$ QD to rhodamine (electron acceptor) by varying the NC size from 11.8 to 6.5 nm, as depicted in Fig. 2d.[68] In this regime of weak to moderate quantum confinement regime, the authors found that the size dependence of the rates is mainly controlled by the orbital overlap between the QD and the rhodamine.[69] As a result, the electron transfer is not dependent on the energy level matching between the donor (in this case the QD) and the acceptor (rhodamine) lowest-unoccupied molecular orbital (LUMO), as observed for QD with a strong quantum confinement regime (*i.e.*, small NC size).[69] These findings are particularly interesting for optoelectronic applications, in which charge separation and charge recombination dictate the main working mechanism of the devices. It should be highlighted that this study investigated the dynamics of charge transfer in the solution state. Translating those findings to the thin-film state should be analyzed carefully, since the solvent may play a role in the charge transfer mechanism.

2.3 Tuning PNC composition and the impact on the material's properties

In a lead halide perovskite material, the valence and conduction bands are mainly formed by Pb 6s and X *n*p (where *n* is an integer) and Pb 6p and X *n*p orbitals, respectively. Therefore, tuning the composition of the PNC results in a change in the position of both CB and VB.[70,71] In addition to the direct impact of the composition on the bandgap, other properties of the material can be influenced. For example, for mixed halide composition in $CsPbBr_xI_{3-x}$ NCs, an increase in the iodide content causes additional centers for hole trapping.[72] This

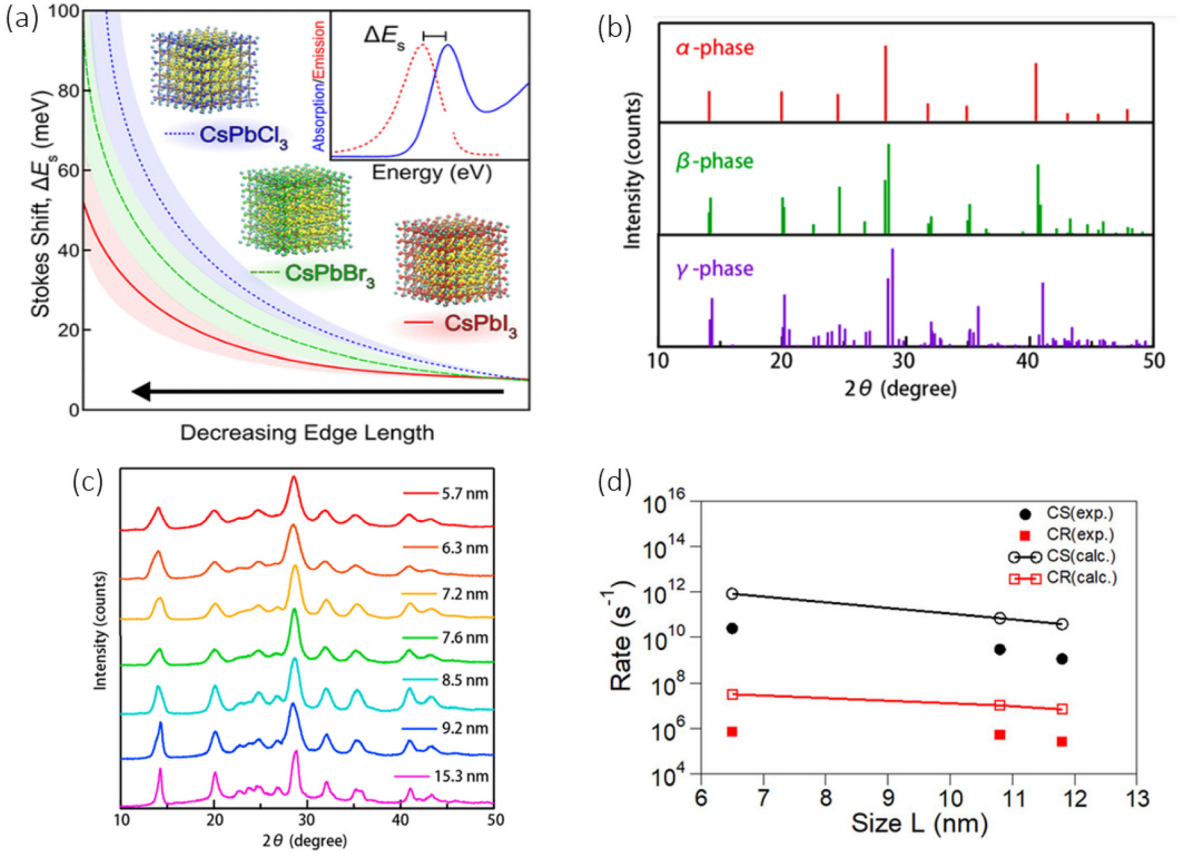

Fig. 2 (a) Dependence of the Stokes shift with the variation of NC size from three compositions of PNC: $CsPbCl_3$, $CsPbBr_3$, and $CsPbI_3$.[62] (b) Simulated XRD of α-, β-, and γ-phase of $CsPbI_3$ PNC; (c) experimental XRD of $CsPbI_3$ with different NC phases.[66] (d) Calculated (empty symbols) and experimental (filled symbols) charge separation (CS) and charge recombination (CR) rates of $CsPbI_3$ QD-rhodamine and their variation with the NC size.[68] (a) Reproduced with permission from ref. 62. Copyright 2020 American Chemical Society. (b and c) Reproduced with permission from ref. 66. Copyright 2019 American Chemical Society. (d) Reproduced with permission from ref. 68. Copyright 2019 AIP Publishing.

occurs because of the presence of Br^- and I^--rich regions,[73,74] which causes the holes created in the Br-rich NC, which has a higher bandgap, to move to the I-rich NC, which has a lower bandgap.[72] Similarly, alloying Cl/Br and Br/I leads to a bathochromic shift of the emission spectra as the bromide or iodide content increases due to the formation of large particles and because of the influence of the anion in the electronic structure of the perovskite.[2,75] This is an excellent alternative to tuning the color emitted by the material. Furthermore, we demonstrated recently that the presence of an absorption tail in low-temperature absorption spectra of $CsPbX_3$ (X: Cl, Br, I) is indicative that iodide-based NC is less defect tolerant than the bromide and chloride,[76] which suggests that iodide may be generating more shallow levels near the band edges when compared to the other two halides. Another interesting impact of the halide anion is in the coherent vibration of the wave packets generated upon photoexcitation, which was found to be dependent on the halide anion for the case of $FAPbX_3$ NC (X: Br and I).[77] This happens because the FA rotation in the Br-base NC is higher compared to the I-based, which means that there is a stronger interaction between FA and $[PbBr_6]^{4-}$.[77]

In addition to the halide anion, the A-site cation may also influence the nature and properties of the PNCs. In the $APbBr_3$ series, in which A: Cs, MA, and FA, the NC size is larger for the ones based on the organic cations.[78] Fig. 3a shows TEM images of $CsPbBr_3$, $MAPbBr_3$, and $FAPbBr_3$. The NC size goes from 9.2 nm for the inorganic-NC, to 17.3 and 12.9 nm for MA-, and FA-based NC, respectively, which directly impacts the absorption and emission features.[78] The energy separation between dark and bright states decreases from Cl to Br and I, and with the replacement of Cs by FA (Fig. 3b).[79] This is important because the thermalization of the excitons towards dark states reduces the light emission efficiency, mainly because of the spin and momentum-forbidden transition to the ground state.[80] In this sense, having a large energy separation between the bright and the dark excitonic states should, in principle, improve the radiative recombination of the NC. However, the impact of the dark exciton on the performance of optoelectronic devices based on MHP NC is still understudied.

2.4 Surface-dependent properties

It is well-known that PNCs are tolerant to typical defects found in perovskite materials as vacancies, surface states, and grain

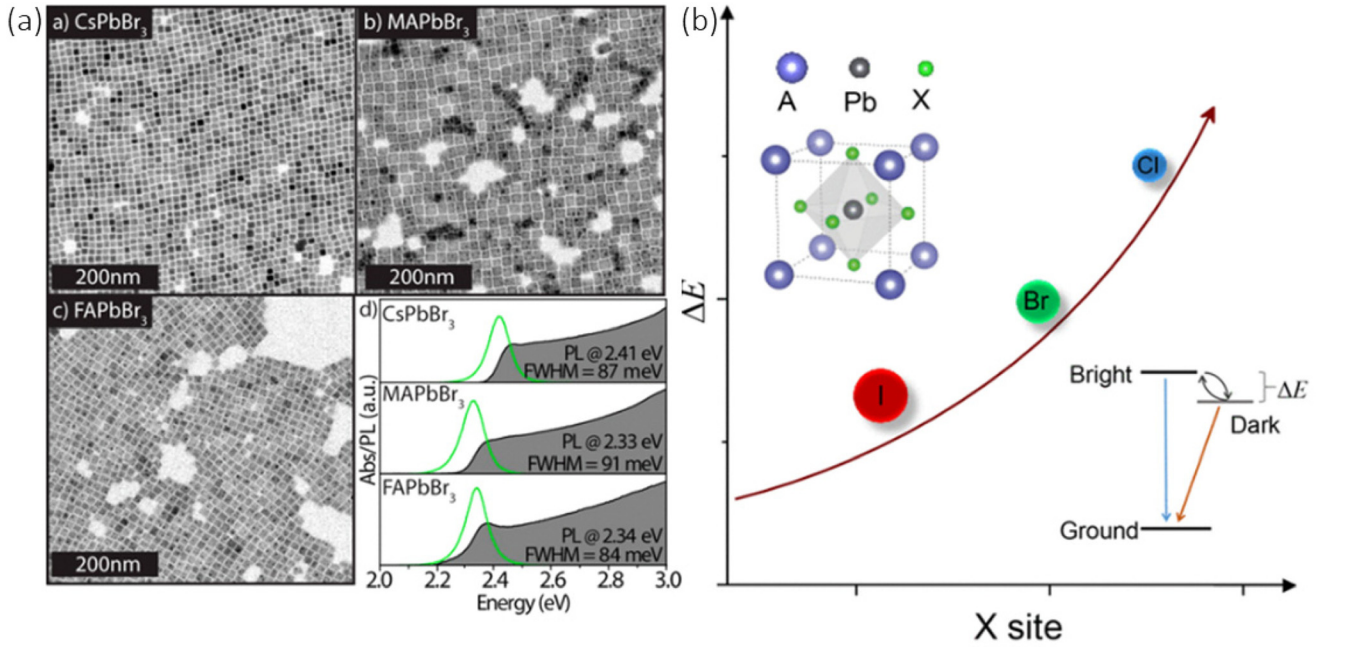

Fig. 3 (a) TEM images, and absorption and emission features of a series of $APbBr_3$ PNC (A = Cs, MA or FA).[78] (b) Schematic illustration of energy separation between the dark (spin-forbidden transition to ground state) and bright (allowed the transition to ground state) and its dependence on the X-site cation specie.[79] (a) Reproduced with permission from ref. 78. Copyright 2018 American Chemical Society. (b) Reproduced with permission from ref. 79. Copyright 2018 American Chemical Society.

boundaries.[81] In a 10 nm PNC, for instance, it is estimated one defect *per* ~10^2–10^7 cm^{-3},[82] whereas bulk perovskites have defect densities in the range of 10^{11}–10^{16} cm^{-3}.[83,84] For a nanoscale regime, these point defects are mostly at the surface of the NC because of the huge number of atoms exposed and the ionic nature that allow halide atoms to escape from the surface.[81] Also, stability may drive bulk-type defects in the core towards the surface,[82] which is explained by the structural instability and the high ionicity of PNCs.[81] This characteristic is also responsible for the occurrence of ion exchange reactions for halide anions[85] and bivalent cations.[86] The intrinsic defect tolerance of PNC is predominantly ascribed to its electronic band structure. For example, in $CsPbX_3$ NCs, the valence band maximum (VBM) consists of the antibonding interaction between the X *n*p orbitals (n = 5, 4 and 3 for X = I, Br, Cl, respectively) and the Pb 6s orbitals, while the conduction band minimum (CBM) results of antibonding interaction between X *n*p and Pb 6p orbitals.[87] This means that the VBM has antibonding features, and the CBM, has a strong spin–orbit coupling. As a consequence, the defect states of PNCs are within (or near) the VBM or CBM rather than in the bandgap, leaving it free of trap states.[81] The proximity to the band edges makes the thermal energy, k_BT, enough to the defect states become filled with charge carriers at room temperature.

Regarding the defect tolerance, ten Brinck *et al.*[82] found that the interstitials defects in $CsPbBr_3$ nanocrystals are energetically favored and the PNC tends to accommodate ionic pairs (*i.e.* CsBr or $PbBr_2$) in the lattice. The authors noticed that midgap states can arise only from halide species independently of the interstitial defect, either cationic or anionic. These localized states triggered by the halide ion only cause trap states if the anion occupies surface positions that point outward the surface. The excess of halide species against the available halide surface sites exemplifies this situation, where its non-bonding lone electron pairs produce trap states. Since surface passivation can form halide-hydrogen bonds on the surface, this treatment, beyond avoiding agglomeration, could inhibit the capture of the excited electrons by the surface traps.[87,88] Vacancy defects by removing ions from either the surface or the core have negligible densities since the energy required to create vacancies is in the range of 1.4 to 2.3 eV. It means that ionic extraction must be induced from species around PNC, which is more effective at the surface, and denotes how surface chemistry plays an important role in the NCs' stability.[82]

As will be addressed in the next sections, surface ligands are molecules that bind to the surface and drive the synthesis through tunable sizes, dimensionalities, morphologies, and the related aspects of PNC including stability and optoelectronic properties. Stability is improved when surface passivation is carefully selected, although an effective surface shelling may inhibit the charge transport and deteriorate the device's performance.[78,88–90] Furthermore, surface ligands are labile and the detachment of these species can be promoted by organic solvents used in the synthesis or purification due to moderate solubility, and also through neutralization, *e.g.*, oleylammonium bromide being converted into oleylamine and HBr. The detachment mechanisms lead to the elimination of ion pairs from the PNC surface, leaving vacancies and expos-

ing undercoordinated halide ions, which are responsible to trap states and the reduced optical response.[90]

An elegant way to reduce surface defects associated with an appropriated surface coverage is to interconnect the PNCs to form crosslinks. This strategy not only enhances the PNC stability but also influences optical and solubility properties.[81] Li *et al.*,[91] for example, used butylphosphonic acid and 4-ammonium chloride in $MAPbI_3$ NCs, and demonstrated that hydrogen bonds through N–H···I and P-OH···I are intermolecular interactions sufficient to link PNCs. The solution was then spin-coated onto TiO_2 and annealed at 100 °C giving rise to a homogeneous layer and solar cells with an efficiency of 16.55%.[91] The use of ligands able to form stronger bonds, *i.e.* covalent bonds, between PNCs is another interesting approach to reaching/improving PNC-PNC connections. Liu *et al.*,[92] used nitrene radicals from the photochemistry of bisazide under UV irradiation to form covalent C–N bonds with long alkyl chains from ligands on neighboring PNCs, creating PNC networks and retaining their morphological properties. This method for direct optical patterning of perovskite NCs with ligand cross-linkers (DOPPLCER) does not require ligand exchange and is universal to PNCs with various compositions, sizes, surface chemistry and synthesized by different methods. The multicolored patterning of various PNCs *via* DOPPLCER, retained their size-defined, and emission features before and after patterning ($CsPbBr_3$ and $CsPbCl_{3-x}Br_x$, except for the unstable red-emitting $CsPbI_{3-x}Br_x$).[92] Post-patterning anion exchange with iodide salts converts $CsPbBr_3$ NCs to $CsPbI_{3-x}Br_x$ patterns and suggests that the PNC cores remain reactive and accessible probably due to the low degree of crosslinking, in contrast to cross-linked ligands *via* X-ray irradiation or with polymeric ligands.[93–95] Furthermore, the method shows the preservation of optical absorption and emission characteristics before and after cross-linking at mild conditions[92] without a high-energy source or a ligand exchange process. UV irradiation has promoted crosslinking reactions between PNCs using a polymer backbone containing a cinnamoyl group[95] or 2,2-dimethoxy-2-phenylacetophenone (DMPA).[96]

2.5 Mechanism of charge generation and dissociation in PNCs

A great attribute of PNCs is their tunable composition of cations and anions delivering a wide spectral emission range (400–700 nm with $CsPbX_3$ and $MAPbX_3$, and up to 800 nm with $FAPbI_3$ NCs), typically with a full width at half-maximum (FWHM) of 12–50 nm.[97] The A-site cation (*e.g.* FA, MA and Cs) does have a subtle effect on the bandgap due to the distortion of the cubic crystal structure, but it does not contribute expressively to the conduction and valence bands in terms of density of states.[98]

From computational calculation based on $MAPbI_3$ NCs, the VBM and CBM are characterized by the same *k*-vector, giving to PNCs a direct bandgap nature with an abrupt absorption onset at the bandgap energy, E_g. Moreover, the bands around the VBM and CBM exhibit a similar curvature. Upon photoexcitation, electron–hole pairs are generated and remain coulombically bounded forming an exciton that required activation energy on the order of the thermal energy, k_BT, to be dissociated into mobile charges.[99] The single exciton formation involves an electron in the conduction band coulombically bound to a hole in the valence band with four temporal regimes. In the first three, the electron stays within the CB in intraband processes (coherent, non-thermal, and hot excitation regime), followed by one last isothermal regime which involves an interband transition from CB to VB, the exciton recombination.

Prior to electron–hole recombination, a strong spin–orbit interaction, or L–S coupling, between the spin and the orbital motion of the carriers caused by the presence of heavy atoms like Pb in their crystal structure results in the triplet and singlet exciton states, with the last having the lowest energy. However, when L–S coupling is combined with the crystal or inversion symmetry breaking (*i.e.*, Rashba effect), it reduces the triplet state energy to below the singlet state, leading to bright triplet states with high photoluminescence quantum yield (PLQY) and fast radiative lifetimes. These low excitonic states are nearly mixed and not distinguishable at room temperature, but experimentally observed at cryogenic temperatures.[11,100,101] Therefore, the energetic order of bright and dark states is still under debate, since bright-to-dark relaxation can be induced by magnetic field, leading to the interpretation that the bright-to-dark spin relaxation is inhibited due to the faster radiative decay from the bright state than their relaxation to the dark state.[102]

PNC composition influences exciton binding energy since the atomic orbital of the species contributes to both valence and conduction bands. As the halide species changes from Cl^-, to Br^- and to I^- in PNCs, due to contribution to the VBM, the exciton binding energy decreases, while the exciton recombination, carrier trapping, and hot carrier cooling times become longer. When the A-site cation is changed from FA to MA, and Cs, an increase in the carrier cooling time due to the decrease in the strength of the carrier-phonon interaction is observed. Quantum confinement also affects exciton dynamics, on account of their small Bohr exciton diameters,[102] estimated to be 5, 7, and 12 nm for $CsPbX_3$ NCs, respectively to Cl, Br and I.[2] Thus, the photo-excited electrons and holes in PNC are physical manifestations of "particles in a box", which promotes fast and efficient radiative recombination due to spatial confinement within the NC.[103]

The time-resolved spectroscopy studies provide a comprehensive understanding of photoinduced processes, such as the excited-state lifetimes and charge carrier transfer kinetics. Especially, transient absorption spectroscopy (TAS) shows that the radiative lifetimes of $CsPbX_3$ go from 1 to 29 ns with accelerated decays from I-based toward Cl-based PNCs. For ligand-capped PNCs, a long-lived exciton lifetime is attributed to a lower density of trap states.[81]

In addition to single excitons, the generation of multiexcitons is expected to boost the photocurrent and performance of photovoltaic devices, overcoming the Shockley–Queisser efficiency limit. Bi/multiexcitons can be produced by an energy excess released by a photon with energy at least twice the

bandgap, creating additional electron–hole pairs instead of being dissipated through thermalization. However, these bi/multiexctions recombine non-radiatively through the Auger process, in which the recombination energy of one exciton is transferred to another charge carrier of the same PNC, therefore their extraction using an electron/hole acceptor prior to the Auger recombination is mandatory.[104] If a multiple exciton generation is observed for the PNC, all of the four temporal regimes previously discussed may overlap. Thus, the mechanism of multiple exciton generation is not an instantaneous process, that is, the energy excess of the hot carrier is not transferred directly to the lowest state. It starts with the excitation energies just above the energy limit of $2E_g$. Then, the additional carriers appear after those initially generated upon photon absorption in a state with longer cooling time, probed by studies with $FAPbI_3$ NCs with sizes of 7.5 and 9.8 nm, and $CsPbI_3$ with 11.5 nm, using an excitation energy of $\sim 2.25E_g$ and $\sim 2.4E_g$, respectively.[102]

When the presence of mixed halides is evaluated in PNCs with Cl doping ($CsPbI_{3-y}Cl_y$ and $FA_xCs_{1-x}PbI_{3-y}Cl_y$) the average photoluminescence (PL) lifetime was found to be ~3 times longer compared to $CsPbI_3$. The authors attributed the increased PL lifetime to the return of the photogenerated charge carriers to the band-edge state by thermal excitation after the decay to the trap states. In this work, suppression of the Auger recombination rate and consequent lengthening of biexciton lifetime was demonstrated using C_{60} as an electron acceptor, with single exciton dissociation followed by electron transfer from $CsPbI_{3-y}Cl_y$ to C_{60} revealed by a biexponential dynamics with a fast component of 18–45 ps. The multiple exciton transfer was observed for $CsPbI_{3-y}Cl_y$ and $FA_xCs_{1-x}PbI_{3-y}Cl_y$ NCs, and it was found that the biexciton lifetime is long enough (~195–205 ps) to be extracted by fullerene as well.[104] Studies with PNC in contact with redox-active molecules, *e.g.* the $CsPbBr_3$-rhodamine B, showed that the Föster mechanism (related to energy transfer over larger distances (up to 12 nm)) is dominant, in agreement with the expected and measured rate constant of energy transfer (k_{ET}). For Cl-rich nanocrystals, the measured k_{ET} is higher, indicating that the Dexter mechanism over shorter distances (1–2 nm) in these systems becomes dominant. These results demonstrate that PNCs present a unique susceptibility to chemical transformations able to access a range of energy and electron transfer process.[100] Different hetero and homojunction architectures could be employed to facilitate efficient charge extraction, *e.g.* PEDOT:PSS and/or metal oxides.[105] Terahertz kinetics of $MAPbI_3$ show that, in presence of a metal oxide with a high electron affinity like TiO_2, the charge mobility is ~7.5 $cm^2\ V^{-1}\ s^{-1}$, lower than in neat $MAPbI_3$ (~20 $cm^2\ V^{-1}\ s^{-1}$), supporting the electron injection from $MAPbI_3$ to TiO_2.[106]

3. Synthesis of perovskite nanocrystals

Bulk-perovskite thin films can be prepared through a precursor solution containing the lead and A-site cation salts in the desired solvent, and deposited by a large variety of techniques such as spin-coating,[98,107] spray,[108] inkjet printing,[109,110] blade-coating,[111,112] thermal evaporation,[113,114] rf-sputtering,[114–118] slot-die coating,[119] chemical vapor deposition,[120] and atomic layer deposition.[121] 2D layered perovskite solar cells have been mainly deposited by solution processes, and also involve the preparation of a precursor solution.[122,123] In contrast, the deposition of PNC thin films requires the previous synthesis of the nanocrystals prior to deposition using one-step wet processes. On account of that feature, we will introduce three methods used to fabricate PNC: (i) hot injection, (ii) ligand-assisted reprecipitation, and (iii) ultrasonication, underlying the strengths and weaknesses of each one.

3.1 Hot injection method

The hot injection method (Fig. 4a) is one of the most used because of the high quality of the materials obtained, with a good size and shape distribution, besides established synthesis protocol for various MHP compositions. It consists in injecting the A-site cation precursor, such as CsOAc, MAI, or FAI, into a hot solution containing the Pb source, *e.g.* $PbCl_2$, $PbBr_2$, or PbI_2, dissolved in a high-boiling point solvent, such as octadecene, in the presence of capping ligands, *e.g.* oleylamine (OLA) and oleic acid (OA) (see Fig. 1e).[2] Besides conferring colloidal stability, these ligands help to dissolve the PbX_2 precursor and passivate some defects present on the NC surface. The solution containing the lead-precursors and ligands is heated to dissolve the materials, and when it reaches the desired temperature, the A-site cation precursor solubilized in a high-boiling point solvent is added, resulting in the formation of $APbX_3$ NCs in a matter of seconds. Usually, high temperatures (>150 °C) are required to solubilize PbX_2, but the choice of the proper synthesis temperature will depend on the solubility of the precursors, the rate of growth, the nucleation of the NC, and also the thermal stability of the materials formed.[124] Synthesis temperature will also influence the final properties of the NC, as we will illustrate in the following sections.

Purification is the next step after synthesis. It is required to remove unreacted precursors and the excess ligands present on the surface, which otherwise can act as trap centers for photogenerated charge carriers.[127] Usually, the purification is performed by redispersing the NC in polar solvents (*e.g.* methanol, acetone, or ethyl acetate), known as "poor solvents", which do not have the ability to solubilize the NC. This dispersion is then centrifuged to recover the powder – the centrifugation speed can be adjusted to collect the NCs based on their size. These solvents will solubilize the unreacted precursors whereas the NC will precipitate after centrifugation. The number of washing steps should be optimized since it can lead to ligand desorption, compromising the colloidal stability, and elemental composition changes, modifying the optoelectronic properties of the NC.[128] The choice of solvent is also important since it influences the optical properties of the PNC. Fig. 4b correlates the PLQY of $CsPbBr_3$ NC dispersed in

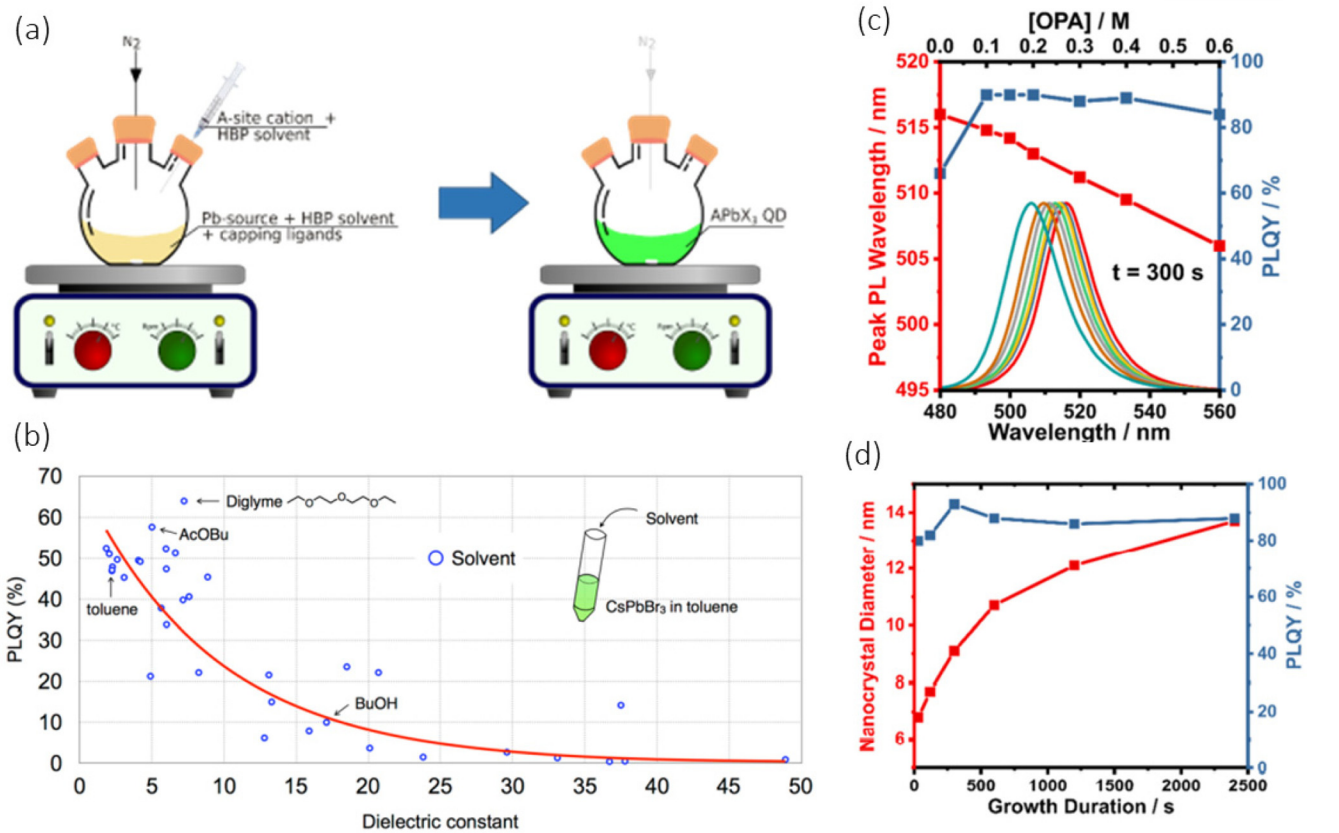

Fig. 4 (a) Schematic illustration of the hot-injection method used to produce perovskite quantum dots (QD). HPB is for high-boiling point solvents. (b) Dependence of the PLQY with the dielectric constant of different solvents used to wash the NC in the purification step.[125] (c) Variation on the emission peak and photoluminescence quantum efficiency (PLQE) with the concentration of octyl phosphonic acid (OPA) at a fixed reaction time (300 s).[126] (d) Variation of nanocrystal size and PLQE with the reaction time at a fixed concentration of OPA (0.3 M).[125,126] (a and b) Adapted with permission from ref. 125 Copyright 2018 American Chemical Society. (c and d) Adapted with permission from ref.126 Copyright 2021 American Chemical Society.

toluene after washing it with solvents of varied dielectric constant (ε).[125] As can be seen, the region with the highest PLQY values is between $5 < \varepsilon < 10$, and, among the solvents used, the best one was diglyme ($\varepsilon = 7.23$).[125] The authors found that poor solvents with low dielectric constant can allow multiple steps of NC washing without compromising the properties of the material. An interesting alternative to the centrifuge purification method was proposed by Tong *et al.*[129] They used lauryl methacrylate (LMA) as a solvent during the synthesis of $CsPbBr_3$ NC. It possesses a high boiling point, and a hydrophobic chain to stabilize the colloidal material. Adding polyurethane acrylate oligomer, and applying UV-light it can be polymerized, yielding a green-emissive composite material comprised of the $CsPbBr_3$ NC embedded into the polymeric network with PLQE as high as 85%, which keeps stable for 100 h.

One of the main challenges of the hot-injection method is the high temperature required for the synthesis, which makes the scalability difficult and very energetically expensive. Nevertheless, room-temperature alternatives to the hot injection method have been studied.[126,130,131] For example, a room temperature strategy for synthesizing $CsPbBr_3$ NC was proposed by using octyl phosphonic acid (OPA) and didodecyldimethylammonium bromide.[126] The first can control the nucleation of the NC, while the last is employed to quench the growth. By controlling the concentration of OPA and the reaction time, it was possible to tune the size of the NC, as shown in Fig. 4c and d.[126] Another alternative is reducing the solvent's boiling point through pressure reduction, which decreases the synthesis temperature by ~40 °C.[132] All of these alternatives facilitate the process's scalability and the industrial manufacture of PNC in solar cells and other optoelectronic devices.

3.2 Ligand-assisted reprecipitation method (LARP)

One of the major advantages of this method compared to the hot injection is the possibility to fabricate PNC at room temperature. It consists in dropping a solution containing the perovskite precursors (A-, B-, and X-site precursors) solubilized in a good solvent (*i.e.*, a solvent that dissolves the precursors), *e.g.* dimethylformamide (DMF) or dimethylsulfoxide (DMSO), into a solution of the capping-ligands in a poor solvent (*i.e.*, a

solvent that does not dissolve the precursors), *e.g.*, hexane, diethyl ether, chloroform, or toluene, as schematically illustrated in Fig. 5a.[133] Conversely, it is also possible to inject the solution of the amines in the poor solvent into the precursor solution. Note that the main difference here compared to the hot injection method is the existence of a precursor solution for the PNC, similar to the preparation of thin films of 3D perovskites.

The heart of this technique lies in the different solubility of the perovskite precursors in the solvent mixture. Strictly speaking, the precursors are highly stable (soluble) in the polar solvents, but when in contact with a poor apolar solvent it precipitates immediately, forming the NC stabilized by the capping ligands that coordinate Pb-sites on the surface.[134] To achieve small NCs with expressive quantum confinement effect, the chain length of the capping ligands should be optimized.[133,135] Capping ligands with a very small chain, for instance, will cause NC aggregation, thereby compromising the quantum confinement-dependent properties. On the other side, long-chain molecules will preclude the NC-to-NC electronic coupling and difficult charge extraction in the system. In addition to capping ligands, several other parameters will impact the final properties of the NCs, including the synthesis temperature, ligand/precursor concentration, and choice of solvents.[134–137]

Typically, the purification is performed by multiple centrifugation steps of the solids suspended in the poor solvent, which is analogous to the described in the hot injection method. This allows the removal, at least partially, of the unreacted capping ligands, A- and B-site precursors. The choice of the solvent in this step is also crucial since it can change the emission profile and, as a consequence, the properties of the PNC.[138] The purification with toluene and chlorobenzene, for instance, results in a broad and multiple peak emission due to a large size distribution. In contrast, hexane, a low polarity solvent (polarity equals 0.06), yields a single and narrow emission peak as a result of the narrow size distribution.

One of the major issues of this technique is the use of highly coordinated polar solvents to solubilize the perovskite precursors.[130,134,140,143] The strong coordination ability between those solvents and PbX_2 precursors results in the crystallization of the perovskite phases from PbX_2-solvent complex intermediates, causing the solvent molecules to remain in the

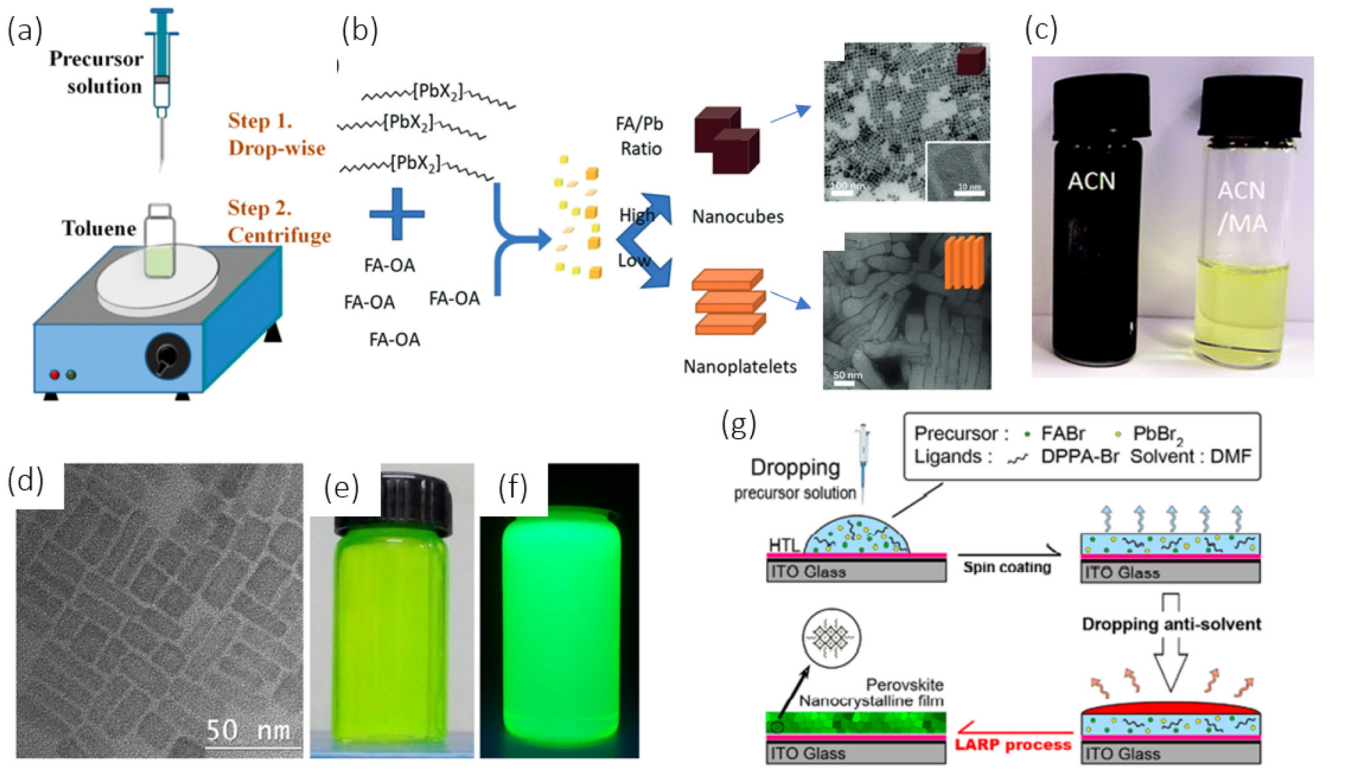

Fig. 5 (a) Scheme of the ligand-assisted reprecipitation (LARP) method: a solution containing the PNC precursors dissolved in polar solvents is dropped into a solution of the capping ligands, leading to the precipitation of the NC, which is recovered and purified by centrifugation.[133] (b) Schematic illustration of the NC size variation through the tuning of FA/Pb ratio, and the different morphologies obtained for low and high FA/Pb ratio.[139] (c) Enhancement of the solubility of $MAPbI_3$ perovskite in acetonitrile (ACN) by bubbling into methylamine (MA) gas, resulting in a clear yellow solution.[140] (d)–(f) $CsPbBr_3$ nanocubes obtained from a synthesis using $PbBr_2$ dissolved in toluene. The complete dissolution of this salt in the apolar solvent was assisted by tetraoctylammonium bromide (TOAB), yielding high fluorescent PNC.[141] (g) Illustration of the method used for the *in situ* synthesis of $FAPbBr_3$ NC directly into the desired substrate.[142] (a) Reprinted with permission from ref. 133 Copyright 2015 American Chemical Society. (c) Reprinted with permission from ref. 140 Copyright 2019 American Chemical Society. (d–f) Reprinted with permission from ref. 141. Copyright 2017 American Chemical Society. (g) Reprinted with permission from ref. 142. Copyright 2018 American Chemical Society.

final product.[144] These defective perovskites are more prone to degrade in the presence of water or oxygen. Strategies to circumvent this issue have been reported. For example, PbX_2 (X = Br, I) was dissolved in toluene with the addition of small amounts of oleic acid (OA) and oleylamine (OLA).[139] Concomitantly, the A-site source (FA-acetate) was dissolved in OA using ultrasonication. By mixing both solutions, the crystallization of the NC occurs spontaneously at room temperature, and the size can be controlled by adjusting the ratio between the A-site cation and the Pb^{2+} precursors (Fig. 5b). Acetonitrile saturated with methylamine has also been used to solubilize the $MAPbI_3$ precursors (Fig. 5c).[140] This solution was then added into a mixture of toluene, OA, and OLA, yielding cubic NC of $MAPbI_3$ with 10–15 nm size, and PLQY >90%. This was possible because methylamine can form a liquid perovskite phase with the $MAPbI_3$ perovskite with the chemical formula $CH_3NH_3PbI_3{\cdot}xCH_3NH_2$, improving the solubility of the perovskite in the acetonitrile (ACN), which is a less coordinated solvent when compared to DMF and DMSO, for instance.[145] Besides, $PbBr_2$ was found to be completely soluble in toluene in the presence of tetraoctylammonium bromide (TOAB).[141] The subsequent swift injection of this solution into a Cs_2CO_3 solution in oleic acid and toluene resulted in the formation of highly emissive $CsPbBr_3$ nanocubes with ~13 nm (Fig. 5d–f).

Using the LARP method it is also possible to fabricate *in situ* PNC films. The process is quite similar to the *ex situ* mentioned in the lasts paragraphs, the difference is that the perovskite precursor solution containing the capping ligand is coated into a substrate, and then the poor solvent is dropped, causing the supersaturation of the film due to the removal of the polar good solvent and the consequent precipitation of the NC (Fig. 5g).[142,146]

3.3 Ultrasonication method

The use of ultrasound to synthesize colloidal PNC was introduced by Tong *et al.*[147] for the synthesis of $CsPbX_3$ perovskite NC from tip sonication of $CsCO_3$ and PbX_2 in the presence of organic ligands, OA and OLA, using mineral oil or octadecene as solvents. A scheme of the synthesis is depicted in Fig. 6a. The formation of a Cs-oleate complex soluble in nonpolar solvents triggers the formation of the PNC. This synthesis approach yielded NCs with cubic and rectangular shapes, sizes in the range of 8–15 nm and varied emission colors depending on the composition (Fig. 6b). From X-ray diffraction (XRD) and transmission electron microscopy (TEM) measurements, it was

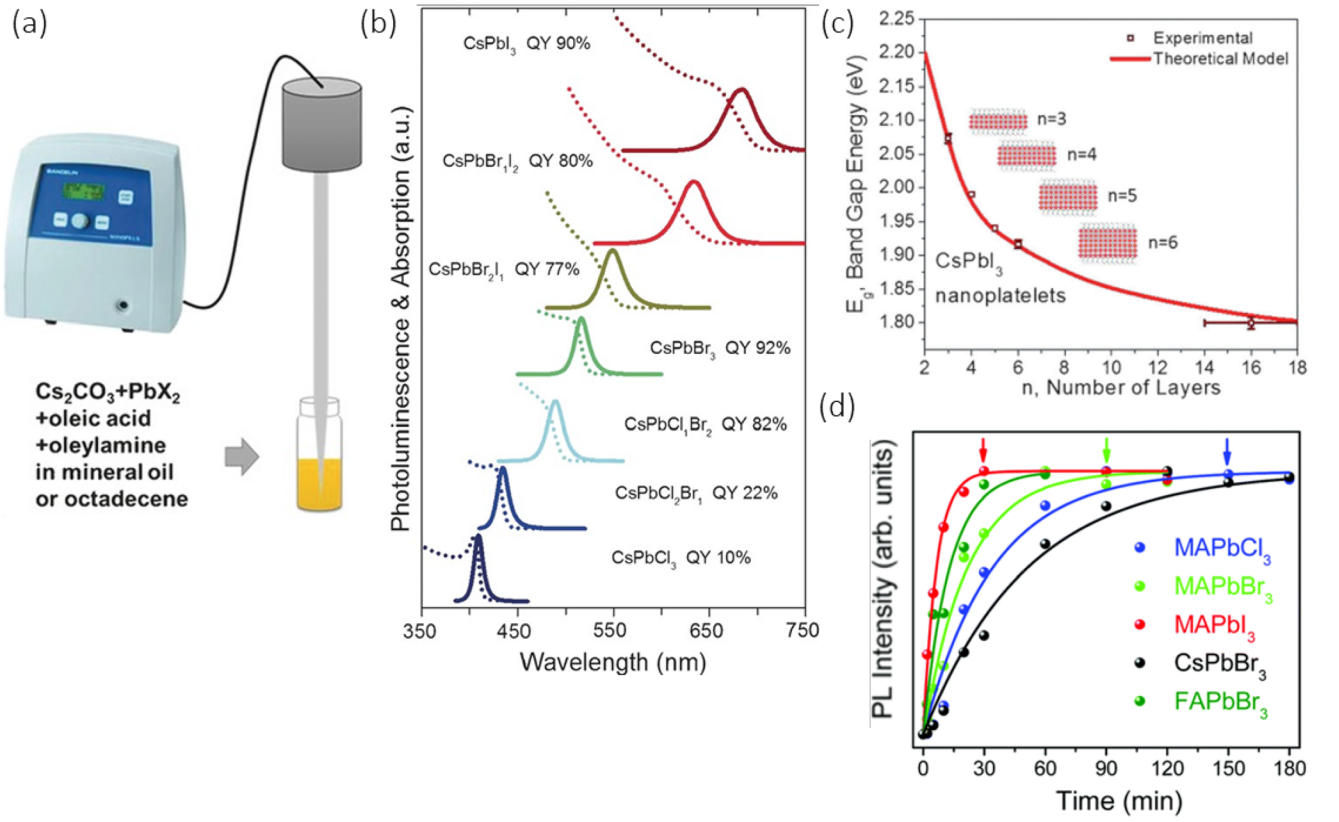

Fig. 6 (a) Schematic illustration of the PNC synthesis, and (b) absorption and emission spectra of the different compositions obtained using the ultrasonication method.[147] (c) Variation of the energy gap with the number of layers of $CsPbI_3$ NC prepared from ultrasonication, achieved by controlling the $CsCO_3/PbI_2$ ratio.[147] (d) Variation of the PL intensity from various times of ultrasonication; the time required to achieve the high PL intensity is dependent on the NC composition.[148] (a–c) Reproduced with permission from ref. 147. Copyright 2016 Wiley-VCH. (d) Reproduced with permission from ref. 148. Copyright 2016 Royal Chemical Society.

found that by lowering the Cs content the reaction rate is decreased, favoring a shapeshift from cubic to nanoplatelets (NPLs). The authors investigated the effect of the $CsCO_3/PbI_2$ ratio in the PL features of the $CsPbI_3$ NC and found an excellent way to produce NPLs with controlled thicknesses from three to six $[PbX]_4^-$ octahedra (see Fig. 6c). Almost concomitantly with the previous report, Jang *et al.*,[148] in 2016, used the ultrasonication method to produce $APbBr_{3-x}Cl_x$ PNC by sonicating AX (X = Cl, Br or I), *i.e* A-site cation precursor, with the lead source (PbX_2) and OA (1 : 1 : 3 proportion, respectively) in toluene. It was found that the sonication time depends on the solubility of the precursors in the solvent mixture (toluene + OA) and can vary from 30 to 150 min, as indicated in Fig. 6d.[148]

When compared to the hot injection method, the ultrasonication procedure uses room temperature for the synthesis. This is possible because ultrasonication promotes the formation of bubbles with a high temperature inside.[148] Those bubbles help the dissolution of the precursor's salts and cause supersaturation, nucleation, and consequent growth of the PNC. Another advantage is that it is not necessary to use an inert atmosphere during the synthesis to obtain high-quality materials.[149] In addition, it can be used to synthesize PNC without the use of polar solvents, such as octadecene and dimethylformamide (DMF). For instance, liquid paraffin was used to obtain $CsPbBr_3$ PNC with shapes varying from 3D nanocubes to 0D QD by adjusting the ratio of the capping ligands and the ultrasound power and time.[150,151] Furthermore, the PNCs can be prepared directly from the perovskite powders (*e.g.*, MAPbBr, MAPbI) and PbX_2 using OLA and OA as both capping ligands and solvents. The ultrasound breaks the bulk perovskite into NC which, in the presence of the capping ligands, stabilizes the small particles formed.[152–154] Although promising, the scaling-up of this process is challenging. The tip of the sonicator has a small size (<1 cm), which could difficult the homogeneity of the reaction, decrease the reaction yield and purity, and affect the NC properties. The scaling up of the ultrasonication method would require, for instance, multiples ultrasound tips into the reaction reservoir to allow a synthesis with appreciable yield.

4. The role of ligand chemistry, and strategies to control perovskite nanocrystals' size and shape

After introducing the main properties of the PNC and some common methods used to prepare them, we will deepen the discussion on the importance of ligand chemistry, and some opportunities that have been used to control the size and morphology of the PNC through the management of the synthesis conditions.

4.1 Surface ligands

As mentioned in the previous section, the surface ligands decrease the surface chemical potential of the NC and, consequently, improve the stability of the material due to avoiding the aggregation and loss of quantum confinement effect.[148] Furthermore, they play a key role in the passivation of defects present on the surface, which are demonstrated to cause midgap states in the energetic landscape of the PNC.[82,155,156] Because of this, it is always important to take into consideration the nature of the surface ligand, and their management has been used to control the NC properties as, for instance, the environmental, temperature, light, powder, and suspension stability, as well as the NC size and uniformity.[157,158] In addition to the aforementioned effects, the surface ligands can also impact the electronic structure of the NC.[155,156] This occurs because the interaction between the ligands and the atoms on the surface of NC changes due to the presence of the capping molecules, which means that the ligand and core experience the electric field of one another.[159]

The most common ligands used for the synthesis of PNCs are oleic acid and oleylamine. When this acid–base pair is mixed, a chemical equilibrium takes place, with the carboxylic acid protonating the amine to ammonium according to the reaction: $R\text{-}COOH + R\text{-}NH_2 \rightleftharpoons R\text{-}COO^- + R\text{-}NH_3^+$. The $-NH_3^+$ group is able to interact with the A-site of the PNCs at the surface, and stabilizes the NC by the formation of three hydrogen bonds with the X^- ions.[160] On the other hand, OA does not bind to the surface of the NC, being present as a free ligand in the solution even after the washing steps of purification.[160,161] Since the binding between the ligand and the PNC surface is very dynamic,[162] the presence of free OA helps to maintain the colloidal stability of the system. It should be highlighted that despite the role of OLA being well understood by the scientific community, the role of OA is still under constant debate, and it is not clear the mechanisms for the colloidal stability conferred by this molecule.

Several types of surface ligands have been used. We can divide them into monodentate, bidentate, branched, and zwitterions (Fig. 7). The monodentate ligands, which include both OA and OLA, are comprised of one polar head that can interact with the PNC or its precursors, and an aliphatic or aromatic moiety that interacts with the solvent. Bidentate ligands, such as 2,2′-iminodibenzoic acid and 12-aminododecanoic acid, have two polar heads, allowing them to bind at two NCs at the same time. They have been reported to reduce structural disorder at the NC surface,[163] and lead to a beneficial passivating effect.[164] In these molecules, tailoring the alkyl/aromatic chain is a good alternative to improve the optoelectronic properties of the material, benefiting charge injection and transport.[165,166] Another class of ligands are the branched ones, *e.g.* 2-hexyldecanoic acid, trioctylphosphine oxide (TOPO) and (3-aminopropyl)triethoxysilane (APTES). They are bulky molecules with a large steric hindrance, which is suggested to benefit the formation of small and more uniform NCs.[54,158,167] Finally, zwitterionic ligands such as amino acids and phosphocholine have at least two functional groups in their structure: one with a positive charge and another with a negative charge. The use of these molecules as ligands in PNCs has been reported to increase chemical stability and PLQY.[168–170]

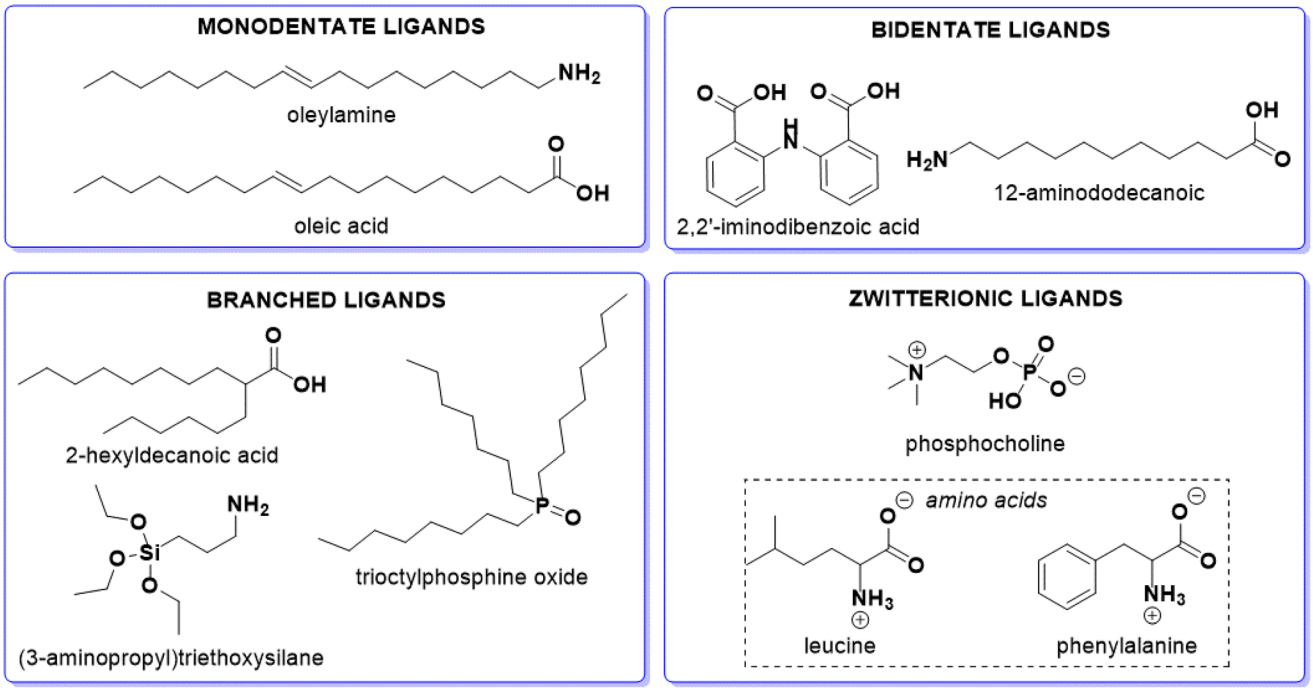

Fig. 7 Classes of ligands to be used during the synthesis of PNCs: monodentate, bidentate, branched, and zwitterionic ligands.

As can be seen, there is a plethora of molecules that can be used as surface ligands in PNCs, and it is quite hard to state universal rules for the choice of a proper ligand. In general, what is aimed is a stable and cheap ligand, capable of passivating the surface defects, and conferring colloidal stability to the NCs. In this sense, it is important to know the surface composition of the NC in order to perform modulations in the interaction strength between the ligand and the NC surface, which can be achieved by inserting electron donating or withdrawing groups to tune the electron density over the interacting polar head. This type of modification can also tune the van der Waals interactions among the ligand molecules, which can facilitate the NC-to-NC electronic coupling. The electronic coupling between the nanocrystals is an important aspect to be considered for their application in solar cells. This is because a long hydrocarbon chain can hinder proper electronic coupling and also imposes issues for charge transfer, because of its insulating nature. Therefore, short alkyl/aryl chains are preferred. However, it should be highlighted using these short-chain ligands it is more difficult to obtain small-size NC since they are less effective to prevent aggregation when compared to long alkyl/aryl chains. Therefore, the selection of the proper ligand depends on a plethora of aspects, including the synthetic methodology used, the composition of the NC surface, the density of defects, the morphology aimed, and the desired application for the material.

There is a huge floor for the exploration of new ligands, in particular, the use of functionalized molecules endowed with groups that can properly interact and passivate surface defects on the NC should be considered; we will return to this discussion later on. However, as we will discuss in **section 5**, attention should be taken to selecting the proper ligand when applying the NC to solar cells is aimed. The reason for this is that the insulating nature of the vast majority of capping ligands decreases the NC-to-NC electronic coupling, hampering the efficient charge separation in the system. At this point, it is clear that the ligand's nature is a crucial part of the integration of PNC into solar cells. Just to mention, short-chain molecules are reported to have a long exciton diffusion length compared to those with long-chain,[171] which directly impacts the charge extraction efficiency of the PNC solar cells. However, direct synthesis using short alkyl chain molecules can be challenging, especially because of the decreased solubility conferred by these molecules when compared to the long-chain ones. To circumvent this issue, post-synthetic strategies are used to replace the long-chain molecules that came from the synthesis with small ones, a process known as "ligand exchange reaction".

4.2 Size and size dispersity control strategies

As suggested before, size control has a tremendous impact on NC's properties due to affecting the quantum confinement of the material. In addition, obtaining a sample homogeneous in terms of size is crucial for its application in solar cells. This is because having particles of different sizes will result in slightly different E_g, which introduces energetic disorder in the system, triggering non-radiative recombination losses and trap centers for the photogenerated charge carriers. Several strategies have been reported to control the size and size distribution and include mostly the adjustment of the synthesis condition in terms of ligands and temperature.

Regarding the ligands, it was found that the number of carbons in the alkylic chain of the carboxylic acid and amine ligands can influence the size and shape of PNCs at a given temperature.[165,172,173] For instance, amines with a long alkylic chain in combination with oleic acid results in nanoplatelets with larger length compared to short amines.[173,174] The explanation for this phenomenon lies in the van der Waals interactions between the ligands, which are stronger for molecules with a long alkylic chain.[174] As a consequence of this interaction, the surface energy of the NC is higher for long-chain molecules, resulting in a natural tendency of the NCs to grow with a large size in order to minimize their surface-to-volume ratio and have better stability.[174] Another aspect to be considered is the higher solubility of long alkylic chain amines, which facilitates the growth of large-size NCs.[175] In addition to this chemical aspect regarding the nature of the ligands, the concentration of the ligands and Pb-source is also capable of modulating the size of the NCs.[134,139,176] Considering PNCs prepared from the LARP method, as the concentration of the Pb-source increases, more precursors are available in the reaction medium, allowing the formation of large NCs. Conversely, at a low concentration regime, the Pb-source becomes soluble in both polar and apolar solvents, so it is not observed in the precipitation of NCs. In the case of the ligands, a high concentration slows down the growth of the NC due to a decrease in the reactivity of the precursors since the ligand forms complexes with Pb^{2+}.[134]

The temperature of the synthesis also impacts the size, with higher temperatures resulting in larger NC. For instance, Otero-Martínez and collaborators showed that from 175 °C to 100 °C the MHP NC shape changes from 3D, with bulk-like properties, to 0D nanocubes, with a strong quantum confinement effect (Fig. 8a).[177] This is also valid for other NC compositions, such as $FAPbBr_3$, and $CsPbX_3$ (X = Cl, Br, I). As a consequence of the NC size variation, different emission peaks (corresponding to different E_g) were obtained.[177] Because of this intimate relationship between the NC size and the reaction temperature, controlling this parameter during the synthesis is crucial and it can be one of the causes of batch-to-batch non-reproducibility. The size dependence on the temperature can be explained in terms of the solubility of the PNCs precursors: as the temperature increases, their solubility increases, facilitating the formation of bigger nanocrystals due to reducing the supersaturation degree.[134] Other works also reported that temperature impacts the products obtained, the morphology, crystal phase, and purity of the PNC,[178–180] reinforcing the importance of fine control of the reaction temperature.

In addition to controlling the size and shape, the application of PNCs in solar cells also depends on the size distribution of the NCs. Having a sample with a broad size distribution means the existence of NCs with different bandgaps, which can result in charge funneling from the higher to the lower bandgap material and trap centers, which decreases the maximum photovoltage delivered by the device. Several strategies have been reported to control PNCs size distribution. Dong *et al.*,[181] for instance, introduced $ZnBr_2$ as an additional source of bromide and demonstrated that Br^--rich condition in the synthesis of $CsPbX_3$ NC through the hot-injection method helps to obtain narrow size distribution (<1 nm) and small size (<7 nm), as shown in Fig. 8b. Furthermore, an approach to prepare fixed-size NCs is growing them inside porous materials. Several porous materials have been tested, including silica,[182] nanoporous silicon, alumina,[183] and metal–organic frameworks[184] (Fig. 8c and d). In addition, the cooling rate of the reaction prepared from the hot-injection method can also impact the size distribution. The slow cooling of the reaction at room temperature, for instance, can prolong the nucleation and growth process, yielding wide-size distribution (Fig. 8e). To circumvent this issue, Luo *et al.* introduced an ultrafast thermodynamic control (UTC) strategy for $CsPbBr_xCl_{3-x}$ NCs.[185] This method consists of quickly cooling the reaction using liquid nitrogen at 77 K inserted directly into the reaction flask, immediately ceasing the NC growth, which allows a narrow size distribution, as shown in Fig. 8e. The authors combined the UTC strategy with the defect passivation of PbX_6^{4-} octahedra using $Pb(BrCl)_2$ salt to obtain strongly blue-emitting $CsPbBr_xCl_{3-x}$ NC with PLQY of 98%.

An elegant way to obtain samples of PNCs with a controlled size distribution is by employing gel permeation chromatography (GPC) (Fig. 8f). This method is routinely used in organic chemistry laboratories to separate mixtures of different products obtained from a reaction. A stationary phase, such as SiO_2 or Al_2O_3, and a mobile phase, *e.g.* chloroform, ethyl acetate, toluene, and diethyl ether, are used to provide the separation of the reaction's products. Each compound from the reaction mixture will interact differently with the stationary and mobile phases. Those that interact strongly with the stationary phase will be more retained, and will eluate from the column at later times. Conversely, those that interact strongly with the solvent, *i.e.* less interaction with the stationary phase, will eluate in early times. By collecting small aliquots of the solvent from the column it is possible to separate the mixture into (more) pure products. Translating this to PNC, GPC allows the narrowing of the polydispersity in a mixture of NC of different sizes, because of the different interactions that the small and the large NCs have with the stationary/mobile phase. This strategy has also been successfully used for the removal of unreacted materials from PNC synthesis,[186] the optimization of ligand binding strength with the outer shell of the NC, and ligand exchange.[187]

4.3 Morphology control strategies

The morphology of the nanocrystals can influence their stability, besides impacting the optoelectronic properties due to changes in the electronic structure.[188,189] Therefore, it is important to find ways to control the morphology of the NC during synthesis. The variation of solvent, ligand concentration, and reaction time, for instance, can tune the NC shape from quantum dots to nanoplates, nano bars, nanocubes, nanorods, and nanowires.[190] Besides, Zhang *et al.*[191] demonstrated that water content during the synthesis could change the NC shape: from spherical to square-shaped rectangular

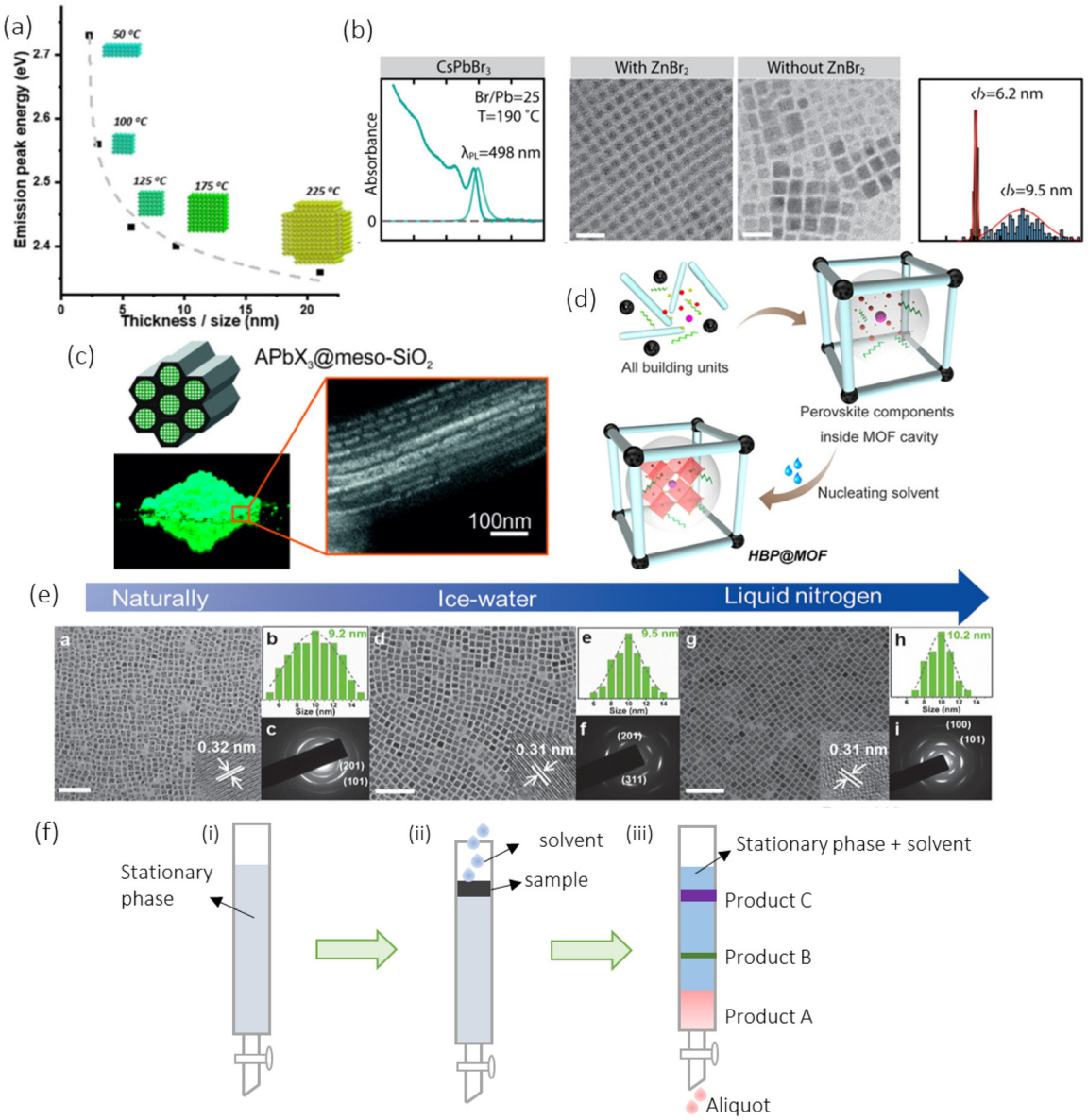

Fig. 8 (a) The dependence of the emission peak on the thickness/size of the NP can be controlled through the synthesis temperature.[177] (b) Influence of $ZnBr_2$ treatment on the NC size and size distribution for $CsPbBr_3$ PNC.[181] (c) Schematic illustration, scanning electron microscopy (SEM) image, and photography of the $APbX_3$ NC powder grown inside mesoporous SiO_2, that acts as a template for the NC grow.[182] (d) Schematic illustration of the NC growth inside the cavities of metal–organic framework (MOF).[184] In both (c) and (d) the size of the NC is controlled by the pore size of the template used, here mp-SiO_2 and MOF. (e) TEM images and size distribution diagram of the $CsPbBr_xCl_{3-x}$ NC obtained at different cooling methods.[185] (f) Schematic illustration of the purification using gel permeation chromatography. The sample and the solvent are added in the stationary phase (ii). As the solvent evolves, products A, B, and C are separated (iii) due to the differences in their interaction with the mobile/stationary phases. (b) Reproduced with permission from ref. 181. Copyright 2018 American Chemical Society. (c) Reproduced with permission from ref. 182. Copyright 2016 American Chemical Society. (d) Reproduced with permission from ref. 184. Copyright 2016 American Chemical Society. (e) Reproduced with permission from ref. 147. Copyright 2016 Wiley-VCH.

nanoplatelets and then nanowires of the $CsPbBr_3$ (Fig. 9a).[191] Since water can affect the morphology of the material, the control over the water level in the solvents used during the synthesis is a fundamental aspect. The shape variation comes with changes in the size, and the increase in the NC size is reflected as a red-shift of the absorption band, loss of the excitonic features, and increased PL lifetime (Fig. 9b and c). The increased size and shape caused by water was attributed to the decomposition of the small NC into their precursors, while other NC act as a seed to grow large ones.

The shape control is also possible through the adjustment of reaction temperature and the amount of Cs-precursor in the case of $CsPbBr_3$ PNC.[192] By increasing the Cs : Pb ratio, the NC shape evolves from 2D nanoplatelets to 0D nanocrystals, with

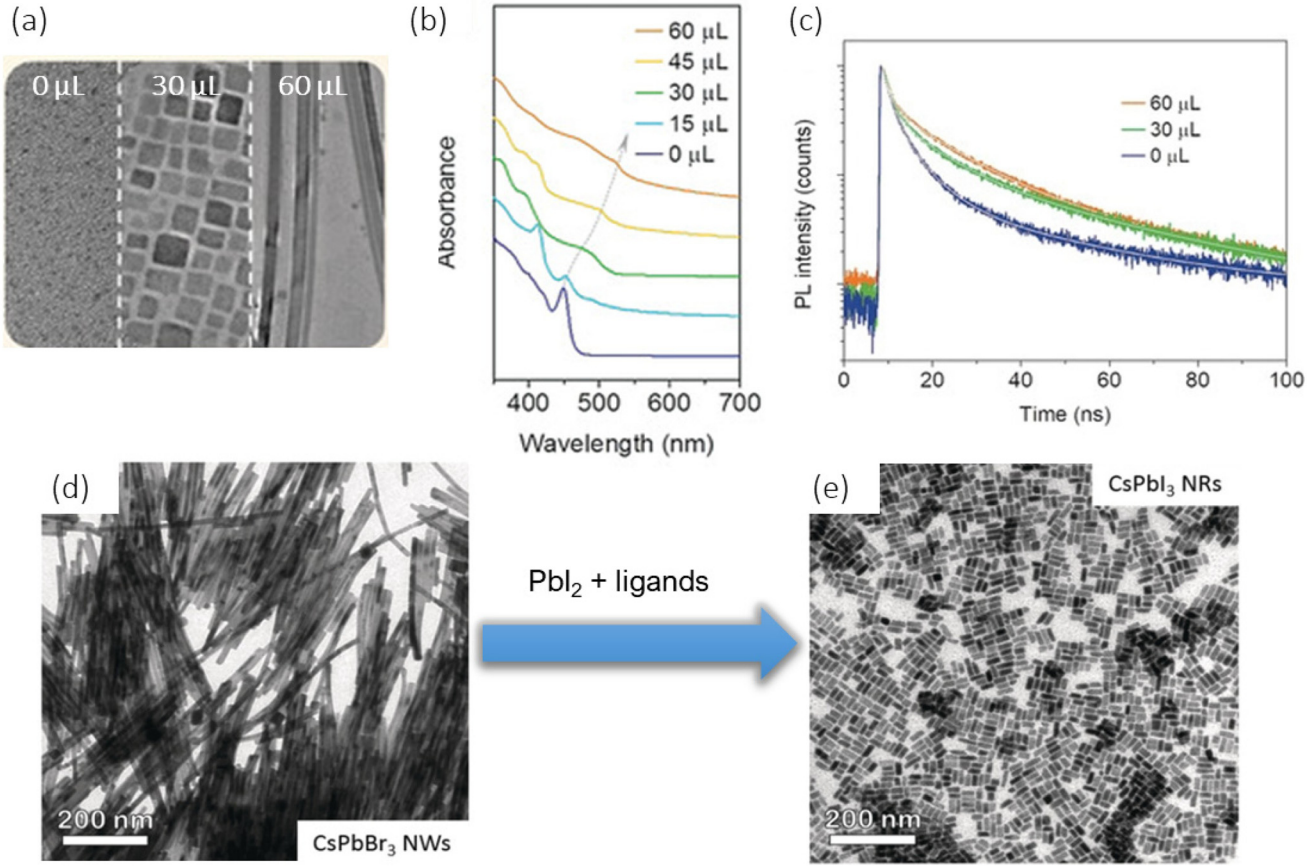

Fig. 9 (a), (b), and (c) Show the transmission microscopy images, absorption features, and PL decay curves, respectively, of $CsPbBr_3$ NCs prepared with different amounts of water.[191] (d) and (e) TEM images of $CsPbBr_3$ and the $CsPbI_3$ NC obtained after the halide ion exchange reaction with PbI_2.[193] (a–c) Reproduced with permission from ref. 147. Copyright 2018 Wiley-VCH. (d and e) Reproduced with permission from ref. 193 Copyright 2018 Wiley-VCH.

dimensions of (8.6 × 10) nm and a diameter of 17.4 nm, respectively. Fixing the Cs : Pb ratio and increasing the reaction temperature from 120 to 185 °C, the morphology goes from thin nanoplatelets with (7.5 × 2.5) nm dimension to a cubic shape with 10.5 nm length. Also, the anion exchange reaction was demonstrated to change the morphology of the NC.[193] Anion exchange reaction is used to change the composition of the pre-synthesized NC and occurs through the diffusion from an ion in solution to the interior of the material, a process controlled by the diffusion both outwards and inwards, and the ion exchange rate.[194] Generally, this methodology retains the morphology of the MHP NC,[195,196] but this was not what Tong and collaborators demonstrated.[193] By replacing Br^- with I^-, or Cl^- in $CsPbBr_3$ NC, the authors verified that morphology changes from nanowires with 1–2 µm and width of 12 nm, to nanorods with a low aspect ratio (Fig. 9d and e). The morphology change causes a blueshift in the absorption and emission spectra, and also increases the PLQY from 10% in the $CsPbBr_3$ nanowires to 47% in $CsPbI_3$ nanorods. This shape variation is attributed to the excess of ligands present in the PbX_2 precursor solution, which causes the random fragmentation of the nanowires forming the nanorods.

5. PNC solar cells

After discussing the main characteristics of the PNCs as well as the common methods to prepare them, we will address the application of these materials in solar cells. In a typical PNC solar cell, the photoactive layer, comprised of the PNCs, is deposited between the hole and electron extraction layer, allowing selective collection of the photogenerated charge carriers (electrons and holes) and further extraction to the cathode and anode, top and bottom electrode, respectively. The most common architecture used to fabricate PNC solar cells is the nip-type (Fig. 10a), in which the photoactive layer is deposited onto the electron transport material (ETM, *e.g.* SnO_2 or TiO_2), and covered by a hole transport material (HTM, *e.g.* Spiro-OMeTAD or PTAA).

The first report on PNCs applied in solar cells dates from 2016, when Swarnkar *et al.*[26] used 9 nm cubic α-$CsPbI_3$ QDs to fabricate a nip-type solar cell with TiO_2, as the ETM, and Spiro-OMeTAD, as the HTM. The device delivered an efficiency of 10.77%, with an open-circuit voltage (V_{OC}) of 1.23 V, short-circuit current (J_{SC}) of 13.47 mA cm^{-2}, and fill factor (FF) of 65.0%. Since then, numerous strategies have been proposed to

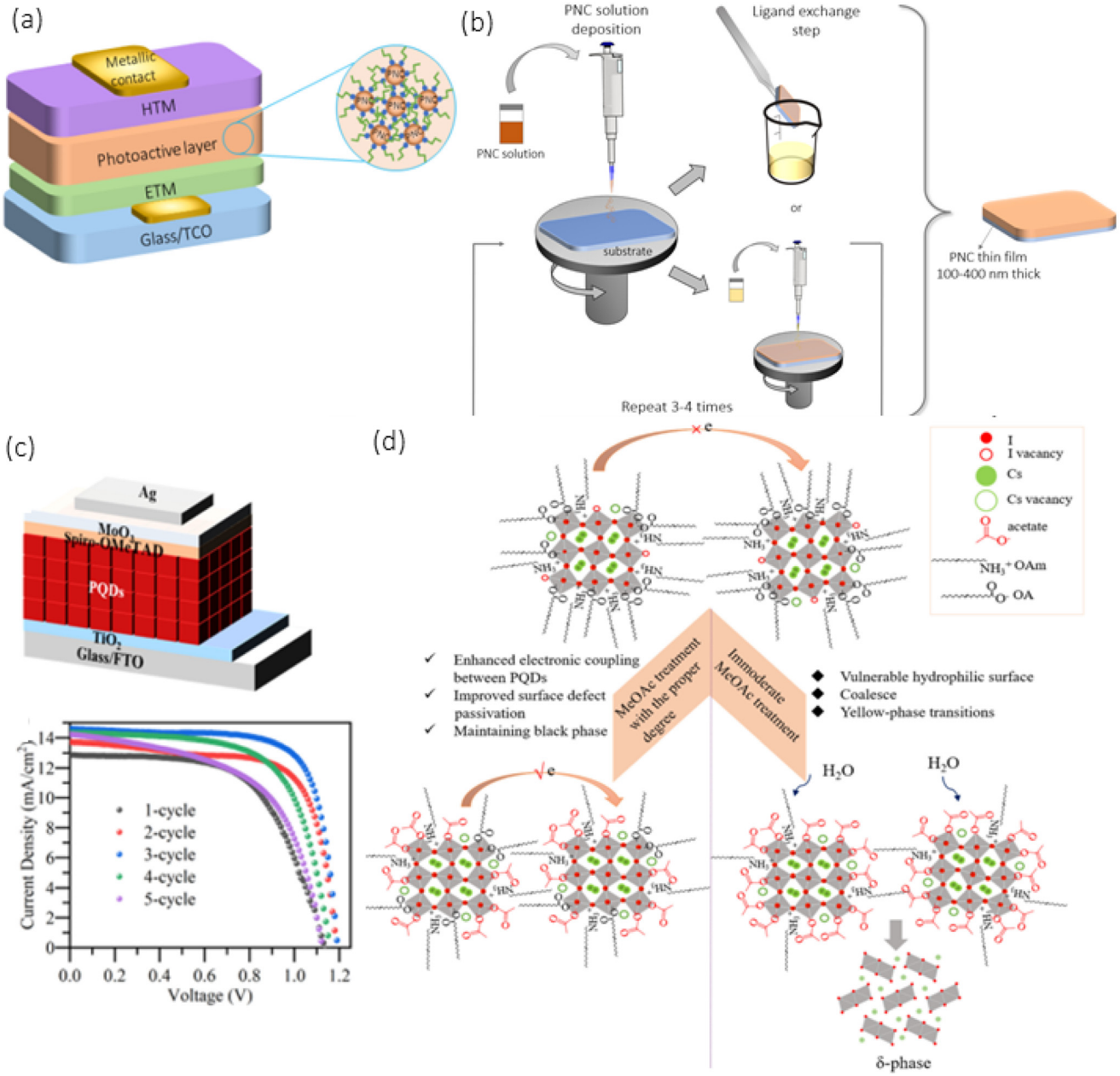

Fig. 10 (a) Schematic illustration of a PNC solar cell with a nip-type architecture. Here, TCO is the transparent conductive oxide (*e.g.*, ITO or FTO); ETM is the electron transport material (*e.g.*, SnO_2, TiO_2); and HTM is the hole transport material (*e.g.*, Spiro-OMeTAD, PTAA). (b) Scheme of the PNCs deposition by spin-coating for solar cell fabrication. In the first step, a solution containing the PNC is deposited onto the desired substrate. Following this, the ligand exchange step is realized. (c) Scheme of a PNC solar cell and the resultant current density *vs.* voltage (*JV* curve) obtained after 1, 2, 3, 4, and 5 successive cycles of solution deposition and ligand exchange.[214] (d) Proposed mechanism of the effect of the MeOAc treatment on the PNC surface.[214] (c and d) Reproduced with permission from ref. 214 Copyright 2021 American Chemical Society.

improve solar cell efficiency, either by management of the PNC synthesis and deposition or by passivation of device interfaces. In Table 1 we provide a summary of the recent achievement in PNC solar cells together with the method used to prepare the NC and the solar cell architecture, and the bandgap of the active layer, which will influence the photon absorption. We can see that most of the devices are prepared using the regular nip-type architecture, with TiO_2 and Spiro-OMeTAD being the ETM and HTM materials, respectively. Also, the NCs of the photoactive layer are usually synthesized from the hot injection method, probably because this is an established procedure for NC synthesis, and allows versatility in terms of NC composition and shape, which can influence the optoelectronic properties of the material and, consequently, the photovoltaic efficiency of the solar cell. Among the works reported in Table 1, we highlight the efforts made by Hao *et al.*[197] and by

Table 1 Summary of the photovoltaic parameters of some perovskite nanocrystal solar cells reported from 2018 to 2022

Solar cell architecture	Synthesis method	E_g (eV)	V_{OC} (V)	J_{SC} (mA cm^{-2})	FF (%)	PCE (%)	Year	Ref.
FTO/TiO_2/$CsPbI_3$ NC/PTB7/MoO_3/Ag	Hot injection	1.73	1.27	12.39	80.0	12.55	2018	199
ITO/SnO_2/$FAPbI_3$ NC/Spiro-OMeTAD/Au	Hot injection	1.55	1.10	11.83	64.42	8.38	2018	200
ITO/ZnO/$Ba(OH)_2$/$FAPbI_3$ NC + conductive polymer/MoO_x/Ag	LARP	—	0.56	15.22	65.41	5.51	2018	201
FTO/TiO_2/α-$CsPbI_3$ + $FAPbI_3$ NCs/PTAA/MoO_3/Ag	Hot injection	1.30 (α-$CsPbI_3$) 1.36 ($FAPbI_3$)	1.22	17.26	74.0	15.6	2019	198
FTO/TiO_2/$CsPbBr_3$ NC/Spiro-OMeTAD/Au	Hot injection	2.30	1.34	9.41	36.0	4.57	2020	202
FTO/TiO_2/$CsPbI_3$ NC/PTAA/MoO_3/Ag	Hot injection	1.29	1.22	75.0	15.1	13.8	2020	203
FTO/TiO_2/$FAPbI_3$ NC/PTAA/MoO_3/Ag	Hot injection	1.37	1.12	16.7	71.0	13.2	2020	203
FTO/TiO_2/$CsPbI_3$ NC/PTAA/MoO_3/Ag	Hot injection	—	1.24	15.84	75.50	14.9	2020	204
ITO/SnO_2/$CsPbI_3$ NC/Spiro-OMeTAD/Ag	Hot injection	~1.75	1.22	17.66	63.38	13.66	2020	205
FTO/TiO_2/α-$CsPbBr_3$ NC/PTAA/MoO_3/Ag	Hot injection	2.38	1.54	4.49	72.45	5.01	2020	206
FTO/NiO_x/$CsPbI_3$ NC/C_{60}/ZnO/Ag	Hot injection	1.76	1.19	14.25	77.6	13.10	2020	207
ITO/SnO_2/$Cs_{0.5}FA_{0.5}PbI_3$ QD/Spiro-OMeTAD/Au	Hot injection	1.64	1.17	18.3	78.3	16.6	2020	197
FTO/TiO_2/$CsPbI_3$ NC/Spiro-OMeTAD/MoO_3/Ag	Hot injection	—	1.27	16.1	74.8	15.3	2021	208
ITO/SnO_2/PCBM@$CsPbI_3$/$CsPbI_3$ NC/PTB7/MoO_3/Ag	Hot injection	1.77	1.26	15.2	78.0	15.1	2021	209
FTO/TiO_2/$CsPbI_3$ NC/PTAA/MoO_3/Ag	Hot injection	1.77	1.26	15.81	75.3	15.05	2021	210
FTO/TiO_2/$CsPbI_3$ NC/$CsPbI_3$ NC:F6TCNNQ/PTAA/MoO_3/Ag	Hot injection	1.77	1.25	16.90	71.0	15.01	2021	211
FTO/TiO_2/$MAPbI_3$ NC@SiO_2/Spiro-OMeTAD/Au	*In situ* synthesis @SiO_2 matrix	—	1.02	16.42	56.1	9.3	2021	212
FTO/TiO_2/$CsPbI_3$ NC/Spiro-OMeTAD/Ag	Hot injection	1.80, 1.79, 1.78[a]	1.25	14.9	71.0	13.2	2021	213
FTO/TiO_2/$CsPbI_3$ NC/Spiro-OMeTAD/MoO_3/Ag	Hot injection	—	1.19	14.59	73.85	12.85	2021	214
FTO/m-TiO_2 + $CsPbI_{2.25}Br_{0.75}$ QD/$CsPbI_{2.25}Br_{0.75}$ QD/Spiro-OMeTAD/Au	Hot injection	1.87	1.20	14.21	72.1	12.31	2021	215
ITO/SnO_2/$CsPbI_3$ QD/Spiro-OMeTAD/Ag	Hot injection	—	1.27	17.71	72.0	16.21	2021	216
PET/ITO/SnO_2/$CsPbI_3$ QD/PTB7/MoO_3/Ag	Hot injection	1.77	1.24	13.6	73.0	12.3	2021	209
FTO/TiO_2/Ag:$CsPbBr_{1.5}I_{1,5}$/Spiro-OMeTAD/MoO_3/Ag	Hot injection	2.12	1.04	12.51	74.0	9.67	2021	217
ITO/PEDOT:PSS/α-$CsPbI_3$ NC/C_{60}/BCP/Al	Colloidal synthesis	1.93	0.98	16.21	67.3	10.06	2022	218
FTO/c-TiO_2/$CsPbI_3$ QD/Spiro-OMeTAD/MoO_x/Ag	Hot-injection method	~1.77	1.24	15.4	71.3	13.7	2022	219
ITO/SnO_2/$CsPbI_3$ QD/Spiro-OMeTAD/Ag	Modified hot-injection method	1.77	1.23	17.73	74.5	16.25	2022	28
ITO/PEDOT:PSS/$FAPbI_3$ QD/PCBM/BCP/Ag	Modified hot-injection method	1.55	0.89	14.56	89.0	10.13	2022	220
FTO/TiO_2/$Cs_{0.5}FA_{0.5}PbI_3$ QD/PTAA/MoO_3/Ag	Hot-injection method	~1.63	1.19	16.82	72.4	14.58	2022	221
FTO/c-TiO_2/m-TiO_2/$CsPbI_3$ QD/PMMA/$Cu_{12}Sb_4S_{13}$ QD/Au	Hot injection	—	1.14	16.14	53.1	10.99	2022	222

[a] Active layer prepared with NC with different sizes.

Li *et al.*[198] obtaining efficiencies of 16.6% and 16.2%, respectively, for nip-type architecture with $Cs_{0.5}FA_{0.5}PbI_3$ and $CsPbI_3$ QD as the active layer, respectively. To the best of our knowledge, these are the highest efficiencies for PNC solar cells reported so far. Compared to the first report in 2016,[26] the performance gain in only six years is superior to 60%.

5.1 Preparation of PNC solar cells

The preparation of PNCs thin film for application in solar cells is not as straightforward as it may seem. It requires sequential deposition of layers of the material from a solution in an apolar solvent, *e.g.* octane, using spin-coating (or other) technique (Fig. 10b). Besides, the insulating nature of the capping ligands that came from the synthesis, *e.g.* OA and OLA, preclude the proper charge separation inside the NC layer and the charge extraction to the charge selective contacts in the device. Therefore, it is necessary to replace these long and insulating chains with short ones (Fig. 10b), aiming to improve the NC-NC electronic coupling.[223] From one side, this ligand exchange step introduces additional complications to the device manufacture but, on the other side, it is an excellent opportunity to heal defects present on the NC surface. Indeed, defect passivation is a key point of any solar cell technology. In the case of PNC solar cells, both the defects present on the NC surface and on the device's interfaces (*e.g.*, interface ETM/active layer and active layer/HTM) should be passivated. These defects can induce non-radiative recombination of charge carriers, and the physical/electronic mismatch between the PNC layer and the other layers of the device can compromise FF and J_{SC}.[224] In this section, we will discuss the fabrication of PNC solar cells and emphasize how the ligand exchange step and interfacial treatments on the device can be used to improve its efficiency and stability.

5.1.1 Active layer preparation. The deposition of the PNC onto the electron, for nip-architecture, or hole transport material, for pin-architecture, starts with a dispersion of the NCs in an appropriate solvent, typically, octane or hexane.[225–228] Sometimes this solution is filtered using nylon filters to avoid the presence of large-size NC in the final film, which could result in a non-homogeneous film, compromising

photovoltaic performance. Next, the ink solution is deposited onto the substrate. Several techniques can be employed, highlighting spin-coating, drop-cast, dip-coating, inkjet printing, blade coating, and slot die coating.[18] Commonly, to obtain a layer thick enough to generate appreciable photocurrent (in the range of ~300–400 nm), several steps of PNC ink solution deposition are required. After that, the hole transport layer is deposited, and finally, metallic contact is thermally evaporated.

5.1.2 The ligand exchange step. After the PNC solution deposition, it is necessary to remove/replace the long capping agents that are used in the synthesis since the insulating nature of these organic chains will preclude the efficient charge separation and extraction in the device. Usually, this is made by a ligand exchange process, which consists of, after each step of PNC layer deposition, dipping the film into (or dripping onto the film) a solution of methyl acetate (MeOAc) containing $Pb(OAc)_2$ or $Pb(NO_3)_2$; this is the most classical procedure used.[26] The mechanism of this exchange lies in the hydrolysis of the MeOAc to generate acetic acid and free methanol molecules. The first can protonate the NC-oleate bonding, replacing the oleate ligands from the NC surface, and generating free oleic acid as a subproduct that is washed out from the film.[229]

There are several effects of this treatment on solar cell performance. From one side the short alkyl chain replaces the long ligands coming from the synthesis, improving the electronic coupling between the NCs, which in turn improves the charge separation in the device, allowing higher values of V_{OC} and J_{SC}.[229,230] On the other side, lead salts are a source of Pb^{2+} ions, which passivates Lewis base defects present on the NC surface.[26] Using this protocol, devices based on $CsPbI_3$ NC with efficiencies of ~10% can be obtained.[26] The sequential repetition of the spin-coating deposition and washing steps can yields thin films with thicknesses varying from 100 to 400 nm, conferring the possibility to fabricate films thin enough to be integrated into flexible and semitransparent devices.

Although the ligand exchange improves the efficiency of the PNC solar cell when compared to the device fabricated using NC with large alkyl chains, it is necessary to control the number of MeOAc dipping steps.[214] As shown in Fig. 10c and d, the number of washing steps can significantly impact the device's performance. For instance, the current density *versus* voltage (*JV*) curve in Fig. 10c shows that only one step of washing (1-cycle) results in low V_{OC}, J_{SC}, and FF compared to 3-cycles. Further increase in the number of washing cycles above three causes the decrease of all photovoltaic parameters. A proposed explanation is that a few steps will not remove an appreciable amount of long-chain ligands, while excessive steps can cause the formation of the yellow perovskite phase;[214] both will compromise the device's efficiency and stability. In this sense, a balance is necessary, and three washing steps seem to be the most appropriate to replace the long capping ligands with short ones and improve the PNC solar cell performance.

As can be inferred from the last paragraphs, the ligand exchange is one of the most important steps in the PNC solar cell assembly, as it will influence the coupling between the NC, impact the defect density of states on the surface, and affect the device efficiency. Given its importance, several strategies based on ligand exchange modifications have been used to improve the performance and stability of the PNC solar cell, with the possibility to add different molecules to confer passivation of the NC surface; some examples of the molecules are shown in Fig. 11a. It should be highlighted that the choice of the molecule and type of treatment realized on the NC to replace the ligands will depend on the nature of the capping ligands, and on the composition of the NC since it influences the binding strengths between the ligand-NC surface.

An alternative to the conventional $Pb(NO_3)_2$/MeOAc mixture was demonstrated using hexane/ethyl acetate (EtOAc).[231] This solvent mixture was able to remove ~57% of the long capping ligands, causing an increase in the NC size from 7.8 to 10.1 nm, and leading to a PCE improvement from 5.9% to 12.2%, respectively. This is possible since the coordinating ability of the ethyl acetate molecule, which is capable of replacing some ligands from the nanocrystal surface. In addition, it is possible to use functionalized ligands, such as amino acids. These bidentate ligands are shorter than OA and OLA ligands, causing a better electronic coupling between the NC and conferring a dual passivation effect on the surface due to the presence of carboxyl (–COOH) and ammonium ($-NH_3^+$) groups in the same molecule.[205] Fig. 11b shows a schematic illustration of this passivation effect conferred by the amino acids when compared to MeOAc, in which we can see the passivation of Cs^+ and I^--related defects. Applying these molecules during the ligand exchange process resulted in PNC solar cells with the architecture ITO/SnO_2/$CsPbI_3$ NC/Spiro-OMeTAD/Ag with efficiency up to 13.7%, presenting improvements in V_{OC}, J_{SC}, and FF when compared to the ligand exchange performed with $Pb(NO_3)_2$, as indicated in Fig. 11c.[205] This value is 2% higher than the obtained for the ligand exchange using $Pb(NO_3)_2$/MeOAc mixture, which evidences the key role of the short and functionalized ligands. Another alternative is the use of pyridine derivatives, such as mercaptopyridine (MP) in MeOAc solution.[232] This approach resulted in solar cells (FTO/TiO_2/$CsPbI_3$ NC/PTAA/MoO_3/Ag) with efficiencies of ~14% (*versus* 12% for the control devices), and negligible hysteresis. It is interesting to stress that the position of the mercapto (–SH) group in MP impacts both device performance and stability: in the *ortho* position, –SH experiences hysterical hindrance to binding on the NC surface, difficulting the defect passivation and negatively impacting the device's stability (Fig. 11d) and efficiency (which decreases to 13.09%). Conversely, when the mercapto group is in the *para* position both efficiency and stability were increased, highlighting the importance of molecular engineering strategies in the design of new passivating candidates. This type of treatment, which includes both improvements in performance and stability, is of central importance, since, with time, the ligand desorption in the thin film can difficult the maintenance of stable photo-

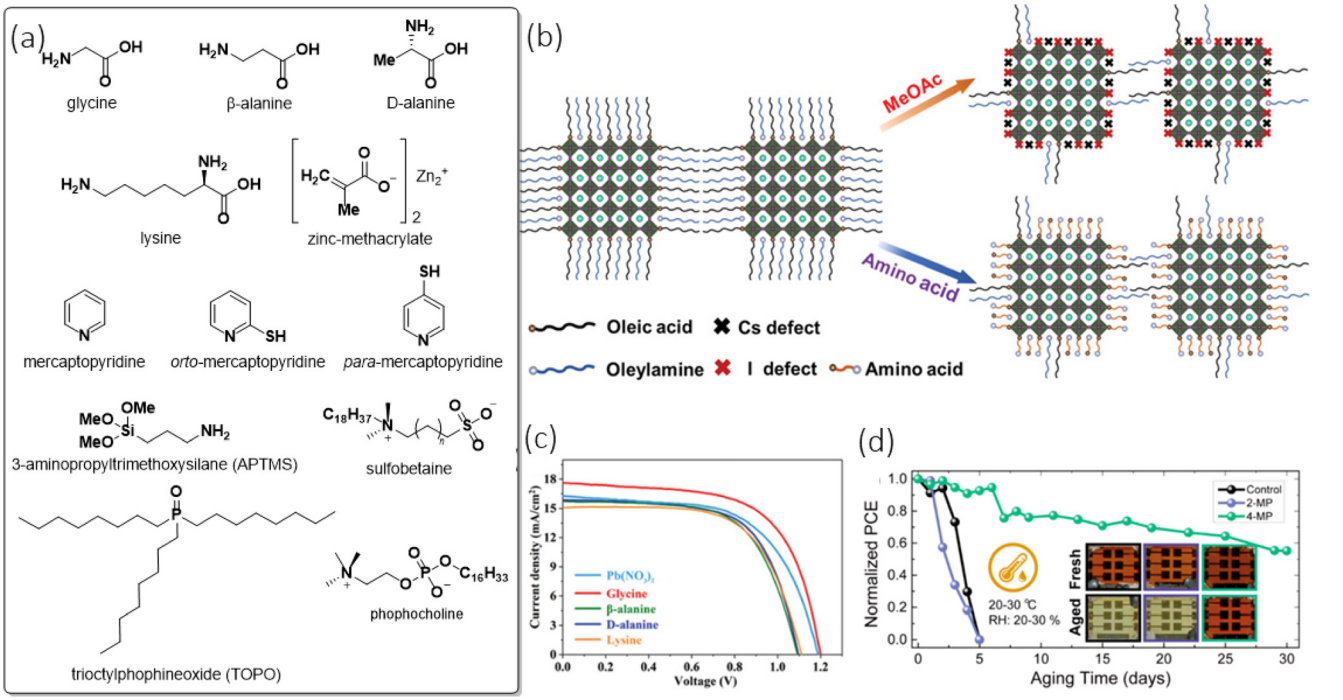

Fig. 11 (a) Molecular structure of some passivating molecules used for the surface passivation of PNC. (b) Schematic illustration of the defect passivation ability of amino acids *vs.* methyl acetate (MeOAc) used during ligand exchange.[205] (c) Comparison of *JV* curves of control PNC solar cell using $Pb(NO_3)_2$ in MeOAc and using amino acids dissolved in MeOAc.[205] (d) Evolution of the PNC solar cell performance with time in an environment with 20–30% of humidity and temperature of 20–30 °C. Here is shown the effect of the mercapto group position in the mercaptopyridine (MP) molecule used during the ligand exchange step.[232] (b and c) Reproduced with permission from ref. 205. Copyright 2020 Wiley-VCH. (d) Reproduced with permission from ref. 232. Copyright 2020 American Chemical Society.

active phases,[161,233] induces aggregation, and consequent loss (or attenuation) of the quantum confinement effects, compromising the device performance. Therefore, it is important to look carefully not only at the nature of the functional group present on the molecule and its isolated interaction strength with the NC surface defects, but also at its position on the molecule and the steric hindrance for the interaction with the NC. Other functionalized molecules can also be explored to be used during the ligand exchange step, including chiral ligands,[234] methoxy silane-based molecules,[235] potassium bromide,[236] zinc methacrylate (ZnMA), trioctylphosphine oxide (TOPO) co-passivation,[237] and zwitterions, as sulfobetaine and phosphocholine.

A different approach for the photoactive layer was proposed by Zhao *et al.*[227] They used the versatility of PNCs to be synthesized in a giant plethora of compositions to prepare an active layer consisting of a QD heterojunction. That is, each layer was deposited with a different ratio of $CsPbI_3$ and $FAPbI_3$ QD, forming $Cs_{1-x}FA_xPbI_3$ QD. The controlled composition of each layer allows a boosting of the charge separation extraction inside the QD layer, achieving efficiencies of nearly 17%. Similar control of the band alignment on the PNC layers was reported by Yuan *et al.*[213] The authors used layer-by-layer deposition of $CsPbI_3$ NC with different sizes to prepare the photoactive PNC layer, which allows gradient band alignment, improving the device performance from 10.3 to 13.2%, with V_{OC} of 1.25 V.

5.1.3 Device interface passivation strategies. As briefly mentioned before, most of the PNC solar cells are fabricated using the regular nip-type architecture, probably because of the better adhesion of the NC in the conductive metal oxide layer, *e.g.* TiO_2, which acts as a support for the NC. Usually, TiO_2 is the ETM whereas Spiro-OMeTAD is the HTM; see Table 1. The adoption of mesoporous (mp) TiO_2 typically results in higher device performance because of the larger contact area for electron extraction. However, its integration in PNC solar cells is tricky, and interface engineering strategies are required. This is because the PNC deposited onto mp-TiO_2 forms a very irregular film that can cause efficiency loss due to inefficient charge separation and the formation of defects in the photoactive layer, compromising V_{OC}, J_{SC}, and FF.[238,239] Chen *et al.*,[238] treated the mp-TiO_2 film with a solution of CsOAc in MeOAc before the deposition of the PNC layer. They found that MeOAc is capable of reconstructing the (001) surface of the TiO_2 layer by breaking Ti–O bonds, facilitating the entrance of the PNC into the mesoporous layer, as depicted in Fig. 12a. In addition, Cs^+ coordinates with the TiO_2 surface and removes trap states on the surface of the NC, as evidenced by the lower trap-filled limited voltage (V_{TFL}) obtained from space charge limited current (SCLC) measurements (Fig. 12b). This strategy allowed the efficiency of solar cells based on FTO/c-TiO_2/mp-TiO_2/PNC/Spiro-OMeTAD/Au to increase from 5% to 14% upon CsOAc/MeOAc treatment. Furthermore, it was found

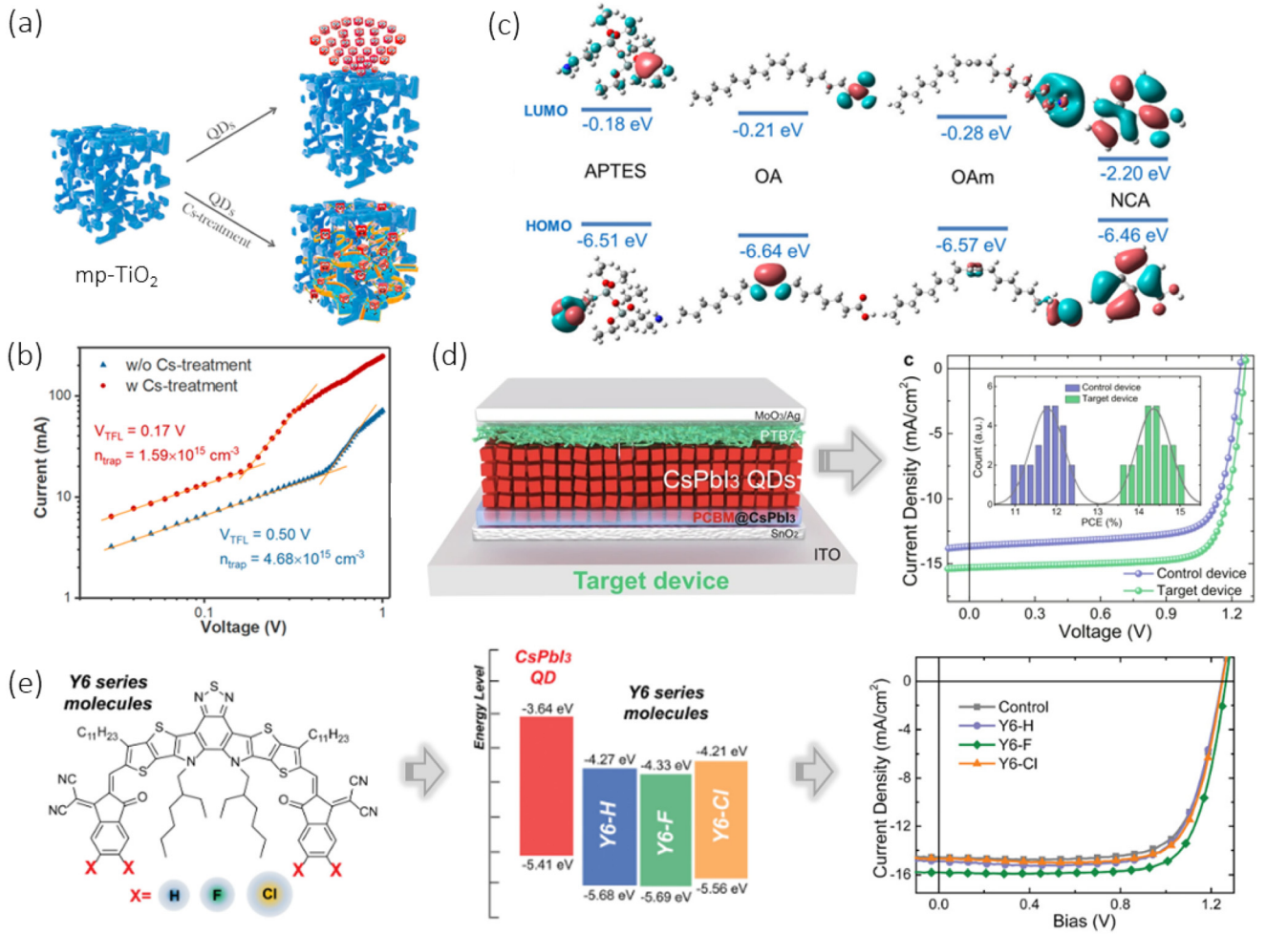

Fig. 12 (a) Schematic illustration of the effect of CsOAc treatment on mp-TiO_2 layer to facilitate the penetration of the PNC.[238] (b) Space-charge limited current (SCLC) measurements of electron-only devices with a structure of ITO/TiO_2/$CsPbI_3$ PNC/PCBM/Ag.[238] (c) Distribution of the ligand's energy level and energetic position of the respective HOMO and LUMO. (3-Aminopropyl)triethoxysilane (APTES), oleic acid (OA), oleylamine (OAm), naphthoic acid (NCA).[240] (d) Schematic diagram of the PNC solar cell assembled with the PCBM:PNC blend and the respective *JV* curve.[209] (e) Comparison between the energy level of the $CsPbI_3$ QD and a series of Y6 molecules. On the right side, it is shown a comparison between the *J*–*V* curves obtained for QD:Y6 blend and the control device.[210] (a and b) Reproduced with permission from ref. 238. Copyright 2020 American Chemical Society. (c) Reproduced with permission from ref. 240. Copyright 2021 De Gruyter. (d) Reproduced with permission from ref. 209. Copyright 2021 Nature. (e) Reproduced with permission from ref. 210. Copyright 2021 Wiley-VCH.

that the electron transfer from the PNC to TiO_2 can be controlled by changing the nature of the ligands used to prepare the NCs.[240] Liu *et al.* used aromatic ligands, *e.g.* naphthoic acid (NCA), in $CsPbBr_3$ NC and verified an increased electron transfer to mp-TiO_2 when compared to alkyl chains (oleic acid (OA) and oleylamine (OAm)), and cross-linked ((3-aminopropyl)triethoxysilane (APTES)) ligands.[240] They attributed this effect to a deeper LUMO energy level of the aromatic ligand (Fig. 12c), providing a better energy match with the conduction band of mp-TiO_2. Also, the electron wave function is more spread out over NCA compared to OA, OAm, and APTES, which facilitates charge separation and extraction (Fig. 12c). This finding evinces the importance of ligand nature management to obtain more efficient devices.

Tin dioxide (SnO_2) is an alternative to TiO_2. It offers a good energy level match with the perovskite layer, high electron mobility, and conductivity, and less photocatalytic activity, which can help improve the device's stability.[241] Usually, this layer is deposited onto the conductive transparent oxide, *e.g.* indium tin oxide (ITO) or fluorine-doped tin oxide (FTO), from a SnO_2 QD dispersion in water. The Cl-doping of SnO_2 QD solution through the use of Cl-based salts, for example, KCl, was found to promote the passivation of oxygen vacancies on the film and improve the cubic-phase stability of $CsPbI_3$ QD that is deposited on top due to reducing V_{OC} loss.[242] The benefits of the Cl-passivated SnO_2 layer resulted in a champion efficiency of 14.5% (against 13.8% of the TiO_2-based PNC solar cell), which can keep 80% of the initial efficiency after 8 h of light soaking in an environment with 50% of relative humidity. Another alternative for SnO_2 passivation is the use of hybrid interfacial architecture. Hu *et. al*,[209] deposited a blend of $CsPbI_3$ QD (10 nm size) and PCBM electron acceptor onto

the SnO_2 layer. The integration of this blend in a solar cell based on ITO/SnO_2/PCBM@$CsPbI_3$-QD/$CsPbI_3$-QD/PTB7/MoO_3/Ag caused an efficiency improvement from 12% (without the blended active layer) to 15.1% (Fig. 12d).[209] The reason behind the improvement is the coordinating effect of the ester groups present on the PCBM, allowing the passivation of Pb^{2+} defects on the surface. Moreover, the energy level of the small molecule provides an energy level cascade, helping the charge extraction to the ETM. Also, it should be considered that PCBM has an electron acceptor character, which can help the electron extraction from the NC layer to the SnO_2. The same strategy was also demonstrated to be efficient in TiO_2/PNC interface using non-fullerene acceptors (*e.g.*, Y6 (Fig. 12e)).[210] It was found that by blending $CsPbI_3$ with Y6 a type-II energy level alignment is obtained, and the organic molecule passivates Pb^{2+} defects on the surface of the NC. PSC based on the architecture FTO/TiO_2/blended active layer/thin QD layer/PTAA/MoO_3/Ag yielded efficiencies as high as 15%, with main improvements observed in J_{SC} and V_{OC}, outperforming the 13.2% efficiency obtained for the device based only in $CsPbI_3$ QD.

Post-passivation of the PNC layer has also been demonstrated to passivate defects. This strategy consists in modifying the surface of the PNC layer after its deposition, being efficient to improve the PLQY,[243] photostability,[244] and external quantum efficiency (EQE).[245] In general, the mechanism of passivation conferred by this approach lies in the improved electronic coupling between the NCs and surface passivation conferred by surface-layer post-treatment.[246] For example, cesium salts, such as cesium acetate, in EtOAc solution, can increase the PNC solar cell efficiency from 12.6% (control) to 14.1% when used as a post-passivation at the NC layer.[247] This improved performance is due to a synergetic effect of both Cs-salt and EtOAc: the first fill Cs-vacancies on the surface caused during the ligand-exchange step, and the second helps in the additional remotion of capping ligands on the surface of the QD. Another strategy is to use hydrophobic conjugated molecules on the surface, such as phenylethylamine and its derivatives, which will replace some ligands on the NC surface.[219,248,249] These molecules are capable of improving the charge carrier delocalization in the PNC, which in turn improves the charge separation efficiency.[250] Also, AX salts (A = guanidinium, formamidinium) have been used in the post-passivation of the PNC layer.[207,251] The efficiency improvement achieved by using these salts comes from an improved charge extraction, enhanced electronic coupling, and their ability to maintain the cubic-NC phase unaltered.

5.2 Perovskite nanocrystals *vs.* bulk perovskites

We will focus here on two advantages of the PNCs compared to the bulk perovskite solar cell (PSC): (i) the high V_{OC} that can be achieved,[230] and (ii) the possibility to stabilize certain perovskite phases that are not stable in bulk form.[252]

Regarding V_{OC}, small losses have been observed for higher bandgap (>1.7 eV) materials, which benefits the achievement of high open-circuit voltages; the mechanism behind will be explained later on. The widening of the bandgap can be obtained, for instance, by alloying Br^- with I^- in the X-site of PNC (Fig. 13a) yielding V_{OC} as high as 1.31 V, and delivering 5.3% efficiency.[253] However, the inclusion of bromide usually increases the non-radiative recombination loss in the system. To circumvent this issue it was found that the concomitant incorporation of FA^+ and Br^- in $CsPbI_3$ NC is beneficial to decrease photovoltage loss (Fig. 13b).[215,254,255] Devices assembled with the architecture FTO/TiO_2/$FA_xCs_{1-x}Pb(I_{1-x}Br_x)_3$ PNC/Spiro-OMeTAD/MoO_x/Al yielded V_{OC} as high as 1.25 V and 1.27 V, for E_g equals 1.82 eV and 2.03 eV, respectively, and maximum PCE of 5.3% and 2.5%, respectively.[254] Additional advances were obtained for $CsPbBr_3$ NC-based solar cells; this perovskite composition can be prepared with bandgaps in the range of 2.38 to 2.46 eV, depending on the synthesis temperature employed.[256] For $CsPbBr_3$ NCs, Cho *et al.*[257] reported a solvent engineering strategy during the ligand exchange step consisting in mixing carboxylate solvents, such as EtOAc and butyl acetate (BuOAc), that resulted in an improved electronic coupling between the QDs. This approach yielded PNC solar cells with an efficiency of 4.2%, and an impressive 1.6 V of V_{OC}. As a matter of comparison, the V_{OC} of bulk $CsPbI_3$ or $CsPbI_{3-x}Br_x$-based solar cells is typically <1.10 V. The possibility of obtaining wide bandgaps makes PNCs particularly interesting for application as the bottom layer in the perovskite-perovskite, or perovskite-silicon tandem solar cells.[258] One of the origins of the high V_{OC} in PNC solar cells is the formation of surface traps during the ligand exchange step.[255] These traps increase the background free charge carrier in the QD, which maximizes the quasi-Fermi level splitting, decreasing V_{OC} losses.[255] However, it should be highlighted that the bandgap opening is a double-edged sword: if from one side it increases the maximum V_{OC} delivered by the solar cell, it dislocated the material's absorption towards the high-energy region of the solar spectrum, causing consequent J_{SC} loss.[254]

Concerning phase stability, the use of NC with composition analog to perovskite bulk materials allows stabilization of given phases otherwise unstable. For instance, the photoactive (α-phase) and the non-photoactive (δ-phase) of 3D $CsPbI_3$ are metastable at room temperature, which means that these two phases coexist and are interchangeable (Fig. 13c).[254,259] The stabilization of the desired bulk α-$CsPbI_3$ phase is only achieved at high temperatures (>150 °C),[260–262] and this material is prone to oxygen and moisture degradation, which can be attributed to its low tolerance fact or (0.803).[263] For that reason, it is quite hard to obtain long-term stability in bulk $CsPbI_3$-based solar cells, and the exposure of the unencapsulated device to ambient air results in the irreversible formation of the yellow non-photoactive phase.[264,265] On the other hand, PSCs prepared using $CsPbI_3$ NCs ($E_g \sim 1.72$ eV, excellent for top-cell in tandem solar cells), are not only more stable under ambient conditions compared to the bulk analog, but also allow stabilization of the photoactive phase at room temperature.[266,267] A decrease in the NC size accompanied by an increase in the CsI content during the synthesis can help further stabilize the α- concerning the δ-phase.[252] This

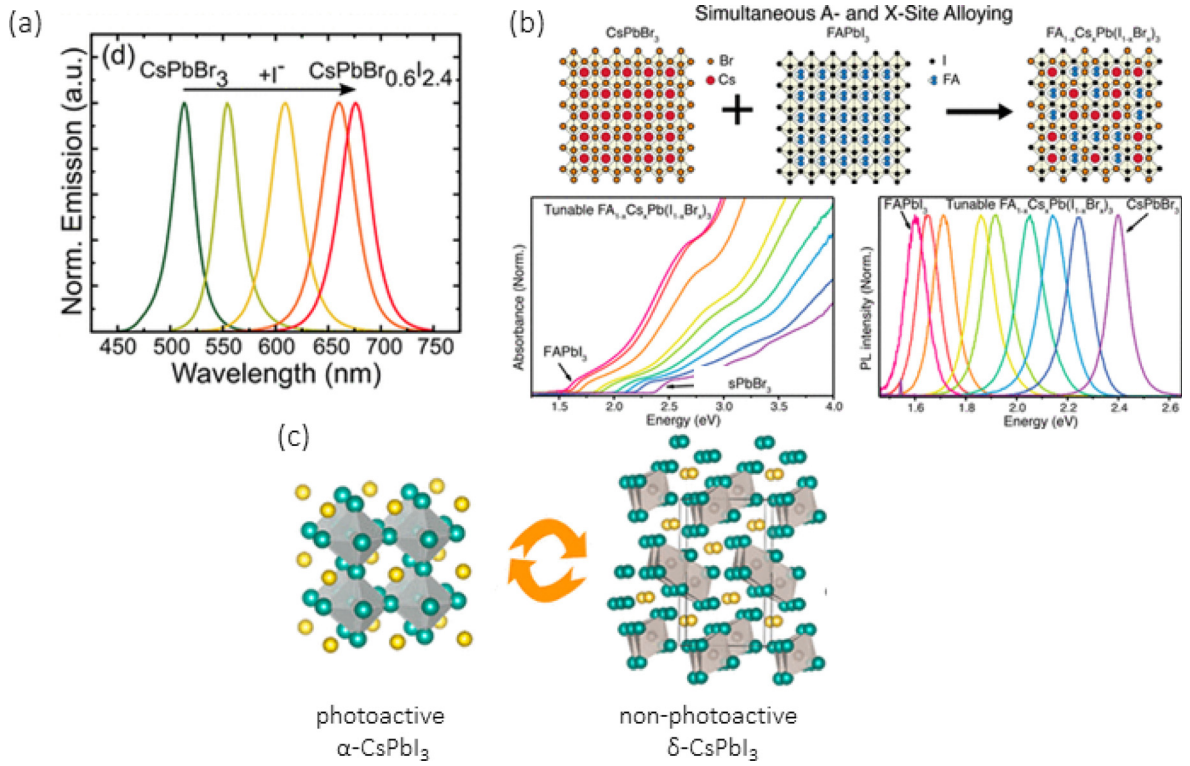

Fig. 13 (a) Variation of the PNC bandgap by alloying Br^- and I^- X-site,[253] and (b) by alloying concomitantly Br^- and I^- in the X-site and FA^+ and Cs^+ in the A-site.[254] (c) Spontaneous conversion of the photoactive to the non-photoactive phase of $CsPbI_3$.[269] (a) Reproduced with permission from ref. 253. Copyright 2018 American Chemical Society. (b) Reproduced with permission from ref. 254. Copyright 2019 American Chemical Society. (c) Reproduced with permission from ref. 269. Copyright 2019 American Chemical Society.

improved stability is attributed to the high surface/volume ratio, which increases the contribution of the surface energy to the total Gibbs-free energy of the material.[268] Since the surface is passivated in the NC, improved phase stability is expected compared to the bulk material.

5.3 Impacts of the size and size dispersivity on solar cell efficiency

One of the main challenges for applying PNCs to solar cells is size dispersivity. Since the bandgap is dependent on this parameter, the existence of NC with various sizes, inherent to the synthesis procedure, will introduce energetic disorder forming energy states near the band edges which can act as a trap for the charge carrier, compromising the charge separation and extraction in the device. In this sense, strategies to optimize the dispersivity of PNC are required. In **section 4.2** we discussed some strategies used to control the size dispersivity or separate the NCs based on their size, as is the case of GPC. Lim *et al.*[208] verified that, after GPC purification, the polydispersity of the PNC decreased from 0.067 to 0.031.[208] They further assembled solar cells comprised of FTO/TiO_2/PNCs/Spiro-OMeTAD/MoO_x/Ag, and observed that the efficiency of the device increased from 13.5% (high polydispersity) to 14.7% (low polydispersity), as a result of V_{OC}, J_{SC}, and FF improvements. This work demonstrates the importance of narrow size distribution to obtain efficient devices. However, we recognize that traditional GPC methodology is time-consuming and introduces an additional challenge to the fabrication of PNCs solar cells. Nevertheless, automated systems for GPC separation are available, in which the steps of column packing, solvent addition, and sample collection are automatic. This can help to save time and, therefore, the cost of the device preparation.

In **section 4.2** we also mentioned the growth of PNCs inside porous matrixes – an approach that used the porosity of material to physically restrict the growth. $MAPbI_3$ NC was grown in a porous SiO_2 matrix through the impregnation of a precursor solution in a thin film of SiO_2 NP of 30 nm average size.[212] This was further used as the active layer of a solar cell (FTO/TiO_2/PNC embedded in SiO_2 matrix/Spiro-OMeTAD/Au). The best efficiency was achieved when 45% of the SiO_2 pores were filled (NC size equals 10 nm), yielding V_{OC}, J_{SC}, FF, and PCE equal to 1.02 V, 16.42 mA cm^{-2}, 56.1%, and 9.3%, respectively, being stable for 5 h under illumination. It is important to note that using a porous template to grow the NCs can avoid the use of capping ligands, and save steps of purification and ligand exchange that are necessary for the proper operation of the conventional colloidal NC-based solar cells.

5.4 Exploring other solar cell architectures

To date, the number of reports with the inverted pin-type structure is considerably lesser compared to the regular nip-

type structure.[16,207] A plausible reason is that devices fabricated using the inverted architecture usually deliver lower efficiencies when compared to the nip devices with the same QD composition. The lower performance has been attributed to the solvation of the PTAA layer (employed as hole transport material) by the octane (a nonpolar solvent used in the deposition of the QD layer) and by the organic ligands used to stabilize the QD structure.[270] This compromises the electron-blocking ability of the PTAA and increases the bimolecular charge carrier recombination at the PTAA/QD interface.[270] Another factor that can explain the lower performance of the inverted configuration devices is the higher interfacial recombination at the interface between the perovskite and the electron transport material (in most cases, fullerenes derivatives).[271] The use of inorganic p-type semiconductors, such as NiO_x, can circumvent these issues and leads to a pin-type device with efficiency closer to the nip-type analog.

Some recent works demonstrated the fabrication of pin-type PNC solar cells. In 2019, Tavakoli *et al.*,[272] used the inverted architecture based on ITO/PTAA/$CsPbI_3$ NC/C_{60}/BCP/graphene (Fig. 14a) to prepare solar cells with 6.8% efficiency. This work showed the chemical vapor deposition of graphene to act as a transparent electrode, being a possible alternative to expensive metals such as silver and gold, commonly used as electrodes, and offering the possibility to fabricate all-transparent solar cells. In 2020, Shivarudraiah *et al.*,[207] used the device architecture FTO/NiO_x/$CsPbI_3$ NC/C_{60}/ZnO/Ag (Fig. 14b) and obtained efficiencies up to 13%. They used NiO_x as the HTM, which is, in principle, more stable than PTAA, and the electron transport layer was a combination of C_{60} and ZnO. The authors also introduced a ligand exchange step using FAI in MeOAc, instead of $Pb(NO_3)_2$/MeOAc, which they found to benefit the NC-NC electronic coupling and cause surface passivation. Recently, Mahato *et al.*[218] verified that adding 5% of DMSO into PEDOT:PSS HTM can increase the contact potential difference (CPD) of the PNC film, benefiting the hole extraction. The effect of DMSO-doping of PEDOT:PSS layer on the solar cell was verified by assembling an inverted device with the architecture: ITO/PEDOT:PSS/$CsPbI_3$ NC/C_{60}/BCP/Al. By increasing the amount of DMSO from 2.5 to 5%, V_{OC} improves from 0.908 to 0.978 V, and the PCE goes from 7.02 to 10.2%, respectively. The author attributed this improvement to the better interchain coupling between PEDOT units and better π–π stacking of PSS, which improves film conductivity.[273]

6. Progress and challenges for scaling up

Considering the synthesis methods mentioned in **section 3**, it is still challenging to obtain perovskite nanocrystals in a facile, reproducible, and scalable process. In addition, it is technically difficult to be sure that the fabrication process of the device would not decompose the nanocrystals or cause defective surfaces.[274] Moreover, for the scaling up of PNC solar cell technology, it must be considered the manufacturing cost, and the toxicity of polar solvents.[274] An approach to evaluate the cost impact of synthesis yield, economies-of-scale (EoS), solvent recycling, and automation for scaling up PNCs for optoelectronic applications has been presented by Kirmani *et al.*[275] The techno-economic model investigated by the authors denotes a cost decrease of more than 50% in a PNC

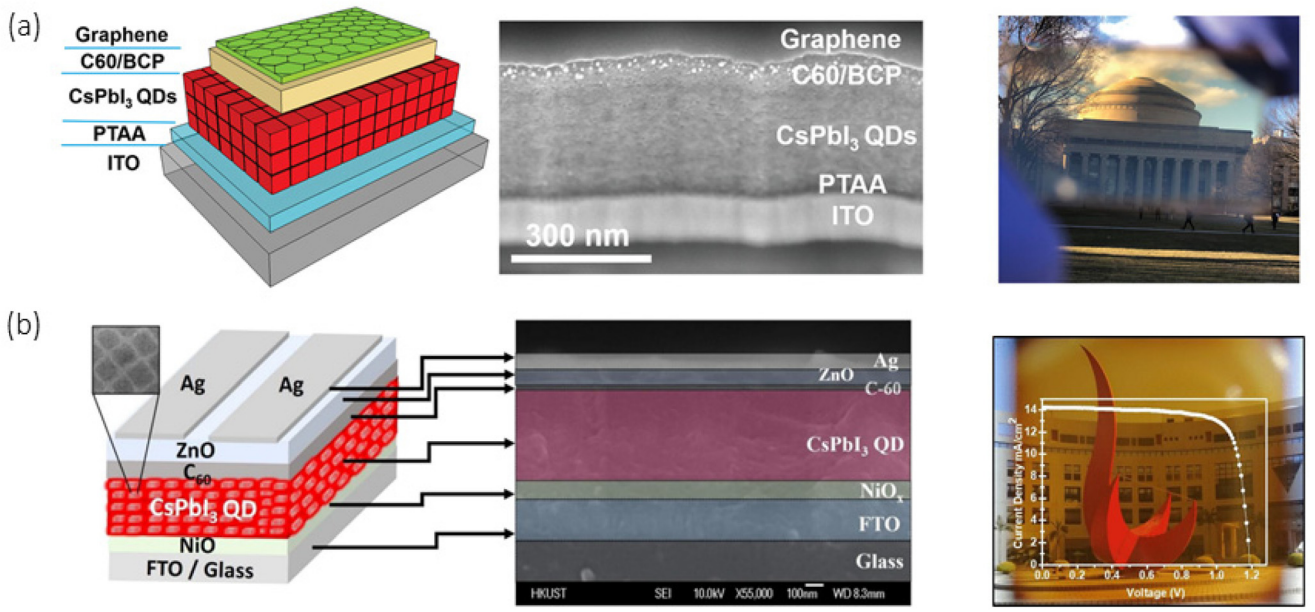

Fig. 14 Schematic diagram, cross-section scanning electron microscopy, and photography of the correspondent inverted pin-type PNC solar cells fabricated by (a) Tavakoli *et al.*, in 2019,[272] and (b) Shivarudraiah *et al.*, in 2020.[207] (a) Reproduced with permission from ref. 272. Copyright 2019 Wiley-VCH. (b) Reproduced with permission from ref. 207. Copyright 2020 American Chemical Society.

film area of 10^7 m^2 when the synthesis yield reaches 50%, instead of 12% from the current hot-injection synthesis protocol for $CsPbI_3$ QDs.[2] This is impressive and emphasizes how PNC synthesis is a key aspect of the upscaling of PNC solar cells. When EoS and solvent recycling are added up, costs drop by more than one-third.[275] It reinforces how the optimization of synthesis protocol and solvent reuse can affect NC solar cell upscaling. Also, developing a flow synthesis process is essential for the industrial scale-up of optoelectronic-grade PNC, avoiding batch-to-batch variations, and establishing a roll-to-roll coating system for large-area deposition of perovskite solar modules (PSM).[275]

While different deposition methods, including evaporation, have already been applied to produce perovskite layers in bulk PSC, only solution-based methods are compatible with PNC solar cells. These methods include spin coating, blade coating, slot-die coating, bar coating, spray coating, inkjet printing, and screen printing. Nevertheless, spin coating is not the ideal method for PSC scaling up because of its incompatibility with roll-to-roll systems. Blade coating, slot-die coating, bar coating, and screen printing are suitable for PNC deposition and they can be described as a tool that spreads the solution onto the substrate while removing the excess. All these methods were already explored in bulk-perovskite-based PSM,[16] however, other PSM techniques like spray coating and inkjet printing, drive a better prospectus to be extended to PNC solar cells.

6.1 Timeline of perovskite nanocrystal modules

As confirmed in the previous section, we can find plenty of works related to PNC solar cells. However, when the search is refined to "large-area", the results obtained are hugely reduced, in which a few articles are reviews that only report bulk-based PSC large-area.[19,20] A great portion of the results are related to LED devices.[31,276–278] At the same time, solar cells based on perovskite nanocrystals are restricted to lab cells (<1.0 cm^2), even when the authors mention a method compatible with large-area devices, *e.g.* scalable synthesis and film deposition methods. Besides, most of the presented processes are compatible with spray-coating deposition techniques, flexible substrates, *etc.*, and a scalable prototype with PNC as an active layer has not been shown yet.[18,25,279]

The upscaling of photovoltaic devices based on perovskite materials is relatively new looking back in the timeline of perovskite technology, as demonstrated in Fig. 15. Large area (>1 cm^2) bulk-perovskite-based cells were first fabricated in 2015,[16] the same year that first monodisperse PNC was prepared by Protesescu *et al.*[2] Only one year later, a PNC solar cell was reported by Swarnkar *et al.*,[26] while PSM has been already reported in the literature for bulk PSC.[16] Since then, PNC in large-area devices was only reported using PNC as an interlayer for bulk-based PSM to improve photovoltaic (PV) parameters, but not as a light-harvesting layer.[17,23] To our knowledge, PNC solar cells have only been fabricated in small areas as lab cells and probed some techniques that might be compatible with large-area deposition.[18] However, it is interesting to note that advances in fabrication processes from bulk PSC and quantum dot solar cells (QDSC), especially with PbS and PbSe QD, are expected to benefit the upscaling of PNC solar cells.

6.2 Large-area perovskite nanocrystal modules

The energy produced by a single cell might be insufficient for many practical applications. To increase the produced energy in photovoltaic devices, two options are available: (i) increasing the active area of the single cell or, more conventional, (ii) connecting single cells, in which each one is treated as a pixel. These pixels could be connected either in series or parallel. Series connection is the most frequently used for PSM structure for bulk PSC. Such configuration increases the voltage of modules by series-connecting small cells, summing the voltages produced by each one while retaining photocurrent in every single pixel. Parallel connection modules are more appropriate for tandem solar cells in which photocurrent must match between individual cells and add them up while maintaining voltage.[16]

Although PNC has not been applied over a large area as an active layer, it has been successfully applied as an interlayer between the bulk-based perovskite film and the HTM, as introduced before. Large-area devices in a nip-type architecture have been demonstrated by Cheng *et al.*[17] and Mali *et al.*,[23] showing that PNC plays a significant role in the surface passivation of bulk perovskite films.[280–283] Cheng *et al.*[17] reported a PSM with (6 × 6) cm^2 dimensions comprised of eight separated cells with an active area of 18.0 cm^2 (Fig. 16a, b, and c). They used spin-coated perovskite QDs as interlayers in the

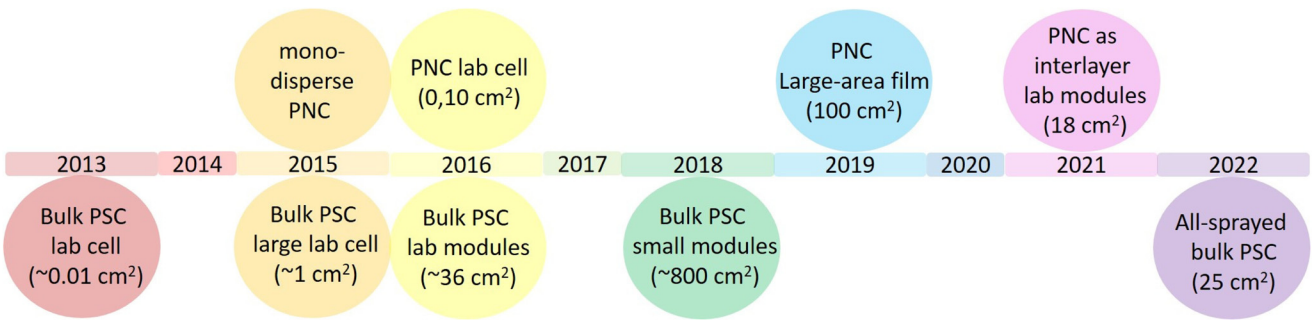

Fig. 15 Timeline of main developments in perovskite technology for PSC upscaling.

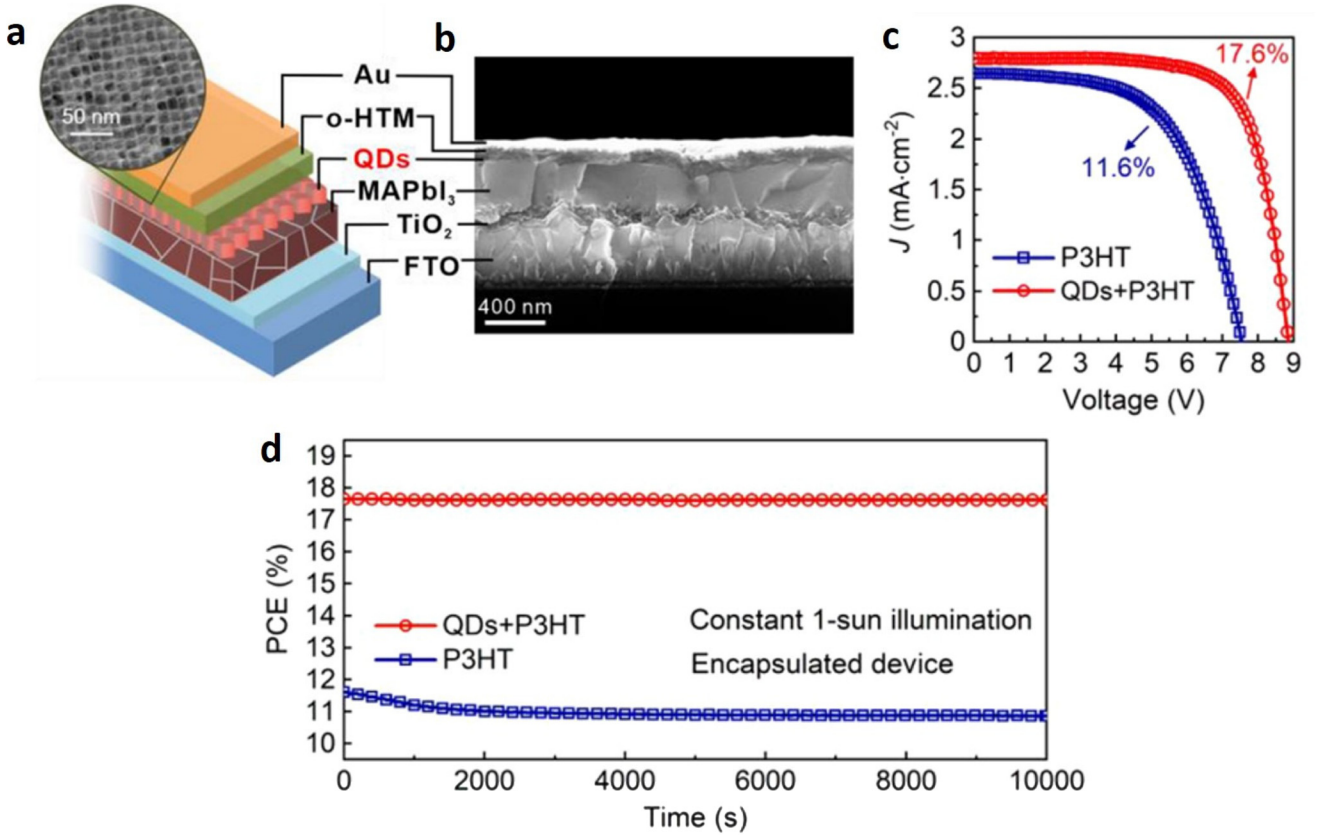

Fig. 16 (a) Schematic device architecture and (b) the cross-section SEM images of P3HT-based PSC with PNC interlayer. (c) *J*–*V* curve showing the PCE of dopant-free P3HT-based PSMs with and without a PNC interlayer at an active area of 18.0 cm^2. (d) Stable output measurement at maximum power point under constant 1-sun illumination for the P3HT-based PSMs with and without a PNC interlayer.[17] (a–d) Reproduced with permission from ref. 17. Copyright 2020 American Chemical Society.

device architecture FTO/c-TiO_2/mp-TiO_2/$MAPbI_3$/PNC/*o*-HTM/Au (*o*-HTM is P3HT, PTAA or Spiro-OMeTAD). The device was encapsulated and stored for 24 h to improve the sealing effect. Different PNC compositions were optimized firstly in small devices, including $CsPbI_2Br$, $CsPbI_{1.85}Br_{1.15}$, $CsPbI_{1.5}Br_{1.5}$, $CsPbI_{1.15}Br_{1.85}$, and $CsPbIBr_2$, with a maximum PCE of 21.1% obtained with $CsPbI_{1.85}Br_{1.15}$ NC as an interlayer between bulk-$MAPbI_3$ film and dopant-free-P3HT.[17] All PNCs capped by OLA and OA in octane solution were synthesized according to the one-pot hot-injection method in α-phase, uniform in size, nearly cubic shape, and demonstrated stability in ambient air with 30–40% relative humidity, maintaining 46.1% of PLQY after five months. Using the optimized conditions obtained for the small-area devices (0.12 cm^2), an 18.0 cm^2 lab module connected in series with the architecture FTO/c-TiO_2/mp-TiO_2/$MAPbI_3$/$CsPbI_{1.85}Br_{1.15}$/P3HT/Au was constructed, yielding an efficiency of 17.6% using P3HT as *o*-HTM (Fig. 16c). It is worth mentioning that P3HT is preferable in front of Spiro-OMeTAD and PTAA, because of its lower cost and improved oxygen and moisture stability.

PNCs were able to passivate the bulk-perovskite surface, promoting hole extraction from $MAPbI_3$ to HTM by forming a cascade of the energy levels (valence band alignment) and regulating polymer/molecule orientation for improved hole mobility without dopants in the HTM layer. This successful outcome of the PNCs multifunctional interlayer was probed by atomic force microscopy (AFM) images and grazing incidence X-ray diffraction (GIXRD).[17] It was found that the P3HT film deposited onto the perovskite/QD layer has a smooth morphology, a decreased pinhole density, and improved crystallinity. This translates into a boosted efficiency and stability for more than 10 000 h under constant 1-sun illumination (Fig. 16d). As a matter of comparison, the module without the surface treatment with PNC showed an initial PCE equal to 11.6%, with an expressive efficiency drop in the first 2000 h over 1-sun illumination. The presence of PNC is believed to reduce tail and trap states, promoting an increase of V_{OC} and FF, leading to an enhancement of more than 50% in PCE. Compared with single cells (active area = 0.12 cm^2), PSM has preserved more than 80% of PCE. By changing P3HT to PTAA and Spiro-OMeTAD, PCE of 15.9 and 16.0% was obtained in the modules, respectively. Also, the modules with PTAA and Spiro-OMeTAD maintained 80% of PCE when compared to small area devices (0.12 cm^2).[17]

In another work, Mali *et al.*[23] used a similar strategy with $CsPb_{0.95}Tb_{0.05}I_2Br$ QDs to stabilize the bulk and surface of

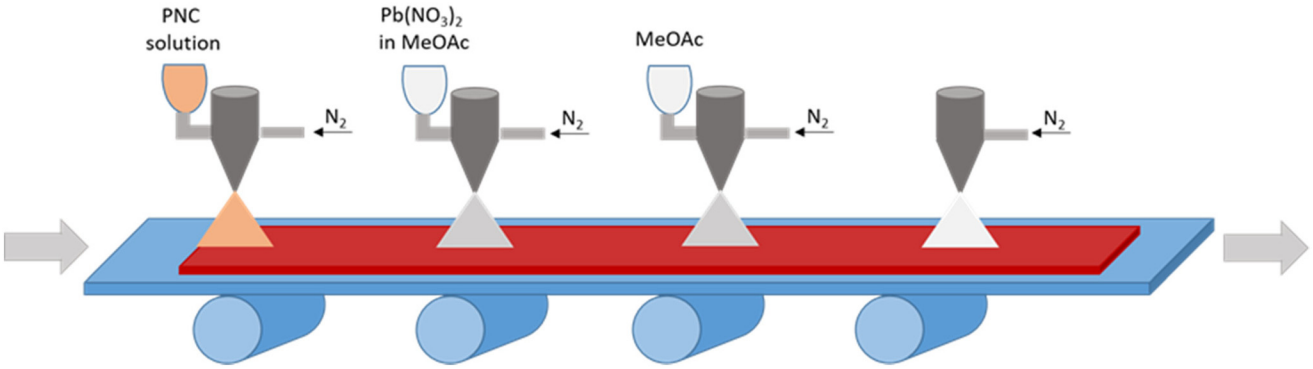

Fig. 17 Process of an automated spray-coating deposition developed by Yuan *et al.*[21] Adapted with permission from ref. 21. Copyright 2019 Wiley-VCH.

$CsPbI_2Br$ film. In the bulk passivation, PNC was spin-coated onto the as-deposited $CsPbI_2Br$ film before thermal annealing, causing the mixing between the PNC and the γ-$CsPbI_2Br$ phase during its formation. Then, a surface treatment with $CsPb_{0.95}Tb_{0.05}I_2Br$ QDs was realized by spin-coating a solution of this material onto the $CsPbI_2Br$-$CsPb_{0.95}Tb_{0.05}I_2Br$ film after the annealing. Subsequently, this film was quickly dipped in ethyl acetate. Un-encapsulated PSM with the architecture FTO/c-TiO_2/mp-TiO_2/$CsPbI_2Br$ + $CsPb_{0.95}Tb_{0.05}I_2Br$/$CsPb_{0.95}Tb_{0.05}I_2Br$/P3HT/Au and an active area of 19.80 cm^2 was constructed with series connection, reaching a PCE of 10.94%. Moreover, 80% of its initial efficiency was kept over a 30 days stability test (720 h) under continuous illumination (100 mW cm^{-2}) in the open atmosphere. The improved performance is because the PNC with Tb^{3+} is able to improve charge carrier lifetime and mobility under ambient conditions. Density functional theory (DFT) calculations suggested that Tb^{3+} doping benefits $CsPbI_2Br$ stability by lowering the binding energy. Also, the Tb d-orbital contributes to the conduction band edge of the material, shifting the Fermi level closer to the CB and introducing donor states at the bottom of the CB.[23] It corroborates the assumption that PNCs as an interlayer are able to improve charge mobility either through cascade energy levels[17] or by tuning the Fermi level.[23]

Spray-coated technology has been shown as an important deposition method for large areas in PSC. Yuan *et al.*[21] reported the spray-coated deposition of monodisperse $CsPbI_3$ PNC films (average size of 10 nm, synthesized by the conventional hot-injection method). The long-chain ligands from synthesis were partially removed using phenyltrimethylammonium bromide (PTABr) previously. The ligand exchange reaction was conducted by adding PTABr powder to the PNC in the hexane solution under stirring, then the residual PTABr was removed by centrifugation. The authors demonstrated an automated spray-coating process in the air (Fig. 17) where two nitrogen pipelines are responsible for atomizing and spraying PNC dispersed in octane, respectively. A uniform and pinhole-free PNC film on a (10 × 10) cm^2 substrate was obtained and the homogeneity was confirmed by overlapping UV-vis absorption spectra obtained for different regions of the film. The authors presented a proof-of-concept that spray-coating can cover large areas with a PNC solution, removing insulating ligands, passivating defects using $Pb(NO_3)_2$ in methyl acetate solution, and aiding in solvent drying of QD films.[21]

An extension of the automated spray-coating process to an all-sprayed process, in which all the layers are deposited from spray-based techniques, is expected to speed up PSM to industrial scale-up. A proposal that addresses this approach has been idealized in modules for bulk-based PSC, as proposed by Lee *et al.*;[22] this technology can be transplanted to PNC solar cells. The authors demonstrated a PCE of 10.08% for an all-sprayed PSM with the architecture FTO/c-TiO_2/$CsPbI_2Br$/MoO_2-PTAA/Carbon black, and an active area of 25 cm^2 (the small-area cells, with 0.12 cm^2, showed PCE of 14.25%). Spray-coating technology as much as inkjet printing seems to be a very interesting way to scale up PNC solar cells.

7. Conclusions and outlook

Much progress has been made in terms of synthesis and the fundamental understanding of the reaction and degradation mechanisms of PNCs. These outcomes helped to increase the efficiency of PNC solar cells. However, it is important to highlight that most of the reports in the literature are based on $CsPbI_3$ or $CsPbBr_3$ NC, probably because of the well-established synthesis protocol for these materials, their appropriate bandgap for solar cells, stability, and the possibility to obtain stable and optically active phases that are challenging to stabilize in their bulk analogs. Since one of the advantages of the PNC is the composition tunability, there is still room for exploring other materials, which is interesting for the fabrication of colored solar cells or active layers comprising of a heterojunction of materials with different bandgaps. In addition, the nip-type architecture has been the most used in PNC solar cells with remarkable PCE. Nevertheless, pin devices can also deliver comparable efficiencies. To reach this goal, the understanding of band alignment between the different materials

that comprise the device, and the working mechanism of the charge transfer from the PNC to the charge extraction layers is key to the advance of pin-type PNC solar cells. The elucidation of this mechanism can be useful not just for solar cells based on PNC, but also for other quantum dots materials such as CdTe, CdS, PbS and $AgBiS_2$.

Additionally, reports about the long-term stability of PNC solar cells are scarce, and very little is known about the intrinsic mechanism that leads to device degradation, which includes not only the PNC but also the other device's layers. This degradation can be triggered by both external and internal factors. As external we can mention moisture, oxygen, and light exposure. As intrinsic, the loss of capping ligands, aggregation, and phase conversion plays an important role. Despite knowing what causes the PNC solar cell degradation, we do not know how the device interfaces behave in front of these extrinsic and intrinsic factors. Knowing about the interface dynamics may allow the discovery of methods to retard or prevent the efficiency loss of the device. Further, there is no consensus about a standard protocol for evaluating the degradation of PNC solar cells, as we have for organic[284] and bulk-based perovskite solar cells.[285] The existence of a standard protocol can facilitate the literature data analysis, providing a way to compare how different approaches can impact the shelf life of the PNC solar cell. Along with it, it is imperative to probe the power conversion efficiency of the device over time by tracking the maximum power point, allowing identify the stabilized efficiency of the device.

Furthermore, there is room for improvement in the device's performance and fabrication process. Using short-chain organic molecules during the ligand exchange step endowed by different functional groups seems to be an alternative to improve efficiency. In this context, the design of new molecules plays an important role. By identifying the type of defect present on the NC surface, by means of DFT, for instance, and using Lewis acid–base chemistry it is possible to design and synthesize appropriate passivating molecules. This approach has been used for bulk-based perovskite solar cells, demonstrating meaningful results.[286–288]

In addition, new strategies for PNC solar cell assembly are necessary. Firstly, it is urgent to find substitutes for the commonly used HTM for nip-type devices: Spiro-OMeTAD and PTAA. The cost of these materials is very high, and not compatible with industrial manufacturing. In addition, Spiro-OMeTAD requires dopants agents (*e.g. tert*-butylpyridine and lithium bis(trifluoromethanesulfonyl)imide) to be properly oxidized and perform well as an HTM. However, these dopants can accelerate the degradation due to their hydrophobic nature, and compromise the long-term stability of the device. Replacing those HTMs with cheaper ones, such as P3HT and polyaniline, is necessary for the manufacturing viability of any perovskite-based technology. However, P3HT and polyaniline and their derivatives have been less applied in PNC-based solar cells. Furthermore, thinking about scalability, the complexity introduced by the deposition of subsequent PNC layers and the ligand exchange reaction, can enhance the fabrication cost when compared to bulk-based perovskite solar cells, in which no ligand-exchange process is required. As discussed, *in situ* methods to grow the NCs directly into the conductive substrate can be an alternative, but this approach is in a very early development stage. Moreover, production costs have been cited as a challenging step in the industrialization of this technology. In this sense, research focusing on improving the synthesis yield, solvent recycling, and the use of environmentally friendly and less expansive reactants[225] are encouraged to push forward the upscaling of PNC solar cells. Cost studies related to higher production volumes are believed to be more cost-effective, but the impact of lower-grade solvents and precursors is expected to help the attractiveness of this technology. Furthermore, efforts are needed in the development of lead-free PNCs-based solar cells. Recent advances are obtained for the replacement of lead with tin, germanium, bismuth, and antimony; however, the efficiency is far behind the Pb-based-PNC solar cells.[289] Beyond PNC, other lead-free materials have been investigated, for instance, silver bismuth sulfide ($AgBiS_2$) demonstrating a record efficiency of 9.17%.[290]

As can be seen in this Review, there is a long way toward the commercialization of PNC solar cells, and several questions about the fundamental properties of the material and the device are still open. We hope that the discussions brought here encourage the community to find suitable solutions for the up-scaling of PNC-based solar cells.

Author contributions

L. Scalon: Conceptualization, investigation, writing original draft, review, and editing. F. S. Freitas: Writing and review. F. C. Marques: Conceptualization, review, editing, and supervision. A. F. Nogueira: Conceptualization, review, supervision, and funding acquisition.

Conflicts of interest

The authors declare no competing interests.

Acknowledgements

The authors gratefully acknowledge support from FAPESP (São Paulo Research Foundation, Grant Numbers 2017/11631-2 and 2018/21401-7), Shell, and the strategic importance of the support given by ANP (Brazil's National Oil, Natural Gas, and Biofuels Agency) through the R&D levy regulation. We also thank the National Council for Scientific and Technological Development (CNPq), the Coordination for the Improvement of Higher Education Personnel (Capes), and the Center for Innovation on New Energies (CINE). L. S. acknowledges FAPESP grant numbers 2020/04406-5, and 2021/12104-1. F. C. M. acknowledges CNPq grants numbers 435260/2018-9, 465423/2014-0 and 313703/2021-3.

References

1 A. Kojima, K. Teshima, Y. Shirai and T. Miyasaka, *J. Am. Chem. Soc.*, 2009, **131**, 6050–6051.
2 L. Protesescu, S. Yakunin, M. I. Bodnarchuk, F. Krieg, R. Caputo, C. H. Hendon, R. X. Yang, A. Walsh and M. V. Kovalenko, *Nano Lett.*, 2015, **15**, 3692–3696.
3 K. Gahlot, S. de Graaf, H. Duim, G. Nedelcu, R. M. Koushki, M. Ahmadi, D. Gavhane, A. Lasorsa, O. De Luca, P. Rudolf, P. C. A. van der Wel, M. A. Loi, B. J. Kooi, G. Portale, J. Calbo and L. Protesescu, *Adv. Mater.*, 2022, e2201353.
4 T. Liu, X. Zhao, P. Wang, Q. C. Burlingame, J. Hu, K. Roh, Z. Xu, B. P. Rand, M. Chen and Y. Loo, *Adv. Energy Mater.*, 2022, 2200402.
5 L. Dou, A. B. Wong, Y. Yu, M. Lai, N. Kornienko, S. W. Eaton, A. Fu, C. G. Bischak, J. Ma, T. Ding, N. S. Ginsberg, L.-W. Wang, A. P. Alivisatos and P. Yang, *Science*, 2015, **349**, 1518–1521.
6 H. Deng, D. Dong, K. Qiao, L. Bu, B. Li, D. Yang, H.-E. Wang, Y. Cheng, Z. Zhao, J. Tang and H. Song, *Nanoscale*, 2015, **7**, 4163–4170.
7 J. M. C. da Silva Filho and F. C. Marques, *MRS Adv.*, 2018, **3**, 1843–1848.
8 A. Jana, A. Meena, S. A. Patil, Y. Jo, S. Cho, Y. Park, V. G. Sree, H. Kim, H. Im and R. A. Taylor, *Prog. Mater. Sci.*, 2022, **129**, 100975.
9 S.-T. Ha, R. Su, J. Xing, Q. Zhang and Q. Xiong, *Chem. Sci.*, 2017, **8**, 2522–2536.
10 G. Ghosh, K. Marjit, S. Ghosh, D. Ghosh and A. Patra, *ChemNanoMat*, 2022, **8**, e202200172.
11 A. Liu, D. B. Almeida, L. G. Bonato, G. Nagamine, L. F. Zagonel, A. F. Nogueira, L. A. Padilha and S. T. Cundiff, *Sci. Adv.*, 2021, **7**, eabb3594.
12 E. Raza and Z. Ahmad, *Energy Rep.*, 2022, **8**, 5820–5851.
13 B. Huang, X. Xia, X. Wang and F. Li, *Sol. Energy Mater. Sol. Cells*, 2022, **240**, 111682.
14 H.-S. Kim, C.-R. Lee, J.-H. Im, K.-B. Lee, T. Moehl, A. Marchioro, S.-J. Moon, R. Humphry-Baker, J.-H. Yum, J. E. Moser, M. Grätzel and N.-G. Park, *Sci. Rep.*, 2012, **2**, 591.
15 H. Li, C. Zuo, D. Angmo, H. Weerasinghe, M. Gao and J. Yang, *Nano-Micro Lett.*, 2022, **14**, 79.
16 D. Li, D. Zhang, K. Lim, Y. Hu, Y. Rong, A. Mei, N. Park and H. Han, *Adv. Funct. Mater.*, 2021, **31**, 2008621.
17 F. Cheng, R. He, S. Nie, C. Zhang, J. Yin, J. Li, N. Zheng and B. Wu, *J. Am. Chem. Soc.*, 2021, **143**, 5855–5866.
18 Q. Zhao, R. Han, A. R. Marshall, S. Wang, B. M. Wieliczka, J. Ni, J. Zhang, J. Yuan, J. M. Luther, A. Hazarika and G.-R. Li, *Adv. Mater.*, 2022, **34**, e2107888.
19 E. Berger, M. Bagheri, S. Asgari, J. Zhou, M. Kokkonen, P. Talebi, J. Luo, A. F. Nogueira, T. Watson and S. G. Hashmi, *Sustainable Energy Fuels*, 2022, **6**, 2879–2900.
20 P. Liu, G. Tang and F. Yan, *Sol. RRL*, 2022, **6**, 2100683.
21 J. Yuan, C. Bi, S. Wang, R. Guo, T. Shen, L. Zhang and J. Tian, *Adv. Funct. Mater.*, 2019, **29**, 1906615.
22 D. S. Lee, M. J. Ki, H. J. Lee, J. K. Park, S. Y. Hong, B. W. Kim, J. H. Heo and S. H. Im, *ACS Appl. Mater. Interfaces*, 2022, **14**, 7926–7935.
23 S. S. Mali, J. V. Patil, S. R. Rondiya, N. Y. Dzade, J. A. Steele, M. K. Nazeeruddin, P. S. Patil and C. K. Hong, *Adv. Mater.*, 2022, **34**, e2203204.
24 H. Liu, C. Geng, P. Wei, H. Chen, S. Zheng, H. Wang and Y. Xie, *J. Alloys Compd.*, 2022, **912**, 165123.
25 J. A. Dias, S. H. Santagneli, S. J. L. Ribeiro and Y. Messaddeq, *Sol. RRL*, 2021, **5**, 2100205.
26 A. Swarnkar, A. R. Marshall, E. M. Sanehira, B. D. Chernomordik, D. T. Moore, J. A. Christians, T. Chakrabarti and J. M. Luther, *Science*, 2016, **354**, 92–95.
27 The National Renewable Energy Lavoratory, Best Research-Cell Efficiency Chart, **https://www.nrel.gov/pv/cell-efficiency.html**.
28 J. Chen, D. Jia, R. Zhuang, Y. Hua and X. Zhang, *Adv. Mater.*, 2022, e2204259.
29 J. M. C. da Silva Filho, A. D. Gonçalves, F. C. Marques and J. N. de Freitas, *Sol. RRL*, 2021, 2100865.
30 R. L. Z. Hoye, P. Schulz, L. T. Schelhas, A. M. Holder, K. H. Stone, J. D. Perkins, D. Vigil-Fowler, S. Siol, D. O. Scanlon, A. Zakutayev, A. Walsh, I. C. Smith, B. C. Melot, R. C. Kurchin, Y. Wang, J. Shi, F. C. Marques, J. J. Berry, W. Tumas, S. Lany and T. Buonassisi, *Chem. Mater.*, 2017, **29**, 1964–1988.
31 Y.-H. Kim, J. Park, S. Kim, J. S. Kim, H. Xu, S.-H. Jeong, B. Hu and T.-W. Lee, *Nat. Nanotechnol.*, 2022, **17**, 590–597.
32 K. Wang and L. Dou, *Nat. Nanotechnol.*, 2022, **17**, 562–563.
33 X. Shen, H. Wu, X. Zhang, M. Xu, J. Hu, J. Zhu, B. Dong, W. W. Yu and X. Bai, *J. Phys. Chem. Lett.*, 2021, **12**, 94–100.
34 H. Wang, X. Gong, D. Zhao, Y.-B. Zhao, S. Wang, J. Zhang, L. Kong, B. Wei, R. Quintero-Bermudez, O. Voznyy, Y. Shang, Z. Ning, Y. Yan, E. H. Sargent and X. Yang, *Joule*, 2020, **4**, 1977–1987.
35 S. A. Kulkarni, T. Baikie, P. P. Boix, N. Yantara, N. Mathews and S. Mhaisalkar, *J. Mater. Chem. A*, 2014, **2**, 9221–9225.
36 D. Chi, S. Huang, M. Zhang, S. Mu, Y. Zhao, Y. Chen and J. You, *Adv. Funct. Mater.*, 2018, **28**, 1804603.
37 W. Ke, I. Spanopoulos, Q. Tu, I. Hadar, X. Li, G. S. Shekhawat, V. P. Dravid and M. G. Kanatzidis, *J. Am. Chem. Soc.*, 2019, **141**, 8627–8637.
38 H. A. Schwartz, H. Laurenzen, A. Marzouk, M. Runkel, K. O. Brinkmann, D. Rogalla, T. Riedl, S. Ashhab and S. Olthof, *ACS Appl. Mater. Interfaces*, 2021, **13**, 4203–4210.
39 T. Kodalle, R. F. Moral, L. Scalon, R. Szostak, M. Abdelsamie, P. E. Marchezi, A. F. Nogueira and C. M. Sutter-Fella, *Adv. Energy Mater.*, 2022, 2201490.
40 P. E. Marchezi, E. M. Therézio, R. Szostak, H. C. Loureiro, K. Bruening, A. Gold-Parker, M. A. Melo, C. J. Tassone, H. C. N. Tolentino, M. F. Toney and A. F. Nogueira, *J. Mater. Chem. A*, 2020, **8**, 9302–9312.
41 H. Shi and M.-H. Du, *Phys. Rev. Appl.*, 2015, **3**, 054005.
42 D. Sumanth Kumar, B. Jai Kumar and H. M. Mahesh, *Synthesis of Inorganic Nanomaterials: Advances and Key Technologies*, Elsevier, 2018, pp. 59–88.

43 F. W. Wise, *Acc. Chem. Res.*, 2000, **33**, 773–780.
44 A. De, N. Mondal and A. Samanta, *J. Phys. Chem. C*, 2018, **122**(25), 13617–13623.
45 W. Zheng, P. Huang, Z. Gong, D. Tu, J. Xu, Q. Zou, R. Li, W. You, J.-C. G. Bünzli and X. Chen, *Nat. Commun.*, 2018, **9**, 3462.
46 A. M. Fox, *Contemp. Phys.*, 1996, **37**, 111–125.
47 S. Baskoutas and A. F. Terzis, *J. Appl. Phys.*, 2006, **99**, 013708.
48 J. Butkus, P. Vashishtha, K. Chen, J. K. Gallaher, S. K. K. Prasad, D. Z. Metin, G. Laufersky, N. Gaston, J. E. Halpert and J. M. Hodgkiss, *Chem. Mater.*, 2017, **29**, 3644–3652.
49 G. Schmid, *Nanotechnology: Volume 1: Principles and Fundamentals (Nanotechnology (VCH))*, Wiley-VCH, Weinheim, 1st edn, 2008.
50 E. Hanamura, *Opt. Quantum Electron.*, 1989, **21**, 441–450.
51 J. Li and J.-J. Zhu, *Analyst*, 2013, **138**, 2506–2515.
52 J. A. Sichert, Y. Tong, N. Mutz, M. Vollmer, S. Fischer, K. Z. Milowska, R. García Cortadella, B. Nickel, C. Cardenas-Daw, J. K. Stolarczyk, A. S. Urban and J. Feldmann, *Nano Lett.*, 2015, **15**, 6521–6527.
53 C. Giansante and I. Infante, *J. Phys. Chem. Lett.*, 2017, **8**, 5209–5215.
54 L. Wu, Q. Zhong, D. Yang, M. Chen, H. Hu, Q. Pan, H. Liu, M. Cao, Y. Xu, B. Sun and Q. Zhang, *Langmuir*, 2017, **33**, 12689–12696.
55 Y. Yao, H. Yu, Y. Wu, Y. Lu, Z. Liu, X. Xu, B. Ma, Q. Zhang, S. Chen and W. Huang, *ACS Omega*, 2019, **4**, 9150–9159.
56 Y. Liu, D. Li, L. Zhang, Y. Chen, C. Geng, S. Shi, Z. Zhang, W. Bi and S. Xu, *Chem. Mater.*, 2020, **32**, 1904–1913.
57 B. Zhang, L. Goldoni, J. Zito, Z. Dang, G. Almeida, F. Zaccaria, J. de Wit, I. Infante, L. De Trizio and L. Manna, *Chem. Mater.*, 2019, **31**, 9140–9147.
58 B. Zhang, L. Goldoni, C. Lambruschini, L. Moni, M. Imran, A. Pianetti, V. Pinchetti, S. Brovelli, L. De Trizio and L. Manna, *Nano Lett.*, 2020, **20**, 8847–8853.
59 M. C. Brennan, J. Zinna and M. Kuno, *ACS Energy Lett.*, 2017, **2**, 1487–1488.
60 Y. Tang, D. Poonia, M. van der Laan, D. Timmerman, S. Kinge, L. D. A. Siebbeles and P. Schall, *ACS Appl. Energy Mater.*, 2022, **5**, 5415–5422.
61 F. Krieg, P. C. Sercel, M. Burian, H. Andrusiv, M. I. Bodnarchuk, T. Stöferle, R. F. Mahrt, D. Naumenko, H. Amenitsch, G. Rainò and M. V. Kovalenko, *ACS Cent. Sci.*, 2020, **7**(1), 135–144.
62 M. C. Brennan, A. Forde, M. Zhukovskyi, A. J. Baublis, Y. V. Morozov, S. Zhang, Z. Zhang, D. S. Kilin and M. Kuno, *J. Phys. Chem. Lett.*, 2020, **11**, 4937–4944.
63 M. C. Brennan, J. E. Herr, T. S. Nguyen-Beck, J. Zinna, S. Draguta, S. Rouvimov, J. Parkhill and M. Kuno, *J. Am. Chem. Soc.*, 2017, **139**, 12201–12208.
64 P. Della Sala, N. Buccheri, A. Sanzone, M. Sassi, P. Neri, C. Talotta, A. Rocco, V. Pinchetti, L. Beverina, S. Brovelli and C. Gaeta, *Chem. Commun.*, 2019, **55**, 3160–3163.
65 C. Li, W. Chen, D. Wu, D. Quan, Z. Zhou, J. Hao, J. Qin, Y. Li, Z. He and K. Wang, *Sci. Rep.*, 2015, **5**, 17777.
66 Q. Zhao, A. Hazarika, L. T. Schelhas, J. Liu, E. A. Gaulding, G. Li, M. Zhang, M. F. Toney, P. C. Sercel and J. M. Luther, *ACS Energy Lett.*, 2020, **5**, 238–247.
67 L. Liu, R. Zhao, C. Xiao, F. Zhang, F. Pevere, K. Shi, H. Huang, H. Zhong and I. Sychugov, *J. Phys. Chem. Lett.*, 2019, **10**, 5451–5457.
68 Q. Shang, A. L. Kaledin, Q. Li and T. Lian, *J. Chem. Phys.*, 2019, **151**, 074705.
69 H. Zhu, Y. Yang, K. Hyeon-Deuk, M. Califano, N. Song, Y. Wang, W. Zhang, O. V. Prezhdo and T. Lian, *Nano Lett.*, 2014, **14**, 1263–1269.
70 S. Meloni, G. Palermo, N. Ashari-Astani, M. Grätzel and U. Rothlisberger, *J. Mater. Chem. A*, 2016, **4**, 15997–16002.
71 F. Hao, C. C. Stoumpos, D. H. Cao, R. P. H. Chang and M. G. Kanatzidis, *Nat. Photonics*, 2014, **8**, 489–494.
72 N. Mondal and A. Samanta, *Nanoscale*, 2017, **9**, 1878–1885.
73 A. Haque, V. K. Ravi, G. S. Shanker, I. Sarkar, A. Nag and P. K. Santra, *J. Phys. Chem. C*, 2017, **122**(25), 13399–13406.
74 I. Karimata and T. Tachikawa, *Angew. Chem., Int. Ed.*, 2021, **60**, 2548–2553.
75 B. T. Diroll, G. Nedelcu, M. V. Kovalenko and R. D. Schaller, *Adv. Funct. Mater.*, 2017, **27**, 1606750.
76 A. Liu, L. G. Bonato, F. Sessa, D. B. Almeida, E. Isele, G. Nagamine, L. F. Zagonel, A. F. Nogueira, L. A. Padilha and S. T. Cundiff, *J. Chem. Phys.*, 2019, **151**, 191103.
77 T. Debnath, D. Sarker, H. Huang, Z.-K. Han, A. Dey, L. Polavarapu, S. V. Levchenko and J. Feldmann, *Nat. Commun.*, 2021, **12**, 2629.
78 P. Ijaz, M. Imran, M. M. Soares, H. C. N. Tolentino, B. Martín-García, C. Giannini, I. Moreels, L. Manna and R. Krahne, *J. Phys. Chem. Lett.*, 2020, **11**, 2079–2085.
79 L. Chen, B. Li, C. Zhang, X. Huang, X. Wang and M. Xiao, *Nano Lett.*, 2018, **18**, 2074–2080.
80 T. Mueller and E. Malic, *npj 2D Mater. Appl.*, 2018, **2**, 29.
81 M. Liu, H. Zhang, D. Gedamu, P. Fourmont, H. Rekola, A. Hiltunen, S. G. Cloutier, R. Nechache, A. Priimagi and P. Vivo, *Small*, 2019, **15**, e1900801.
82 S. ten Brinck, F. Zaccaria and I. Infante, *ACS Energy Lett.*, 2019, **4**, 2739–2747.
83 D. Meggiolaro, E. Mosconi and F. De Angelis, *ACS Energy Lett.*, 2018, **3**, 447–451.
84 T. Leijtens, G. E. Eperon, A. J. Barker, G. Grancini, W. Zhang, J. M. Ball, A. R. S. Kandada, H. J. Snaith and A. Petrozza, *Energy Environ. Sci.*, 2016, **9**, 3472–3481.
85 Q. A. Akkerman, V. D'Innocenzo, S. Accornero, A. Scarpellini, A. Petrozza, M. Prato and L. Manna, *J. Am. Chem. Soc.*, 2015, **137**, 10276–10281.
86 W. van der Stam, J. J. Geuchies, T. Altantzis, K. H. W. van den Bos, J. D. Meeldijk, S. Van Aert, S. Bals, D. Vanmaekelbergh and C. de Mello Donega, *J. Am. Chem. Soc.*, 2017, **139**, 4087–4097.
87 I. du Fossé, J. T. Mulder, G. Almeida, A. G. M. Spruit, I. Infante, F. C. Grozema and A. J. Houtepen, *J. Am. Chem. Soc.*, 2022, **144**, 11059–11063.

88 D. Yang, X. Li and H. Zeng, *Adv. Mater. Interfaces*, 2018, **5**, 1701662.
89 Q. A. Akkerman, G. Rainò, M. V. Kovalenko and L. Manna, *Nat. Mater.*, 2018, **17**, 394–405.
90 Y. Dong, Y. Zhao, S. Zhang, Y. Dai, L. Liu, Y. Li and Q. Chen, *J. Mater. Chem. A*, 2018, **6**, 21729–21746.
91 X. Li, M. I. Dar, C. Yi, J. Luo, M. Tschumi, S. M. Zakeeruddin, M. K. Nazeeruddin, H. Han and M. Grätzel, *Nat. Chem.*, 2015, **7**, 703–711.
92 D. Liu, K. Weng, S. Lu, F. Li, H. Abudukeremu, L. Zhang, Y. Yang, J. Hou, H. Qiu, Z. Fu, X. Luo, L. Duan, Y. Zhang, H. Zhang and J. Li, *Sci. Adv.*, 2022, **8**, eabm8433.
93 X. Jin, K. Ma and H. Gao, *J. Am. Chem. Soc.*, 2022, **144**(44), 20411–20420.
94 F. Palazon, Q. A. Akkerman, M. Prato and L. Manna, *ACS Nano*, 2016, **10**, 1224–1230.
95 J. Ko, K. Ma, J. F. Joung, S. Park and J. Bang, *Nano Lett.*, 2021, **21**, 2288–2295.
96 S. Shin, Y. Kim, N. Gwak, I. Jeong, M. Lee, K. Kang, S. Yeon, S. Kim, T. A. Kim and N. Oh, *Appl. Surf. Sci.*, 2023, **608**, 155016.
97 H. Huang, M. I. Bodnarchuk, S. V. Kershaw, M. V. Kovalenko and A. L. Rogach, *ACS Energy Lett.*, 2017, **2**, 2071–2083.
98 J. Shamsi, A. S. Urban, M. Imran, L. De Trizio and L. Manna, *Chem. Rev.*, 2019, **119**, 3296–3348.
99 J. Shi, Y. Li, Y. Li, D. Li, Y. Luo, H. Wu and Q. Meng, *Joule*, 2018, **2**, 879–901.
100 J. T. DuBose and P. V. Kamat, *Chem. Rev.*, 2022, **122**, 12475–12494.
101 L. Hou, P. Tamarat and B. Lounis, *Nanomaterials*, 2021, **11**, 1058.
102 R. Ahumada-Lazo, R. Saran, O. Woolland, Y. Jia, M.-E. Kyriazi, A. G. Kanaras, D. Binks and R. J. Curry, *J. Phys. Photonics*, 2021, **3**, 021002.
103 A. Forde, E. Hobbie and D. Kilin, *MRS Adv.*, 2019, **4**, 1981–1988.
104 N. Mondal, A. De and A. Samanta, *J. Phys. Chem. Lett.*, 2018, **9**, 3673–3679.
105 Q. Lin, A. Armin, P. L. Burn and P. Meredith, *Acc. Chem. Res.*, 2016, **49**, 545–553.
106 C. S. Ponseca, T. J. Savenije, M. Abdellah, K. Zheng, A. Yartsev, T. Pascher, T. Harlang, P. Chabera, T. Pullerits, A. Stepanov, J.-P. Wolf and V. Sundström, *J. Am. Chem. Soc.*, 2014, **136**, 5189–5192.
107 A. K. Jena, A. Kulkarni and T. Miyasaka, *Chem. Rev.*, 2019, **119**, 3036–3103.
108 A. T. Barrows, A. J. Pearson, C. K. Kwak, A. D. F. Dunbar, A. R. Buckley and D. G. Lidzey, *Energy Environ. Sci.*, 2014, **7**, 2944.
109 F. Mathies, H. Eggers, B. S. Richards, G. Hernandez-Sosa, U. Lemmer and U. W. Paetzold, *ACS Appl. Energy Mater.*, 2018, **1**, 1834–1839.
110 Z. Wei, H. Chen, K. Yan and S. Yang, *Angew. Chem.*, 2014, **126**, 13455–13459.
111 M.-C. Tang, Y. Fan, D. Barrit, X. Chang, H. X. Dang, R. Li, K. Wang, D.-M. Smilgies, S. (Frank) Liu, S. De Wolf, T. D. Anthopoulos, K. Zhao and A. Amassian, *J. Mater. Chem. A*, 2020, **8**, 1095–1104.
112 R. Wu, C. Wang, M. Jiang, C. Liu, D. Liu, S. Li, Q. Kong, W. He, C. Zhan, F. Zhang, X. Liu, B. Yang and W. Hu, *J. Renewable Sustainable Energy*, 2021, **13**, 012701.
113 M. Liu, M. B. Johnston and H. J. Snaith, *Nature*, 2013, **501**, 395–398.
114 N. F. V. Borrero, J. M. C. da Silva Filho, N. F. Coutinho, J. N. Freitas and F. C. Marques, *J. Inorg. Organomet. Polym.*, 2021, **32**, 1259–1265.
115 C. Borri, N. Calisi, E. Galvanetto, N. Falsini, F. Biccari, A. Vinattieri, G. Cucinotta and S. Caporali, *Nanomaterials*, 2020, **10**, 60.
116 J. M. C. da Silva Filho, V. A. Ermakov and F. C. Marques, *Sci. Rep.*, 2018, **8**, 1563.
117 J. M. C. da Silva Filho, N. F. V. Borrero, G. A. Viana, R. B. Merlo and F. C. Marques, *Cryst. Growth Des.*, 2020, **20**, 1531–1537.
118 J. M. C. da Silva Filho, R. Landers and F. C. Marques, *J. Inorg. Organomet. Polym. Mater.*, 2019, 1–7.
119 R. Patidar, D. Burkitt, K. Hooper, D. Richards and T. Watson, *Mater. Today Commun.*, 2020, **22**, 100808.
120 L. Qiu, S. He, Y. Jiang and Y. Qi, *J. Mater. Chem. A*, 2021, **9**, 22759–22780.
121 B. R. Sutherland, S. Hoogland, M. M. Adachi, P. Kanjanaboos, C. T. O. Wong, J. J. McDowell, J. Xu, O. Voznyy, Z. Ning, A. J. Houtepen and E. H. Sargent, *Adv. Mater.*, 2015, **27**, 53–58.
122 Y. Chen, S. Tan, N. Zhou, N. Yang, W. Zhou, Y. Wu, K. Weber, Q. Chen and H. Zhou, *Sol. RRL*, 2019, **3**, 1900083.
123 M. S. Holanda, R. F. Moral, P. E. Marchezi, F. C. Marques and A. F. Nogueira, *EcoMat*, 2021, **3**(4), e12124.
124 Y. Zhang, T. D. Siegler, C. J. Thomas, M. K. Abney, T. Shah, A. De Gorostiza, R. M. Greene and B. A. Korgel, *Chem. Mater.*, 2020, **32**, 5410–5423.
125 K. Hoshi, T. Chiba, J. Sato, Y. Hayashi, Y. Takahashi, H. Ebe, S. Ohisa and J. Kido, *ACS Appl. Mater. Interfaces*, 2018, **10**, 24607–24612.
126 A. A. M. Brown, P. Vashishtha, T. J. N. Hooper, Y. F. Ng, G. V. Nutan, Y. Fang, D. Giovanni, J. N. Tey, L. Jiang, B. Damodaran, T. C. Sum, S. H. Pu, S. G. Mhaisalkar and N. Mathews, *Chem. Mater.*, 2021, **33**, 2387–2397.
127 M. Han and Y.-Y. Noh, *Phys. Status Solidi A*, 2021, **218**, 2100366.
128 R. Grisorio, M. E. Di Clemente, E. Fanizza, I. Allegretta, D. Altamura, M. Striccoli, R. Terzano, C. Giannini, M. Irimia-Vladu and G. P. Suranna, *Nanoscale*, 2019, **11**, 986–999.
129 J. Tong, J. Wu, W. Shen, Y. Zhang, Y. Liu, T. Zhang, S. Nie and Z. Deng, *ACS Appl. Mater. Interfaces*, 2019, **11**, 9317–9325.
130 F. Ambroz, W. Xu, S. Gadipelli, D. J. L. Brett, C. Lin, C. Contini, M. A. McLachlan, J. R. Durrant, I. P. Parkin

and T. J. Macdonald, *Part. Part. Syst. Charact.*, 2020, **37**, 1900391.
131 A. Kirakosyan, Y. Kim, M. R. Sihn, M. Jeon, J. Jeong and J. Choi, *ChemNanoMat*, 2020, **6**, 1863–1869.
132 S. R. Pathipati, *J. Lumin.*, 2021, **239**, 118345.
133 F. Zhang, H. Zhong, C. Chen, X. Wu, X. Hu, H. Huang, J. Han, B. Zou and Y. Dong, *ACS Nano*, 2015, **9**, 4533–4542.
134 H. Huang, J. Raith, S. V. Kershaw, S. Kalytchuk, O. Tomanec, L. Jing, A. S. Susha, R. Zboril and A. L. Rogach, *Nat. Commun.*, 2017, **8**, 996.
135 A. Jancik Prochazkova, M. C. Scharber, C. Yumusak, J. Jančík, J. Másilko, O. Brüggemann, M. Weiter, N. S. Sariciftci, J. Krajcovic, Y. Salinas and A. Kovalenko, *Sci. Rep.*, 2020, **10**, 15720.
136 M. Chen, Y. Yuan, Z. Wang, X. Shen, Y. Liu and D. Cao, *Cryst. Growth Des.*, 2020, **20**, 4855–4860.
137 I. Levchuk, P. Herre, M. Brandl, A. Osvet, R. Hock, W. Peukert, P. Schweizer, E. Spiecker, M. Batentschuk and C. J. Brabec, *Chem. Commun.*, 2016, **53**, 244–247.
138 S. Zhou, *RSC Adv.*, 2021, **11**, 28410–28419.
139 H. Huang, Y. Li, Y. Tong, E.-P. Yao, M. W. Feil, A. F. Richter, M. Döblinger, A. L. Rogach, J. Feldmann and L. Polavarapu, *Angew. Chem., Int. Ed.*, 2019, **58**, 16558–16562.
140 Y. Hassan, O. J. Ashton, J. H. Park, G. Li, N. Sakai, B. Wenger, A.-A. Haghighirad, N. K. Noel, M. H. Song, B. R. Lee, R. H. Friend and H. J. Snaith, *J. Am. Chem. Soc.*, 2019, **141**, 1269–1279.
141 S. Wei, Y. Yang, X. Kang, L. Wang, L. Huang and D. Pan, *Inorg. Chem.*, 2017, **56**, 2596–2601.
142 D. Han, M. Imran, M. Zhang, S. Chang, X.-G. Wu, X. Zhang, J. Tang, M. Wang, S. Ali, X. Li, G. Yu, J. Han, L. Wang, B. Zou and H. Zhong, *ACS Nano*, 2018, **12**, 8808–8816.
143 Z. Zhenfu, J. Liang, W. Zhihai, C. Jiong, Z. Miaomiao and H. Yafei, *J. Mater. Sci.*, 2018, **53**, 15430–15441.
144 B. McKenna, A. Shivkumar, B. Charles and R. C. Evans, *Nanoscale*, 2020, **12**, 11694–11702.
145 N. K. Noel, S. N. Habisreutinger, B. Wenger, M. T. Klug, M. T. Hörantner, M. B. Johnston, R. J. Nicholas, D. T. Moore and H. J. Snaith, *Energy Environ. Sci.*, 2017, **10**, 145–152.
146 H. Cho, S.-H. Jeong, M.-H. Park, Y.-H. Kim, C. Wolf, C.-L. Lee, J. H. Heo, A. Sadhanala, N. Myoung, S. Yoo, S. H. Im, R. H. Friend and T.-W. Lee, *Science*, 2015, **350**, 1222–1225.
147 Y. Tong, E. Bladt, M. F. Aygüler, A. Manzi, K. Z. Milowska, V. A. Hintermayr, P. Docampo, S. Bals, A. S. Urban, L. Polavarapu and J. Feldmann, *Angew. Chem., Int. Ed.*, 2016, **55**, 13887–13892.
148 D. M. Jang, D. H. Kim, K. Park, J. Park, J. W. Lee and J. K. Song, *J. Mater. Chem. C*, 2016, **4**, 10625–10629.
149 X. Xu, H. He, Z. Fang, H. Lou, C. Lin, L. Chen and Z. Ye, *ACS Appl. Nano Mater.*, 2019, **2**, 6874–6879.
150 L. Rao, Y. Tang, C. Song, K. Xu, E. T. Vickers, S. Bonabi Naghadeh, X. Ding, Z. Li and J. Z. Zhang, *Chem. Mater.*, 2018, **31**, 365–375.
151 L. Rao, X. Ding, X. Du, G. Liang, Y. Tang, K. Tang and J. Z. Zhang, *Beilstein J. Nanotechnol.*, 2019, **10**, 666–676.
152 H. Huang, Q. Xue, B. Chen, Y. Xiong, J. Schneider, C. Zhi, H. Zhong and A. L. Rogach, *Angew. Chem., Int. Ed.*, 2017, **56**, 9571–9576.
153 V. A. Hintermayr, A. F. Richter, F. Ehrat, M. Döblinger, W. Vanderlinden, J. A. Sichert, Y. Tong, L. Polavarapu, J. Feldmann and A. S. Urban, *Adv. Mater.*, 2016, **28**, 9478–9485.
154 Y. Tong, B. J. Bohn, E. Bladt, K. Wang, P. Müller-Buschbaum, S. Bals, A. S. Urban, L. Polavarapu and J. Feldmann, *Angew. Chem., Int. Ed.*, 2017, **56**, 13887–13892.
155 C. Giansante, *J. Phys. Chem. C*, 2018, **122**, 18110–18116.
156 M. A. Boles, D. Ling, T. Hyeon and D. V. Talapin, *Nat. Mater.*, 2016, **15**, 141–153.
157 Q. Xie, D. Wu, X. Wang, Y. Li, F. Fang, Z. Wang, Y. Ma, M. Su, S. Peng, H. Liu, K. Wang and X. W. Sun, *J. Mater. Chem. C*, 2019, **7**, 11251–11257.
158 B. Luo, Y.-C. Pu, S. A. Lindley, Y. Yang, L. Lu, Y. Li, X. Li and J. Z. Zhang, *Angew. Chem., Int. Ed.*, 2016, **55**, 8864–8868.
159 C. Giansante, *Chem. – Eur. J.*, 2021, **27**, 14359–14369.
160 V. K. Ravi, P. K. Santra, N. Joshi, J. Chugh, S. K. Singh, H. Rensmo, P. Ghosh and A. Nag, *J. Phys. Chem. Lett.*, 2017, **8**, 4988–4994.
161 J. De Roo, M. Ibáñez, P. Geiregat, G. Nedelcu, W. Walravens, J. Maes, J. C. Martins, I. Van Driessche, M. V. Kovalenko and Z. Hens, *ACS Nano*, 2016, **10**, 2071–2081.
162 B. Fritzinger, I. Moreels, P. Lommens, R. Koole, Z. Hens and J. C. Martins, *J. Am. Chem. Soc.*, 2009, **131**, 3024–3032.
163 Y. Li, M. Cai, M. Shen, Y. Cai and R.-J. Xie, *J. Mater. Chem. C*, 2022, **10**, 8356–8363.
164 J. Pan, Y. Shang, J. Yin, M. De Bastiani, W. Peng, I. Dursun, L. Sinatra, A. M. El-Zohry, M. N. Hedhili, A.-H. Emwas, O. F. Mohammed, Z. Ning and O. M. Bakr, *J. Am. Chem. Soc.*, 2018, **140**, 562–565.
165 S. Kumar, J. Jagielski, T. Marcato, S. F. Solari and C.-J. Shih, *J. Phys. Chem. Lett.*, 2019, **10**, 7560–7567.
166 C.-H. Kuan and S.-H. Yang, *Adv. Mater.*, 2022, **3**, 7824.
167 T. Morris and T. Zubkov, *Colloids Surf., A*, 2014, **443**, 439–449.
168 F. Krieg, S. T. Ochsenbein, S. Yakunin, S. ten Brinck, P. Aellen, A. Süess, B. Clerc, D. Guggisberg, O. Nazarenko, Y. Shynkarenko, S. Kumar, C.-J. Shih, I. Infante and M. V. Kovalenko, *ACS Energy Lett.*, 2018, **3**, 641–646.
169 R. Grisorio, F. Fasulo, A. B. Muñoz-García, M. Pavone, D. Conelli, E. Fanizza, M. Striccoli, I. Allegretta, R. Terzano, N. Margiotta, P. Vivo and G. P. Suranna, *Nano Lett.*, 2022, **22**, 4437–4444.
170 C. Cueto, C. Donoghue, K. Bolduc and T. Emrick, *Chem. – Eur. J.*, 2022, **28**, e202200409.

171 Y. Luo, S. Zhou, Z. Dang and P. Gao, *J. Phys. Chem. C*, 2021, **125**, 27638–27646.
172 M. Imran, P. Ijaz, D. Baranov, L. Goldoni, U. Petralanda, Q. Akkerman, A. L. Abdelhady, M. Prato, P. Bianchini, I. Infante and L. Manna, *Nano Lett.*, 2018, **18**, 7822–7831.
173 A. Pan, B. He, X. Fan, Z. Liu, J. J. Urban, A. P. Alivisatos, L. He and Y. Liu, *ACS Nano*, 2016, **10**, 7943–7954.
174 S. Aharon, M. Wierzbowska and L. Etgar, *ACS Energy Lett.*, 2018, **3**, 1387–1393.
175 H. Huang, L. Polavarapu, J. A. Sichert, A. S. Susha, A. S. Urban and A. L. Rogach, *NPG Asia Mater.*, 2016, **8**, e328.
176 J. Huang, Y.-H. Wu, Z.-G. Zhu, W. Y. Shih and W.-H. Shih, *Chem. Phys. Lett.*, 2018, **702**, 21–25.
177 C. Otero-Martínez, D. García-Lojo, I. Pastoriza-Santos, J. Pérez-Juste and L. Polavarapu, *Angew. Chem., Int. Ed.*, 2021, **60**, 26677–26684.
178 A. Dutta, R. K. Behera, S. K. Dutta, S. das Adhikari and N. Pradhan, *J. Phys. Chem. Lett.*, 2018, **9**, 6599–6604.
179 T.-H. Le, S. Lee, H. Jo, G. Jeong, M. Chang and H. Yoon, *J. Phys. Chem. Lett.*, 2021, **12**, 5631–5638.
180 Y. Bekenstein, B. A. Koscher, S. W. Eaton, P. Yang and A. P. Alivisatos, *J. Am. Chem. Soc.*, 2015, **137**, 16008–16011.
181 Y. Dong, T. Qiao, D. Kim, D. Parobek, D. Rossi and D. H. Son, *Nano Lett.*, 2018, **18**, 3716–3722.
182 D. N. Dirin, L. Protesescu, D. Trummer, I. V. Kochetygov, S. Yakunin, F. Krumeich, N. P. Stadie and M. V. Kovalenko, *Nano Lett.*, 2016, **16**, 5866–5874.
183 S. Demchyshyn, J. M. Roemer, H. Groiß, H. Heilbrunner, C. Ulbricht, D. Apaydin, A. Böhm, U. Rütt, F. Bertram, G. Hesser, M. C. Scharber, N. S. Sariciftci, B. Nickel, S. Bauer, E. D. Głowacki and M. Kaltenbrunner, *Sci. Adv.*, 2017, **3**, e1700738.
184 S. Mollick, T. N. Mandal, A. Jana, S. Fajal, A. V. Desai and S. K. Ghosh, *ACS Appl. Nano Mater.*, 2019, **2**, 1333–1340.
185 C. Luo, C. Yan, W. Li, F. Chun, M. Xie, Z. Zhu, Y. Gao, B. Guo and W. Yang, *Adv. Funct. Mater.*, 2020, **30**, 2000026.
186 D. Parobek, B. J. Roman, Y. Dong, H. Jin, E. Lee, M. Sheldon and D. H. Son, *Nano Lett.*, 2016, **16**, 7376–7380.
187 S. L. Abiodun, P. J. Pellechia and A. B. Greytak, *J. Phys. Chem. C*, 2021, **125**, 3463–3471.
188 S. Sun, D. Yuan, Y. Xu, A. Wang and Z. Deng, *ACS Nano*, 2016, **10**, 3648–3657.
189 M. V. Kovalenko, L. Manna, A. Cabot, Z. Hens, D. V. Talapin, C. R. Kagan, V. I. Klimov, A. L. Rogach, P. Reiss, D. J. Milliron, P. Guyot-Sionnnest, G. Konstantatos, W. J. Parak, T. Hyeon, B. A. Korgel, C. B. Murray and W. Heiss, *ACS Nano*, 2015, **9**, 1012–1057.
190 S. Seth and A. Samanta, *Sci. Rep.*, 2016, **6**, 37693.
191 X. Zhang, X. Bai, H. Wu, X. Zhang, C. Sun, Y. Zhang, W. Zhang, W. Zheng, W. W. Yu and A. L. Rogach, *Angew. Chem., Int. Ed.*, 2018, **57**, 3337–3342.
192 T.-H. Le, S. Lee, E. Heo, U. Lee, H. Lee, H. Jo, K. S. Yang, M. Chang and H. Yoon, *Chem. Eng. J.*, 2021, **416**, 128045.
193 Y. Tong, M. Fu, E. Bladt, H. Huang, A. F. Richter, K. Wang, P. Müller-Buschbaum, S. Bals, P. Tamarat, B. Lounis, J. Feldmann and L. Polavarapu, *Angew. Chem., Int. Ed.*, 2018, **57**, 16094–16098.
194 H. Jiang, S. Cui, Y. Chen and H. Zhong, *Nano Sel.*, 2021, **2**, 2040–2060.
195 E. G. Ripka, C. R. Deschene, J. M. Franck, I.-T. Bae and M. M. Maye, *Langmuir*, 2018, **34**, 11139–11146.
196 Q. A. Akkerman, S. G. Motti, A. R. Srimath Kandada, E. Mosconi, V. D'Innocenzo, G. Bertoni, S. Marras, B. A. Kamino, L. Miranda, F. De Angelis, A. Petrozza, M. Prato and L. Manna, *J. Am. Chem. Soc.*, 2016, **138**, 1010–1016.
197 M. Hao, Y. Bai, S. Zeiske, L. Ren, J. Liu, Y. Yuan, N. Zarrabi, N. Cheng, M. Ghasemi, P. Chen, M. Lyu, D. He, J.-H. Yun, Y. Du, Y. Wang, S. Ding, A. Armin, P. Meredith, G. Liu, H.-M. Cheng and L. Wang, *Nat. Energy*, 2020, **5**, 79–88.
198 F. Li, S. Zhou, J. Yuan, C. Qin, Y. Yang, J. Shi, X. Ling, Y. Li and W. Ma, *ACS Energy Lett.*, 2019, **4**, 2571–2578.
199 J. Yuan, X. Ling, D. Yang, F. Li, S. Zhou, J. Shi, Y. Qian, J. Hu, Y. Sun, Y. Yang, X. Gao, S. Duhm, Q. Zhang and W. Ma, *Joule*, 2018, **2**, 2450–2463.
200 J. Xue, J.-W. Lee, Z. Dai, R. Wang, S. Nuryyeva, M. E. Liao, S.-Y. Chang, L. Meng, D. Meng, P. Sun, O. Lin, M. S. Goorsky and Y. Yang, *Joule*, 2018, **2**, 1866–1878.
201 R. Soltani, B. M. D. Puscher, A. A. Katbab, I. Levchuk, N. Kazerouni, N. Gasparini, N. Camaioni, A. Osvet, M. Batentschuk, R. H. Fink, D. M. Guldi and T. Ameri, *Phys. Chem. Chem. Phys.*, 2018, **20**, 23674–23683.
202 L. Zhang, T. Hu, J. Li, L. Zhang, H. Li, Z. Lu and G. Wang, *Front. Mater.*, 2020, **6**, 330.
203 K. Ji, J. Yuan, F. Li, Y. Shi, X. Ling, X. Zhang, Y. Zhang, H. Lu, J. Yuan and W. Ma, *J. Mater. Chem. A*, 2020, **8**, 8104–8112.
204 Y. Wang, J. Yuan, X. Zhang, X. Ling, B. W. Larson, Q. Zhao, Y. Yang, Y. Shi, J. M. Luther and W. Ma, *Adv. Mater.*, 2020, **32**, e2000449.
205 D. Jia, J. Chen, M. Yu, J. Liu, E. M. J. Johansson, A. Hagfeldt and X. Zhang, *Small*, 2020, **16**, e2001772.
206 X. Zhang, Y. Qian, X. Ling, Y. Wang, Y. Zhang, J. Shi, Y. Shi, J. Yuan and W. Ma, *ACS Appl. Mater. Interfaces*, 2020, **12**, 27307–27315.
207 S. B. Shivarudraiah, M. Ng, C.-H. A. Li and J. E. Halpert, *ACS Appl. Energy Mater.*, 2020, **3**, 5620–5627.
208 S. Lim, G. Lee, S. Han, J. Kim, S. Yun, J. Lim, Y.-J. Pu, M. J. Ko, T. Park, J. Choi and Y. Kim, *ACS Energy Lett.*, 2021, 2229–2237.
209 L. Hu, Q. Zhao, S. Huang, J. Zheng, X. Guan, R. Patterson, J. Kim, L. Shi, C.-H. Lin, Q. Lei, D. Chu, W. Tao, S. Cheong, R. D. Tilley, A. W. Y. Ho-Baillie, J. M. Luther, J. Yuan and T. Wu, *Nat. Commun.*, 2021, **12**, 466.
210 J. Yuan, X. Zhang, J. Sun, R. Patterson, H. Yao, D. Xue, Y. Wang, K. Ji, L. Hu, S. Huang, D. Chu, T. Wu, J. Hou and J. Yuan, *Adv. Funct. Mater.*, 2021, **31**, 2101272.

211 X. Zhang, H. Huang, X. Ling, J. Sun, X. Jiang, Y. Wang, D. Xue, L. Huang, L. Chi, J. Yuan and W. Ma, *Adv. Mater.*, 2022, **34**, e2105977.
212 A. Rubino, L. Caliò, M. E. Calvo and H. Míguez, *Sol. RRL*, 2021, **5**, 2100204.
213 J. Yuan, C. Bi, J. Xi, R. Guo and J. Tian, *J. Phys. Chem. Lett.*, 2021, **12**, 1018–1024.
214 R. Han, Q. Zhao, J. Su, X. Zhou, X. Ye, X. Liang, J. Li, H. Cai, J. Ni and J. Zhang, *J. Phys. Chem. C*, 2021, **125**, 8469–8478.
215 Y. Liu, Q. Li, W. Zhang, Z. Yang, S. Zhao and W. Chen, *ACS Appl. Energy Mater.*, 2021, **4**, 6688–6696.
216 D. Jia, J. Chen, X. Mei, W. Fan, S. Luo, M. Yu, J. Liu and X. Zhang, *Energy Environ. Sci.*, 2021, **14**, 4599–4609.
217 D. Ghosh, Md. Y. Ali, A. Ghosh, A. Mandal and S. Bhattacharyya, *J. Phys. Chem. C*, 2021, **125**, 5485–5493.
218 S. Mahato, A. Ghorai, A. Mondal, S. K. Srivastava, M. Modak, S. Das and S. K. Ray, *ACS Appl. Mater. Interfaces*, 2022, **14**, 9711–9723.
219 J. Kim, S. Han, G. Lee, J. Choi, M. Jae Ko and Y. Kim, *Chem. Eng. J.*, 2022, **448**, 137672.
220 Y. Xu, H. Li, S. Ramakrishnan, D. Song, Y. Zhang, M. Cotlet and Q. Yu, *ACS Appl. Energy Mater.*, 2022, **5**, 9858–9869.
221 C. Zhao, X. Zhang, H. Huang and J. Yuan, *J. Chem. Phys.*, 2022, **157**, 031101.
222 W. Wei, W. Chen, X. Zhao, Z. Yang and Y. Liu, *J. Alloys Compd.*, 2022, **891**, 161985.
223 G. Almeida, I. Infante and L. Manna, *Science*, 2019, **364**, 833–834.
224 Z. Ni, C. Bao, Y. Liu, Q. Jiang, W.-Q. Wu, S. Chen, X. Dai, B. Chen, B. Hartweg, Z. Yu, Z. Holman and J. Huang, *Science*, 2020, **367**, 1352–1358.
225 L. Hu, Q. Li, Y. Yao, Q. Zeng, Z. Zhou, C. Cazorla, T. Wan, X. Guan, J.-K. Huang, C.-H. Lin, M. Li, S. Cheong, R. D. Tilley, D. Chu, J. Yuan, S. Huang, T. Wu and F. Liu, *ACS Mater. Lett.*, 2022, **4**, 120–127.
226 A. Hazarika, Q. Zhao, E. A. Gaulding, J. A. Christians, B. Dou, A. R. Marshall, T. Moot, J. J. Berry, J. C. Johnson and J. M. Luther, *ACS Nano*, 2018, **12**, 10327–10337.
227 Q. Zhao, A. Hazarika, X. Chen, S. P. Harvey, B. W. Larson, G. R. Teeter, J. Liu, T. Song, C. Xiao, L. Shaw, M. Zhang, G. Li, M. C. Beard and J. M. Luther, *Nat. Commun.*, 2019, **10**, 2842.
228 S. Han, J. Kim, D. E. Kim, M. J. Ko, J. Choi, S.-W. Baek and Y. Kim, *J. Mater. Chem. A*, 2022, **10**, 8966–8974.
229 L. M. Wheeler, E. M. Sanehira, A. R. Marshall, P. Schulz, M. Suri, N. C. Anderson, J. A. Christians, D. Nordlund, D. Sokaras, T. Kroll, S. P. Harvey, J. J. Berry, L. Y. Lin and J. M. Luther, *J. Am. Chem. Soc.*, 2018, **140**, 10504–10513.
230 C. Liu, Q. Zeng, H. Wei, Y. Yu, Y. Zhao, T. Feng and B. Yang, *Small Methods*, 2020, **4**, 2000419.
231 C. Liu, Q. Zeng, Y. Zhao, Y. Yu, M. Yang, H. Gao, H. Wei and B. Yang, *Sol. RRL*, 2020, **4**, 2000102.
232 J. Khan, X. Zhang, J. Yuan, Y. Wang, G. Shi, R. Patterson, J. Shi, X. Ling, L. Hu, T. Wu, S. Dai and W. Ma, *ACS Energy Lett.*, 2020, **5**, 3322–3329.
233 M. V. Kovalenko, L. Protesescu and M. I. Bodnarchuk, *Science*, 2017, **358**, 745–750.
234 S. Jiang, Y. Song, H. Kang, B. Li, K. Yang, G. Xing, Y. Yu, S. Li, P. Zhao and T. Zhang, *ACS Appl. Mater. Interfaces*, 2022, **14**, 3385–3394.
235 X. Wang, W. Li, X. Zhao, J. Fu, G. Zhang, W. Ma, W.-H. Zhang and H. W. Choi, *Appl. Phys. Lett.*, 2022, **120**, 011903.
236 Q. Liao, Q. Meng, L. Jing, J. Pang, Q. Pang and J. Z. Zhang, *J. Phys. Chem. C*, 2021, **125**, 18372–18379.
237 D. Li, Y. Liu, S. Shi, Y. Li, C. Geng and S. Xu, *J. Mater. Chem. C*, 2021, **9**, 2873–2881.
238 K. Chen, W. Jin, Y. Zhang, T. Yang, P. Reiss, Q. Zhong, U. Bach, Q. Li, Y. Wang, H. Zhang, Q. Bao and Y. Liu, *J. Am. Chem. Soc.*, 2020, **142**, 3775–3783.
239 F. C. Marques and J. J. Jasieniak, *Appl. Surf. Sci.*, 2017, **422**, 504–508.
240 X. Liu, H. Zhao, L. Wei, X. Ren, X. Zhang, F. Li, P. Zeng and M. Liu, *Nanophotonics*, 2021, **10**, 1967–1975.
241 Q. Jiang, X. Zhang and J. You, *Small*, 2018, e1801154.
242 S. Lim, J. Kim, J. Y. Park, J. Min, S. Yun, T. Park, Y. Kim and J. Choi, *ACS Appl. Mater. Interfaces*, 2021, **13**, 6119–6129.
243 G. H. Ahmed, J. K. El-Demellawi, J. Yin, J. Pan, D. B. Velusamy, M. N. Hedhili, E. Alarousu, O. M. Bakr, H. N. Alshareef and O. F. Mohammed, *ACS Energy Lett.*, 2018, **3**, 2301–2307.
244 H. Li, Y. Qian, X. Xing, J. Zhu, X. Huang, Q. Jing, W. Zhang, C. Zhang and Z. Lu, *J. Phys. Chem. C*, 2018, **122**, 12994–13000.
245 S. Geng, Y. Wen, B. Zhou, Z. Wang, Z. Wang, P. Wang, Y. Jing, K. Cao, K. Wang and R. Chen, *ACS Appl. Electron. Mater.*, 2021, **3**, 2362–2371.
246 J. Chen, D. Jia, E. M. J. Johansson, A. Hagfeldt and X. Zhang, *Energy Environ. Sci.*, 2020, **14**, 224–261.
247 X. Ling, S. Zhou, J. Yuan, J. Shi, Y. Qian, B. W. Larson, Q. Zhao, C. Qin, F. Li, G. Shi, C. Stewart, J. Hu, X. Zhang, J. M. Luther, S. Duhm and W. Ma, *Adv. Energy Mater.*, 2019, 1900721.
248 J. Kim, S. Cho, F. Dinic, J. Choi, C. Choi, S. M. Jeong, J.-S. Lee, O. Voznyy, M. J. Ko and Y. Kim, *Nano Energy*, 2020, **75**, 104985.
249 Z.-L. Tseng, L.-C. Chen, L.-W. Chao, M.-J. Tsai, D. Luo, N. R. Al Amin, S.-W. Liu and K.-T. Wong, *Adv. Mater.*, 2022, **34**, e2109785.
250 E. T. Vickers, T. A. Graham, A. H. Chowdhury, B. Bahrami, B. W. Dreskin, S. Lindley, S. B. Naghadeh, Q. Qiao and J. Z. Zhang, *ACS Energy Lett.*, 2018, **3**, 2931–2939.
251 X. Ling, J. Yuan, X. Zhang, Y. Qian, S. M. Zakeeruddin, B. W. Larson, Q. Zhao, J. Shi, J. Yang, K. Ji, Y. Zhang, Y. Wang, C. Zhang, S. Duhm, J. M. Luther, M. Grätzel and W. Ma, *Adv. Mater.*, 2020, **32**, e2001906.
252 R. X. Yang and L. Z. Tan, *J. Chem. Phys.*, 2020, **152**, 034702.

253 S. Christodoulou, F. Di Stasio, S. Pradhan, A. Stavrinadis and G. Konstantatos, *J. Phys. Chem. C*, 2018, **122**, 7621–7626.
254 M. Suri, A. Hazarika, B. W. Larson, Q. Zhao, M. Vallés-Pelarda, T. D. Siegler, M. K. Abney, A. J. Ferguson, B. A. Korgel and J. M. Luther, *ACS Energy Lett.*, 2019, **4**, 1954–1960.
255 B. M. Wieliczka, J. A. Márquez, A. M. Bothwell, Q. Zhao, T. Moot, K. T. VanSant, A. J. Ferguson, T. Unold, D. Kuciauskas and J. M. Luther, *ACS Nano*, 2021, **15**, 19334–19344.
256 S. Kim, K.-D. Park and H. Lee, *Energies*, 2021, **14**, 275.
257 S. Cho, J. Kim, S. M. Jeong, M. J. Ko, J.-S. Lee and Y. Kim, *Chem. Mater.*, 2020, **32**, 8808–8818.
258 D. P. McMeekin, G. Sadoughi, W. Rehman, G. E. Eperon, M. Saliba, M. T. Hörantner, A. Haghighirad, N. Sakai, L. Korte, B. Rech, M. B. Johnston, L. M. Herz and H. J. Snaith, *Science*, 2016, **351**, 151–155.
259 R. J. Sutton, M. R. Filip, A. A. Haghighirad, N. Sakai, B. Wenger, F. Giustino and H. J. Snaith, *ACS Energy Lett.*, 2018, **3**, 1787–1794.
260 S. Tan, J. Shi, B. Yu, W. Zhao, Y. Li, Y. Li, H. Wu, Y. Luo, D. Li and Q. Meng, *Adv. Funct. Mater.*, 2021, **31**, 2010813.
261 Y. Wang, M. I. Dar, L. K. Ono, T. Zhang, M. Kan, Y. Li, L. Zhang, X. Wang, Y. Yang, X. Gao, Y. Qi, M. Grätzel and Y. Zhao, *Science*, 2019, **365**, 591–595.
262 J. H. Heo, F. Zhang, C. Xiao, S. J. Heo, J. K. Park, J. J. Berry, K. Zhu and S. H. Im, *Joule*, 2021, **5**, 481–494.
263 Y. Zhao, K. Zhao, L. Wan, Y. Tan and Z.-S. Wang, *ACS Appl. Mater. Interfaces*, 2022, **14**, 6906–6915.
264 S. Xiang, Z. Fu, W. Li, Y. Wei, J. Liu, H. Liu, L. Zhu, R. Zhang and H. Chen, *ACS Energy Lett.*, 2018, **3**, 1824–1831.
265 W. Ahmad, J. Khan, G. Niu and J. Tang, *Sol. RRL*, 2017, **1**, 1700048.
266 A. Dutta, S. K. Dutta, S. Das Adhikari and N. Pradhan, *Angew. Chem., Int. Ed.*, 2018, **57**, 9083–9087.
267 M. Kim, D. Cortecchia, T. Borzda, W. Mróz, L. Leoncino, D. Dellasega, S.-H. Lee and A. Petrozza, *Chem. Mater.*, 2021, **33**, 547–553.
268 Q. Wang, X. Zheng, Y. Deng, J. Zhao, Z. Chen and J. Huang, *Joule*, 2017, **1**, 371–382.
269 B. Wang, N. Novendra and A. Navrotsky, *J. Am. Chem. Soc.*, 2019, **141**, 14501–14504.
270 C. Xiao, Q. Zhao, C.-S. Jiang, Y. Sun, M. M. Al-Jassim, S. U. Nanayakkara and J. M. Luther, *Nano Energy*, 2020, **78**, 105319.
271 M. Stolterfoht, P. Caprioglio, C. M. Wolff, J. A. Márquez, J. Nordmann, S. Zhang, D. Rothhardt, U. Hörmann, Y. Amir, A. Redinger, L. Kegelmann, F. Zu, S. Albrecht, N. Koch, T. Kirchartz, M. Saliba, T. Unold and D. Neher, *Energy Environ. Sci.*, 2019, **12**, 2778–2788.
272 M. M. Tavakoli, M. Nasilowski, J. Zhao, M. G. Bawendi and J. Kong, *Small Methods*, 2019, **3**, 1900449.
273 S. Mahato, J. Puigdollers, C. Voz, M. Mukhopadhyay, M. Mukherjee and S. Hazra, *Appl. Surf. Sci.*, 2020, **499**, 143967.
274 Y. Bai, M. Hao, S. Ding, P. Chen and L. Wang, *Adv. Mater.*, 2022, **34**, e2105958.
275 A. R. Kirmani, M. Woodhouse and J. M. Luther, *ACS Energy Lett.*, 2022, **7**, 1255–1259.
276 F. Yan and H. V. Demir, *Opt. Mater. Express*, 2022, **12**, 256.
277 Y. Miao, X. Liu, Y. Chen, T. Zhang, T. Wang and Y. Zhao, *Adv. Mater.*, 2021, **33**, e2105699.
278 C.-G. Lu, X.-F. Hu, S.-H. Xu, H.-G. Liu, J.-K. Xu, Y.-P. Cui and C.-L. Wang, *RSC Adv.*, 2020, **10**, 25480–25486.
279 M. Michalska, M. A. Surmiak, F. Maasoumi, D. C. Senevirathna, P. Chantler, H. Li, B. Li, T. Zhang, X. Lin, H. Deng, N. Chandrasekaran, T. A. N. Peiris, K. J. Rietwyk, A. S. R. Chesman, T. Alan, D. Vak, U. Bach and J. J. Jasieniak, *Sol. RRL*, 2021, 2100342.
280 L. Xie, P. Vashishtha, T. M. Koh, P. C. Harikesh, N. F. Jamaludin, A. Bruno, T. J. N. Hooper, J. Li, Y. F. Ng, S. G. Mhaisalkar and N. Mathews, *Adv. Mater.*, 2020, **32**, e2003296.
281 S. Akin, Y. Altintas, E. Mutlugun and S. Sonmezoglu, *Nano Energy*, 2019, **60**, 557–566.
282 W. Yang, R. Su, D. Luo, Q. Hu, F. Zhang, Z. Xu, Z. Wang, J. Tang, Z. Lv, X. Yang, Y. Tu, W. Zhang, H. Zhong, Q. Gong, T. P. Russell and R. Zhu, *Nano Energy*, 2020, **67**, 104189.
283 X. Zheng, J. Troughton, N. Gasparini, Y. Lin, M. Wei, Y. Hou, J. Liu, K. Song, Z. Chen, C. Yang, B. Turedi, A. Y. Alsalloum, J. Pan, J. Chen, A. A. Zhumekenov, T. D. Anthopoulos, Y. Han, D. Baran, O. F. Mohammed, E. H. Sargent and O. M. Bakr, *Joule*, 2019, **3**, 1963–1976.
284 M. Hermenau, S. Scholz, K. Leo and M. Riede, *Sol. Energy Mater. Sol. Cells*, 2011, **95**, 1278–1283.
285 M. V. Khenkin, E. A. Katz, A. Abate, G. Bardizza, J. J. Berry, C. Brabec, F. Brunetti, V. Bulović, Q. Burlingame, A. Di Carlo, R. Cheacharoen, Y.-B. Cheng, A. Colsmann, S. Cros, K. Domanski, M. Dusza, C. J. Fell, S. R. Forrest, Y. Galagan, D. Di Girolamo and M. Lira-Cantu, *Nat. Energy*, 2020, **5**, 35–49.
286 L. Scalon, R. Szostak, F. L. Araújo, K. F. Adriani, J. F. R. V. Silveira, W. X. C. Oliveira, J. L. F. Da Silva, C. C. Oliveira and A. F. Nogueira, *JACS Au*, 2022, **2**, 1306–1312.
287 X. Luo, Z. Shen, Y. Shen, Z. Su, X. Gao, Y. Wang, Q. Han and L. Han, *Adv. Mater.*, 2022, **34**, e2202100.
288 T. Zhang, B. Zhao, Z. Li, S. Liu, C. Liu, X. Li, H. Liu, Y. Chen, Z. Liu and X. Li, *J. Mater. Chem. C*, 2022, **10**, 1357–1364.
289 S. Aina, B. Villacampa and M. Bernechea, *Adv. Mater.*, 2021, **2**, 4140–4151.
290 Y. Wang, S. R. Kavanagh, I. Burgués-Ceballos, A. Walsh, D. O. Scanlon and G. Konstantatos, *Nat. Photonics*, 2022, **16**, 235–241.